



HAL
open science

Seeking for non-Fourier heat transfer with thermorefectance

Ahmad Zenji

► **To cite this version:**

Ahmad Zenji. Seeking for non-Fourier heat transfer with thermorefectance. Physics [physics]. Université de Bordeaux, 2022. English. NNT : 2022BORD0370 . tel-03986276

HAL Id: tel-03986276

<https://theses.hal.science/tel-03986276>

Submitted on 13 Feb 2023

HAL is a multi-disciplinary open access archive for the deposit and dissemination of scientific research documents, whether they are published or not. The documents may come from teaching and research institutions in France or abroad, or from public or private research centers.

L'archive ouverte pluridisciplinaire **HAL**, est destinée au dépôt et à la diffusion de documents scientifiques de niveau recherche, publiés ou non, émanant des établissements d'enseignement et de recherche français ou étrangers, des laboratoires publics ou privés.

THÈSE PRÉSENTÉE
POUR OBTENIR LE GRADE DE

**DOCTEUR DE
L'UNIVERSITÉ DE BORDEAUX**

ÉCOLE DOCTORALE DES SCIENCES PHYSIQUE ET DE L'INGÉNIEUR

SPÉCIALITÉ : Laser, Matière et Nanosciences

Ahmad ZENJI

**SEEKING FOR NON-FOURIER HEAT TRANSFER WITH
THERMOREFLECTANCE**

Sous la direction de : Pr. Stefan DILHAIRE
(co-directeur : Pr. Stéphane GRAUBY, co-encadrant : Dr. Jean-Michel RAMPNOUX)

Soutenue le 9 décembre 2022

Membres du jury :

M. VALLEE Fabrice, Directeur de recherche, Université de Lyon (Villeurbanne)
M. BOURGEOIS Olivier, Directeur de recherche, Université de Grenoble Alpes (Grenoble)
M. DILHAIRE Stefan, Professeur, Université de Bordeaux (Talence),
M. GRAUBY Stéphane, Professeur, Université de Bordeaux (Talence),
M. DEGERT Jérôme, Professeur, Université de Bordeaux (Talence)
M. PERNOT Gilles, Maître de conférences, Université de Lorraine (Nancy)
Mme ABAD Begoña, Docteure, Université de Basel (Basel, SUISSE)
Mme FLEURANCE Nolwenn, Ingénieure de recherche, LNE (Paris)
M. RAMPNOUX Jean-Michel, Maître de conférences, Université de Bordeaux (Talence)

Rapporteur
Rapporteur
Directeur de thèse
Co-Directeur
Président
Examinateur
Examinatrice
Invitée
Invité

Titre : A la recherche d'un transfert de chaleur non-Fourier avec la thermoréfectance

Résumé :

La conduction thermique régie par les phonons dans les matériaux est généralement décrite par le modèle de diffusion de Fourier. Par contre, un nouveau comportement thermique observé dans les alliages, appelé régime superdiffusif basé sur la dynamique de Lévy, peut être observé à des échelles spatiales et temporelles spécifiques. Il s'agit d'un régime intermédiaire entre les régimes balistique et diffusif. Plusieurs méthodes thermiques théoriques et expérimentales ont été proposées pour modéliser la superdiffusivité. Pourtant, de nombreuses caractéristiques prédites par celles-ci n'ont pas été observées expérimentalement. Cela représente toujours un défi dans le transport thermique pour de nombreuses applications à l'échelle nanométrique. Dans ce contexte, nous avons développé un capteur thermique spectral à large bande, qui combine des mesures de thermoréfectance dans les domaines temporel et fréquentiel (TDTR et FDTR), en but d'étudier ce régime non-Fourier dans certains semi-conducteurs.

Premièrement, la bande passante thermique de la technique TDTR est limitée par le transport thermique dans le transducteur, déposé au-dessus du matériau d'intérêt. Ainsi, nous avons étudié la transparence thermique de plusieurs films métalliques pour optimiser la nature et l'épaisseur du transducteur. Dans la deuxième partie, nous avons développé un capteur à large bande basé sur la combinaison FDTR/TDTR qui permet de mesurer à notre connaissance la plus large réponse thermique des matériaux sur 8 décades, de 10 kHz jusqu'à 1 THz. Par conséquent, cela permet également d'atteindre une résolution temporelle ultime de la réponse thermique transitoire. Nous avons ensuite effectué à travers le capteur des mesures et identifié des propriétés thermiques dans une gamme de valeurs de conductivité thermique de films minces allant de 10^{-1} à 10^2 W/m/K. Dans la troisième partie, la mesure analysée avec un modèle basé sur la dynamique de Lévy a permis de mettre en évidence la présence de transport thermique non diffusif dans les alliages InGaAs. Ensuite, nous avons étudié la réponse thermique du matériau modèle GeMn incorporant des nano-inclusions, qui devrait présenter un comportement quasi-balistique. Enfin, nous avons développé une technique d'imagerie TDTR ultrarapide afin d'étudier le transport thermique dans le plan. Ce qui rend notre banc de mesure capable de réaliser une étude thermique dans le plan et hors du plan.

Mots clés :

Echantillonnage optique asynchrone/hétérodyne, TDTR, FDTR, Thermoréfectance, Transport thermique à l'échelle nanométrique, Pompe-sonde femtoseconde, Phonons, Dynamique de Lévy, Semi-conducteurs, Transport balistique-diffusif, Films métalliques, Imagerie thermique

Title : Seeking for non-Fourier heat transfer with thermoreflectance

Abstract :

Phonons heat conduction in materials is usually described by the well-known Fourier diffusion model. However, a new thermal behavior in alloys, called superdiffusive regime based on the Lévy dynamics, can be observed at specific space and time scales. It is an intermediate regime between the ballistic and diffusive regimes. Several theoretical and experimental thermal methods were proposed to model the superdiffusivity. Yet, many predicted characteristic features have not been observed experimentally. It still represents a longstanding challenge in thermal transport for numerous nanoscale applications. In this context, we have developed a broadband spectral thermal sensor, which combines Time- and Frequency-domain thermoreflectance (TDTR and FDTR) measurements, seeking for this non-Fourier regime in certain semi-conductors.

First, the ultimate thermal bandwidth of the TDTR technique is limited by the thermal transport in the transducer deposited above the material of interest. Thus, we have studied the thermal transparency of several metal films to optimize the nature and thickness of the transducer. In the second part, we have developed a broadband sensor based on the combination of FDTR/TDTR that allows to measure to our knowledge the widest thermal response of materials over 8 decades, from 10 kHz up to 1 THz. Hence, it also makes possible to achieve the ultimate temporal resolution of the transient thermal response. We then performed the sensor measurements and identified the thermal properties in a range of thermal conductivity values of thin films ranging from 10^{-1} to 10^2 W/m/K. In the third part, the sensor measurement, analyzed with a model based on Lévy dynamics, highlighted the presence of non-diffusive thermal transport in InGaAs alloys. Then, we investigated the thermal response of model material GeMn incorporating nano-inclusions, which are expected to exhibit a quasi-ballistic behavior. Finally, we developed an ultrafast TDTR imaging technique in order to study the in-plane thermal propagation. This makes our bench capable of complete in and out of plane studies.

Keywords :

Asynchronous/Heterodyne optical sampling, TDTR, FDTR, Thermoreflectance, Heat transport at nanoscale, Femtosecond pump-probe, Phonons, Lévy dynamics, Semi-conductors, Ballistic-diffusive transport, Metallic films, Heat imaging

Unité de recherche

Université de Bordeaux, CNRS, LOMA, UMR 5798, F-33400 Talence, France

Acknowledgement

I warmly thank Mr. Fabrice Vallée and Mr. Olivier Bourgeois for having agreed to be the scientific reviewers of this work and for having evaluated it. I also thank Mr. Jérôme Degert, Mr. Gilles Pernot, Mrs. Begoña Abad and Mrs. Nolwenn Fleurance for their participation in the thesis defense jury.

I would like to thank my thesis supervisors, Pr. Stefan Dilhaire and Pr. Stéphane Grauby, for giving me the opportunity to complete this thesis within their team, and for guiding and advising me throughout these years until to final rendering.

I would like to thank Jean-Michel Rampnoux, who also guided me, advised me and above all helped me during these three years of work.

My charming colleagues, doctoral and post-doctoral students of the team, without whom the atmosphere and the good mood would not be there. To them, and to the whole team, I owe a huge thank you.

Thank you to all the technical and administrative staff of the laboratory, for their respective help and advice as well as for all the good times spent during the laboratory events.

Thank you to all my friends in Bordeaux, Arthur, Tarek, Ahmad, Amani, Sara and Hala, who were there during my ups and downs, who supported me on a daily basis, and who above all transformed the moments spent in their company into a string of unforgettable memories.

Thank you to my friends from university, Sahar, Ahmad, Moustapha, Bilal and many others. We came to France together seeking education, and we all embarked on research. And here we are, after several years, doctors and future doctors. This experience with you is dear to me and has certainly changed our lives. This experience, I will keep it engraved in my heart, hoping for many more to come.

These three years of work and effort, I dedicate them to my family.

To my parents, Khalil and Rajaa, whose presence and encouragement were for me the founding pillars of what I am and what I do. Thank you for your unconditional love and support. Thank you for your sacrifices throughout my life that helped me be the person I am today. It is to you that I give my deepest thanks and to whom I will always be grateful for the love, effort and hope you offered me.

To my brothers, Ali and Hassan. Thank you, simply for your company and support during every moment of my life. You are the ones who encouraged me to go out into the world, who supported my biggest decisions, and were always there for me, there to make me smile and see me grow. With that, you never stopped proving me the meaning of brotherhood and the love we have for one another.

To my biggest supporter, Nour. Thank you for your daily support and encouragement. Thank you for just being you, an adventure enthusiast who constantly pushes us both to explore more and evolve, in order to grow personally and professionally. I enjoyed and still enjoy every moment we spend together, creating memories I will cherish for life!

To France, which opened its doors for me to pursue my graduate studies.

And to Lebanon, the wonderful country I come from.

Finally, although I am leaving for new adventures elsewhere, these three years spent in the team at LOMA will always be scripted in my mind and heart. It was a team full of spirit, love and joy, just like a family, and we were truly one. A family to whom I will not say farewell, but I will say au revoir...

Table of content

Acknowledgement	7
Table of content	9
List of abbreviations	13
Introduction	17
Chapter 1 : Heat transport in nanomaterials: Measurements and identifications of thermal properties	23
1.1 Introduction	23
1.2 Measurements and processing tools for thermal property identification in solids	24
1.2.1 Contact methods.....	25
1.2.2 Non-contact methods	28
1.3 Thermoreflectance: Time-Domain vs Frequency-Domain.....	34
1.3.1 Time-Domain Thermoreflectance (TDTR): synchronous optical sampling vs asynchronous optical sampling	34
1.3.2 Frequency-Domain Thermoreflectance (FDTR)	40
1.4 Modeling thermal transport in thermoreflectance experiments	42
1.4.1 Dynamics of electrons and phonons: Two-Temperature Model (2TM)	43
1.4.2 Fourier heat transport: One-Temperature Model (1TM)	45
1.5 Solving 1TM by quadrupole method.....	46
1.5.1 Thermal quadrupole formalism	47
1.5.2 Particular cases and conditions.....	49
1.5.3 Expression of the surface temperature	52
1.6 Inverse method for thermal parameters identifications	53
1.6.1 Direct Problem / Inverse Problem	53
1.6.2 Mathematical description of the inverse method	55
1.6.3 Experimental examples of SiO ₂ and Ge thermal identification	56
1.6.4 Uncertainty sources	59
1.7 Conclusion.....	59
Chapter 2 : Ultimate thermal resolution in TDTR: Influence of the transducer	63
2.1 Introduction	63
2.2 Ultra-fast transient thermal effects in the transducer	64

2.3	Thermal transport modeling of metal transducer: Solving non-linear 2TM by Finite element method.....	65
2.3.1	Transducer upon a layer of interest.....	65
2.3.2	Laser excitation	68
2.4	Thermal investigation of aluminum and gold transducers	68
2.4.1	Electron and phonon dynamics through the films.....	69
2.4.2	Phononic dynamics at the film–substrate interface	72
2.4.3	Spectral response study	74
2.5	Experimental validation of the modeling.....	76
2.5.1	Asynchronous TDTR setup	76
2.5.2	Spectrum of Au transducer film	78
2.6	Thermal behavior of other metal films	79
2.7	Conclusion.....	81
Chapter 3 : Ultra-broadband spectroscopy of heat transport.....		85
3.1	Introduction	85
3.2	Scenario of thermal parameter identification in frequency domain.....	86
3.3	Direct problem and sensitivity study of 1TM.....	88
3.3.1	Case study: transducer on substrate to evaluate the range of measurement	89
3.3.2	Modeling over 3 decades of thermal conductivities	90
3.3.3	Influence of transducer thickness on the sensitivity of thermal properties.....	93
3.3.4	Asymptotic behavior	94
3.3.5	Additional thermal parameters sensitivity	99
3.4	Ultra-broadband spectral thermal sensor from 10 kHz to 1 THz.....	102
3.4.1	Spectroscopic measurements via combined time- and frequency-domain thermorefectance.	102
3.4.2	Over 3 decades thermal conductivity identification.....	106
3.4.3	Conclusion.....	111
3.5	Uncertainty analysis.....	112
3.5.1	Experimental noise	112
3.5.2	Fixed parameters	115
3.5.3	Correlated parameters.....	117
3.6	Conclusion.....	118
Chapter 4 : Spectroscopy of superdiffusive phonons in non-Fourier materials.....		123
4.1	Introduction	123

4.2	Superdiffusion heat conduction and Lévy processes.....	124
4.2.1	Bird's eye view of non-Fourier transport.....	124
4.2.2	Thermal transport regimes in alloys	126
4.2.3	Origin of the superdiffusive Lévy regime	131
4.3	Modeling the truncated Lévy distribution	134
4.3.1	Implementation of the superdiffusion model	134
4.3.2	Comparative study with the response of diffusive 1TM.....	136
4.4	Experimental study and analysis out of plane diffusion	138
4.4.1	InGaAs	138
4.4.2	GeMn.....	141
4.4.3	Conclusion.....	150
4.5	Heat transfer dynamics imaging for in-plane diffusion analysis.....	150
4.5.1	TDTR scanning system.....	151
4.5.2	Measurement and acquisition process.....	153
4.6	In-plane thermal properties identification	154
4.6.1	Parabolic method	154
4.6.2	Hotspot imaging in homogenous gold film	156
4.7	Conclusion and perspective	161
	Conclusion	165
	List of achievements	169
	References.....	171

List of abbreviations

1TM	One-Temperature Model
2TM	Two-Temperature Model
AC	Alternating Current
AFM	Atomic Force Microscopy
SThM	Scanning Thermal Microscopy
ANR	Agence Nationale de la Recherche
P-SThM	Scanning Thermal Microscopy in Passive mode
A-SThM	Scanning Thermal Microscopy in active mode
CCD	Charge Coupled Device
CW	Continuous Wave
FDTR	Frequency-Domain Thermoreflectance
TDTR	Time-Domain Thermoreflectance
FEM	Finite Element Method
TEM	Transmission Electron Microscopy
MBE	Molecular Beam Epitaxy
LEMTA	Laboratoire Énergies & Mécanique Théorique et Appliquée
LOMA	Laboratoire Ondes et Matière d'Aquitaine
Néel	Research laboratory in condensed matter physics
SPiDER-man	ANR project called Spectral Superdiffusive Phonon Sensor

Introduction

Introduction

During the last century, scientific research and technological advances have undergone a considerable revolution in various fields: medicine, information and communication transport, and others. Most of these fields are in continuous important development, which depends on many areas such as nanosciences and nanotechnologies. And thin films have been a very active field of research in science and technology for several years. The increasing use of these kind of films requires a precise knowledge of thermal properties of materials at the nanometric scale. If the thermal properties of most solid materials are well known, they may be very different for thin films considering their specific structure. It becomes necessary to know the thermal properties in question to be able to understand the transfer phenomena at different scales. This is to optimize the structure of materials according to the desired properties and to increase the performance of systems concerned by reducing the frequency of component failures and minimizing the operating cost of them.

This thesis is a part of an ANR project called Spectral Superdiffusive Phonon Sensor (SPiDER-man) led by Gilles PERNOT from LEMTA in Nancy, in association with Olivier BOURGEOIS from Néel institute in Grenoble and Stefan DILHAIRE from LOMA in Bordeaux. The main goals of SPiDER-man project are to explore and develop a new instrumentation in order to probe ultra-fast energy transfer in nanostructured semiconductors, known as ballistic-diffusive regime. This latter can be captured by the frame of Lévy Walks theory, i.e. the superdiffusive regime.

Over the past decade, rapid improvement of experimental techniques devoted to “nano” materials characterization has arisen. For instance, Time-Domain Thermoreflectance (TDTR) and Scanning Thermal Microscopy (SThM) are now well-established techniques to probe energy transport in nanostructured materials. Yet, if those approaches respectively allow spectacular temporal or spatial resolution of heat transfer at nanoscales, they can scarcely describe the ballistic-diffusive regime that exists when length scale and energy carriers mean free path are similar. The latter behavior is theoretically expected in different semiconductors. It represents a longstanding problem in nanoscale thermal transport for several engineering applications such as heat management, thermal hot spots, thermal boundary resistances, and others.

In this framework, SPiDER-man project intents to provide answers at three distinct levels:

1. The design and elaboration by mean of Molecular Beam Epitaxy tailored nanomaterial that exhibit superdiffusive behavior;
2. The development of all numerical tools valuable to understand and predict results of experiments on ballistic-diffusive regime with respect to Lévy framework;
3. The design of a new instrumentation to probe superdiffusive phonon transport in nanomaterials.

Since the early 1990's, high resolution experimental systems based on femtosecond lasers or near field probes has opened new pathways in the fields of low-dimensional physics and has provided key tools for the characterization of transport properties at the nanoscale. On the other hand, they have also highlighted unknown mechanisms and interactions demonstrating the failure of classical physical laws in nanosystems. One of the most remarkable examples of this failure is the transition between ballistic and diffusive regimes of heat transfer. The need for improved experimental characterization techniques and new ways of modelling is not yet fulfilled.

The core of this work lies on the development of new broadband thermal sensor combining two thermoreflectance measurement methods, TDTR and FDTR. In this sensor, implementation of several new technical features allows investigating thermal transport on a broad frequency range from the kHz to THz. This work provides a complete description of the phonon transport properties as a function of frequency. This, for instance, has natural applications in microelectronics where components (processors, memories...) can operate at very high frequencies and thus exhibit problems related to heat dissipation. This accurately highlights the transition between ballistic and diffusive transport that are at the core of this proposal.

The present work is divided in 4 chapters. In the first 3 chapters, we will carry out the development of the FDTR/TDTR spectral thermal sensor, and in the last one, we will seek the super-diffusive thermal regime in certain materials.

The first chapter is devoted to introduce the characterization of nanomaterial thermal properties from pump-probe thermoreflectance measurements. An inventory of the most widely used thermal characterization techniques will be carried out in the first section. Then, we will focus on the pump-probe thermoreflectance methods, especially TDTR heterodyne and FDTR used in this work. We

will describe the optical sampling of these methods and its consequences on the recorded temporal-spectral signals. For the modeling, we will introduce the Two-Temperature Model (2TM) to study the impulse response of metals, object of chapter 2. We will then describe the classic One-Temperature Model (1TM) based on Fourier law, which will allow to describe the propagation of heat in multilayer sample. In the last section, we will present a generalized identification method that aims to use the 1TM to estimate the thermal properties of studied materials. To conclude this part, we will show experimental examples of the thermal identification for a SiO_2 and Ge samples.

The second chapter is dedicated to the study the effect of the transducer on the bandwidth of the TDTR heterodyne method. We will see that the ultimate thermal resolution of the response is limited by the transducer deposited on the top of the sample. We will implement and numerically solve the Two-Temperature Model to investigate the thermal transparency of several metal films. The study will be carried out for gold (Au) and aluminum (Al) transducers, which are commonly and currently used in femtosecond pump-probe experiments, to study the effect of each film on the response. Then, we will validate this study by measuring the spectral response of Au film by the TDTR method. The simulation will finally be extended to other metals for future possible experimental uses in order to determine the optimal transducer. The work in this chapter has been published in Journal of Applied Physics.

The third chapter is devoted to the identification of the thermal properties of materials through an ultra-broadband response. First, we will study the theoretical responses and the sensitivities to the different thermal properties of the 1TM. We will present then the FDTR/TDTR spectral sensor used for thermal measurements of materials that allowed to measure the thermal response of materials over 8 decades from a few kHz to a few THz. We will show the capacity of this sensor by studying different types of material and identifying several thermal properties simultaneously. Some thermal characterization results of these materials have been published in scientific articles.

The fourth chapter aims to study the superdiffusive regime existing in alloys. We will first describe the foundations of this intermediate ballistic-diffusive regime and its physical origin. We will introduce a thermal model based on Lévy formalism allowing to describe the thermal energy motion in alloys. Using the broadband spectral sensor, we will investigate the superdiffusive behavior in InGaAs layer. We will then investigate new family of materials incorporating nano-inclusions (based on Ge) that are expected to exhibit a superdiffusive regime. In the last part of

this chapter, we will introduce the TDTR imaging method, which allows a cartographic thermal measurement. Finally, we will present the preliminary result of in-plane thermal characterization obtained for gold film.

Chapter 1

Heat transport in nanomaterials:
Measurements and identifications
of thermal properties

Chapter 1 : Heat transport in nanomaterials: Measurements and identifications of thermal properties

1.1 Introduction

Thermal characterization of materials at the sub-nanometric scale requires the use of a measurement technique adapted to the studied dimensions, the measured quantities and the operating conditions. The implementation of the experimental method is also accompanied by the development of a theoretical thermal modeling of the studied medium. The properties being measured are treated as free parameters in the model and are adjusted by an identification method to match the model response to the experimental data. The confidence interval associated with the measured values is a critical aspect depending on the measurement technique and the physical model used for the identification. This chapter introduces thermal characterization techniques of nanomaterials dedicated to the measurement of their thermo-physical properties. These approaches include experimental measurements, theoretical models of heat transfer and identification procedures.

This chapter starts by introducing the techniques used to measure the thermal transport in materials. We will give a general description of each method and the basic principles behind it. In a second part, we will focus on one of these techniques: the pump-probe thermorefectance. We will then present the various optical sampling techniques adopted in this field to reconstruct and measure the thermal response of materials.

After having described each technique, we will introduce in a third part the thermal modeling performed in thermorefectance experiments. We will start with the Two-Temperature Model which makes it possible to understand the impulse response of a metal. We will then describe the One-Temperature Model that is the asymptotic limit at long time scale of the 2TM when phonons

and electrons are thermalized. Later, in the next part, we will present a method for solving the 1TM using thermal quadrupoles. We will thus be able to obtain the thermal response at the surface of the studied material.

Finally, in the last part, we will present a generalized inverse method that aims to use the 1TM to estimate the thermal properties of materials from the experimental measurements obtained by the thermoreflectance methods. We will show examples of thermal characterization of SiO₂ and Ge samples through measurements obtained in frequency domain using the FDTR method. These examples illustrate the possibilities and performances of the method and validate our 1TM.

1.2 Measurements and processing tools for thermal property identification in solids

Measuring thermal properties of materials is not only necessary for understanding dynamics of heat carriers such as electrons and phonons, but also an important process in developing new materials with specific thermal properties for certain applications. During the last decades, several thermal characterization techniques have emerged and evolved according to the nature of materials to be studied (solid, liquid...) and to the thermal properties to be measured (thermal conductivity, thermal effusivity...). The general principle of these thermal methods is to create a heat source on the surface of the material, and to measure the temperature variation associated to the heat diffusion within the sample.

Different criteria and categories may be used to classify thermal measurement methods. Two major classes of methods can be distinguished by the nature of the thermal detection scheme. It may be either in contact with the surface of the studied sample and called contact methods (3ω method, SThM...) or without any contact with the sample, thus called non-contact methods (Flash method, thermoreflectance pump-probe...).

1.2.1 Contact methods

3 ω method

The 3ω method originated from Corbino [1-2] who discovered the third harmonic voltage component while applying a current through a heater. Later, G. D. Cahill employed this technique for the thermal characterization [3-4]. Although initially used for measuring the thermal conductivity of bulk materials, the method was later extended to thin films. This technique is currently one of the most popular methods in the research field for thermal characterization of solids [5-7].

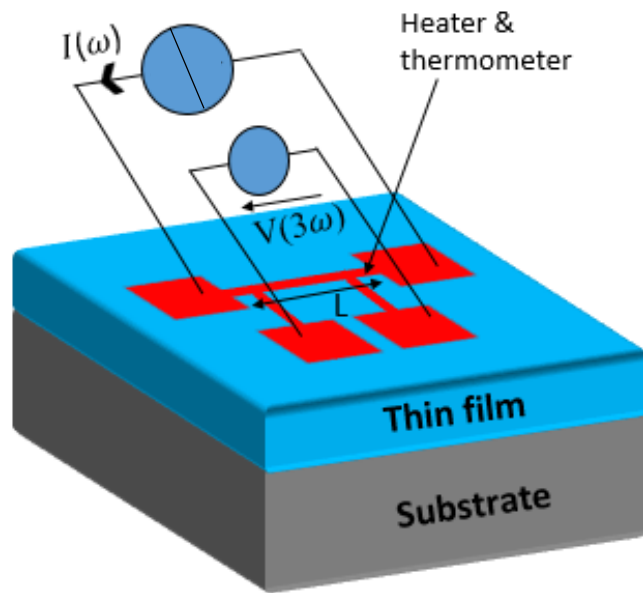


Figure 1-1: Schematic diagram of 3ω measurement for thin film material.

The 3ω method employs a metallic stripe deposited on the material surface as shown in **Figure 1-1**. The metallic line acts as a heater and a thermometer at the same time by inducing a thermal distribution and measuring the variation of the temperature in the material. To excite the stripe, an alternating current (AC) is used where its electrical signal modulated at a frequency ω ($\text{rad}\cdot\text{s}^{-1}$) can be described as:

$$I(t) = I_0 \cos(\omega t) \quad 1.1$$

By Joule effect, this electric current generates a thermal wave oscillating at a frequency 2ω that increases the temperature of the heater and subsequently of the material. The power dissipated in the metallic resistance (R) is:

$$P(t) = RI(t)^2 = RI_0^2 \cos^2(\omega t) = \frac{RI_0^2}{2} [1 + \cos(2\omega t)] \quad 1.2$$

As a result, the temperature variation at the sample surface also varies at a frequency 2ω . Because the electrical resistance of the stripe depends on the temperature, the resistance will be modulated at 2ω as well. In return, this leads to a potential difference between the electrodes since the resistance of the heater/sensor varies at this frequency (2ω) and the current varies at a frequency ω . The voltage difference V across the metal line follows the equation below:

$$V = V_{1\omega} \cos(\omega t) + V'_{1\omega} \cos(\omega t + \varphi) + V_{3\omega} \cos(3\omega t + \varphi) \quad 1.3$$

It is possible to extract the third harmonic of this signal with a lock-in amplifier. Measuring this component at two frequencies ω_1 and ω_2 , the thermal conductivity k of the thin film can be calculated by [3]:

$$k = \frac{V^3 \ln\left(\frac{\omega_2}{\omega_1}\right)}{4\pi LR^2 (V_{3\omega_1} - V_{3\omega_2})} \frac{dR}{dT} \quad 1.4$$

where $V_{3\omega_1}$ is the third harmonic of the voltage at frequency ω_1 , $V_{3\omega_2}$ is the third harmonic of the voltage at frequency ω_2 , R is the resistance of the metal strip with a length of L and $\frac{dR}{dT}$ is the rate of resistance variation with temperature.

Despite its ability to measure thermal conductivities of materials independently of their thermal capacities, the 3ω method has some disadvantages and many error sources in certain cases. One

of these latter is when the studied sample is not an electrical insulator, then a layer of insulation must be deposit between the stripe and the sample, requiring a calibration step to avoid the effect of this layer. On the other hand, this technique does not take into account the thermal interface between the stripe and the material. It also only measures the mean temperature and not local, which can generate non-negligible errors in the measured thermal conductivity of thin samples [8].

SThM method

The Scanning Thermal Microscopy (SThM) is one of the measuring techniques that is being employed to understand the thermal cartographies of the surface [9-12]. This method is based on a contact Atomic Force Microscopy (AFM), which allows to have simultaneously a topographic and a spatial mapping of the temperature or the thermal conductivity across the sample surface with a submicron spatial resolution. Instead of the conventional sharp tip used in AFM, the SThM employs a temperature sensor such as a thermocouple or a resistance thermometer. For this, several types have been implemented, especially metal probes and probes doped with silicon. The probe in SThM can be used in two different modes called passive and active, see **Figure 1-2** [13].

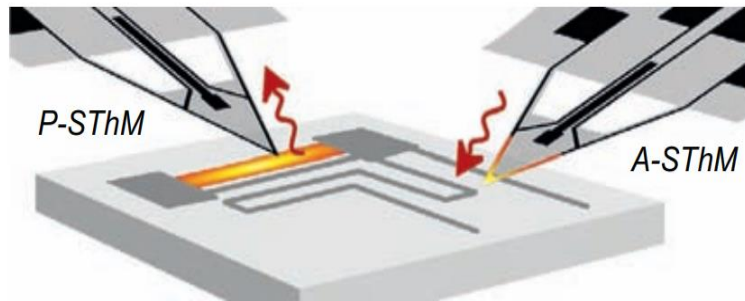


Figure 1-2: Schematic representation of the two SThM operating modes: passive (P-SThM) and active (A-SThM) [13].

In passive mode (P-SThM), the sample is heated by an external heat source and the tip takes the role of a thermometer. The local temperature is then measured by the heat flux flowing from the sample to the tip. A temperature map and a topographic image are produced simultaneously by scanning the tip across the heated sample.

In active mode (A-SThM), the tip acts as the heater and the sensor at the same time, which makes the operation of this mode very similar to the 3ω method. An electric current is used to induce Joule heating in the tip resistor. While scanning, the temperature of the tip sensor depends on the heat exchange with the sample and, therefore, on the sample local thermal conductivity [14-15]. Measuring the temperature variation as a function of the position provides an image of thermal conductance of the sample. A thermal model allows to extract the thermal conductivity map of the sample.

The SThM is a useful thermal characterization technique, but its efficiency depends on several parameters: physical and geometric properties of the used tip, the thickness of the studied sample and the surface quality [16]. In addition, the method has a difficulty to make quantitative measurements due to the thermal contact resistance.

1.2.2 Non-contact methods

Flash method

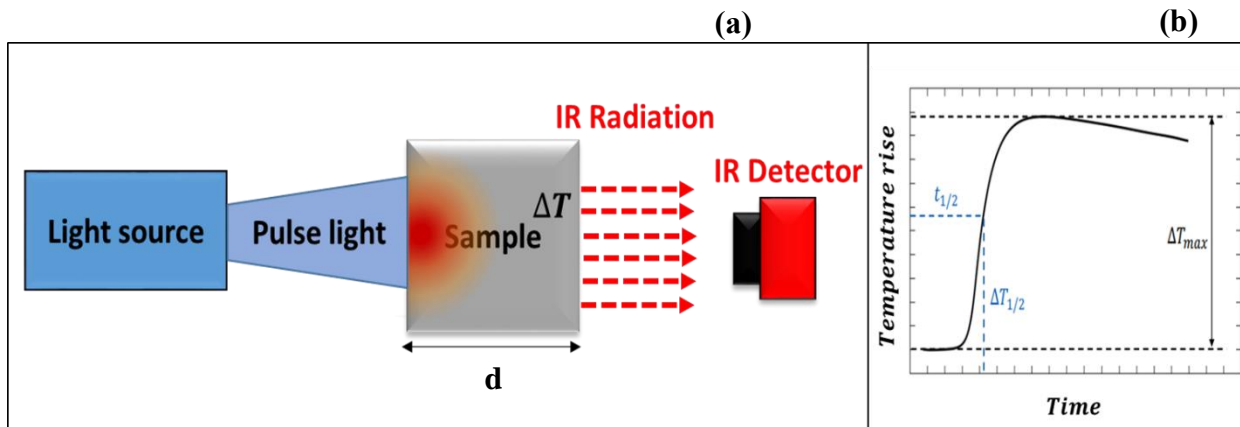


Figure 1-3: (a) Principle of the Flash method. (b) An example graph showing the measured rear side temperature rising curve.

The Flash method for measuring the thermal diffusivity of solids was first described by Parker in 1961 [17-18]. The simplicity and the speed measurement of this method have with no doubt ensured its success and considered it as a main thermal characterization technique. Its concept, as

shown **Figure 1-3(a)**, is based on radiating the front face of the sample with a short energy pulse coming from a laser source or a flash lamp. The energy will then be absorbed by the specimen and emitted again on the rear face of the sample, where a sensor (thermometer, infrared detector) measures the variation of the temperature. The thermal diffusivity value is computed from the temperature rise versus the acquisition duration as described by the following equation, by considering $t_{1/2}$ the time at which half of the maximum temperature raise (see **Figure 1-3(b)**) was reached:

$$D = \frac{1.38 d^2}{\pi^2 t_{1/2}} \quad 1.5$$

where d (m) is the thickness of the sample. The measurement of the amount of energy absorbed makes it also possible to determine the specific heat capacity ρC (J/m³/K) and then to obtain the thermal conductivity k (W/m/K):

$$k = \frac{1.38 d^2}{\pi^2 t_{1/2}} \rho C \quad 1.6$$

This method has several limitations concerning the studied specimen. Beside the fact that it requires size calibrated samples, it also requires to have a material that is able to absorb energy in the visible part of the front side and to emit an infrared radiation on the opposite side. If not, it is necessary to deposit on the studied material other layers with these properties. That makes the sample more complex and heterogeneous and the measured signal will be difficult to interpret [19].

Raman thermometry method

Raman spectroscopy is a thermal characterization technique that uses the light-backscattering phenomena to determine the local temperature vibrational properties of material [20-22]. In this thermometry method, a laser beam is used as both the heat source and the temperature sensor of

the sample. The backscattered light of the beam is collected onto a Charge Coupled Device (CCD) detector and analyzed by the Raman spectrometer.

When the incident light is absorbed at the sample surface, most of the light is elastically scattered conserving its energy, this is called Rayleigh scattering. However, a small part will be inelastically scattered with a slightly different frequency (ν) and called Raman scattering. **Figure 1-4** [23] shows this scattering mechanism.

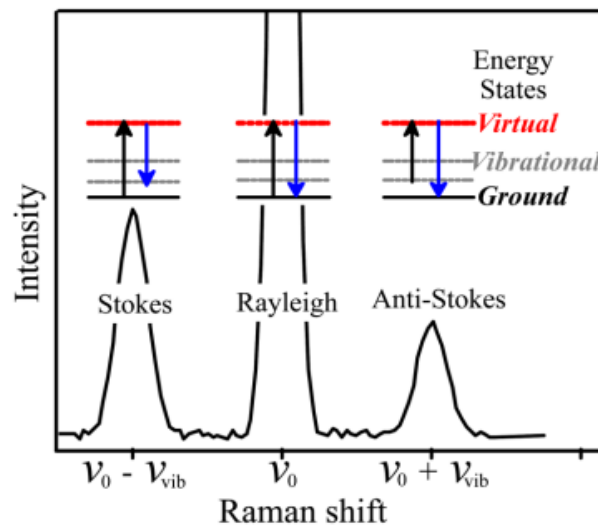


Figure 1-4: Schematic of scattering modes involved in Raman spectrometer [23].

For Rayleigh scattering, the excited electron returns to the initial state by emitting a photon with the same energy as the incident. As for Raman scattering, the excited electron does not return to its initial state and there are two cases:

- i) Stokes scattering when the electron decays to a higher level by emitting photon with lower energy than the incident.
- ii) Anti-stokes scattering when the electron decays to a lower state level and the emitted photon has a higher energy than the incident light.

In the most common approach of this method, both the Stokes and Anti-Stokes peaks are registered and their relative intensities (I_S and I_A) are correlated to the local temperature (T) by the following equation:

$$\frac{I_A}{I_S} = A \cdot \exp\left(\frac{-\hbar\omega}{K_B T}\right) \quad 1.7$$

where A is a calibration constant determined experimentally, \hbar is the Planck constant, ω is the phonon frequency, K_B is the Boltzmann constant.

The thermal conductivity can then be extracted by using a thermal diffusive model under certain assumptions taking into account the beam laser shape and the power density absorbed by the sample [24].

Raman method has several advantages in the context of thermal characterization. Among them, this technique doesn't require a sample preparation or a smooth surface for the measurement and it allows to determine the thermal conductivity of the medium without the need of its heat capacity. However, there are some drawbacks to the use of this method. Raman spectrum is very sensitive and can be affected and deformed by some contributions, such as the compositional, structural disorder and impurities of the sample [25-26]. In addition, the studied materials should have a significant Raman signal from one of its optical modes. This means that specimens like amorphous materials and metals that exhibit poor Raman signals are not good candidates to be measured with Raman thermometry [23].

Thermoreflectance

Thermoreflectance is an optical method aiming at characterizing thermal properties of materials through the reflectance change with temperature. With the advancement of pico- and femtosecond pulsed laser in the 1980s [27-28], this technique has proven itself as a very effective method to detect ultra-fast transient phenomena, which was impossible with conventional contact systems such as thermocouples. The importance of the thermoreflectance is not only for measuring thermal

properties and interfaces of nano-materials [29-32], but also for studying their acoustics and optical properties [33-36].

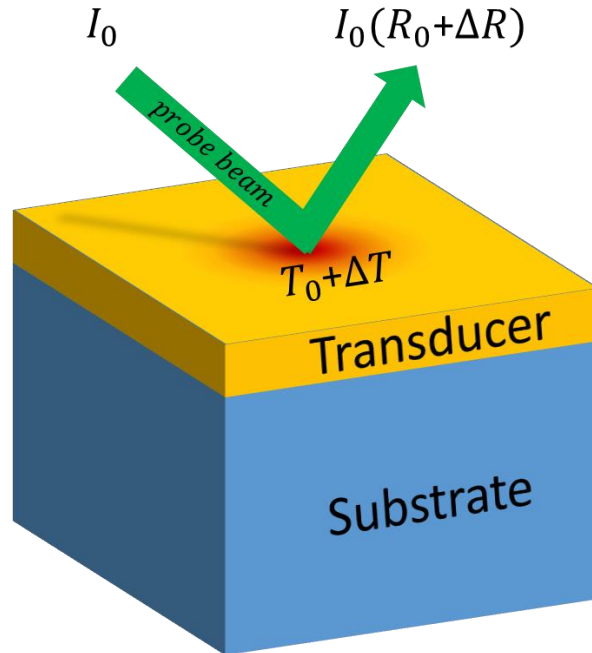


Figure 1-5: General principle of thermoreflectance

The Thermoreflectance principle shown in **Figure 1-5**, is to disturb the sample by a thermal source (laser, resistance) and generate the effects to be studied. These effects, whether they are thermal or acoustic, generate a transient modification of the reflectivity response of the medium that is detected by using a probe laser. The intensity of this beam reflected at the sample surface is directly related to the variation of reflectivity. If I_0 is the intensity of the incident probe beam, then the reflected one can be written as:

$$I_0(R_0 + \Delta R) \quad 1.8$$

where R_0 is the reflectivity of the metal at ambient temperature T_0 , and ΔR is the variation in reflectivity due to heating. The relation between the reflectivity and the temperature can be obtained by using an empirical law. Assuming that the heating induces a low rise of the temperature ΔT in the sample, an approximation of the reflectivity to first order can be obtained:

$$\begin{aligned} R(T_0 + \Delta T) &= R_0 + \Delta R \\ &= R_0 + \frac{\partial R}{\partial T} \Delta T \end{aligned} \tag{1.9}$$

Thus, the change in surface reflectivity is related to the change in temperature [37] by the following relation:

$$\frac{\Delta R}{R_0} = \left(\frac{1}{R_0} \frac{\partial R}{\partial T} \right) \Delta T = \kappa(\lambda) \Delta T \tag{1.10}$$

where $\kappa(\lambda)$ is the coefficient of the thermorefectivity that depends in particular on the thermo-optical properties of the metal as well as the considered wavelength of the probe beam λ [38]. The reflectivity measurement makes it possible to obtain the temperature variation in the studied material and determine its thermal properties.

In our work, we are interested in a pump-probe thermorefectance method with two ultra-short laser pulses (femtosecond), where the high intensity pump heats the sample and the low intensity probe senses its reflectivity response. The pump pulse is absorbed on the surface of a metallic transducer, which is used to increase the absorption and convert light into heat. Firstly, the energy of the incident pump is absorbed by the electrons of the metal and generates a non-equilibrium state with the lattice. The electrons temperature rapidly increases while the lattice remains cold, since the heat capacity of the electron is much smaller than that of the lattice. Then, the energy is transferred to the cold lattice by electron-phonon coupling until reaching the thermal equilibrium, thus causing a heat flux that propagates and dissipates in the material. This thermoelastic constraint of the lattice can also generate a mechanical wave that propagates in the form of an acoustic wave.

After this perturbation, a probe pulse arrives and reflects on the sample surface to measure the thermal and acoustic effects created by the pump. Indeed, these transient phenomena in the metal produce a change in the optical reflectivity, which induces a variation in the intensity of the probe beam reflected on the surface that can be measured by a photodetector. The transient response of

the sample can be reconstructed by creating a delay between the arrival moments of the pump and the probe on the surface.

Thermoreflectance being optical in nature, puts certain limitations on the sample choice. The main limitation is the requirement of a smooth surface, as the sample roughness does not contribute to the probe signal due to the diffuse scattering effects. This method requires also the deposition of a metal transducer layer, which complicates the thermal analysis in some cases as it introduces an additional layer with the associated deposition processes [39].

1.3 Thermoreflectance: Time-Domain vs Frequency-Domain

The interest in ultrafast transient phenomena in materials has led to the development of many measurement techniques based on thermoreflectance. These impose an optical sampling of the material response, which is achieved by the pump-probe delay, in order to detect the ultra-fast transient signal. According to this sampling, the employed techniques can be roughly grouped into time-domain methods based on the temporal delay between pump-probe pulses, and frequency-domain methods based on modulated pump laser sources.

1.3.1 Time-Domain Thermoreflectance (TDTR): synchronous optical sampling vs asynchronous optical sampling

Among the thermoreflectance measurement methods in the time-domain, two configurations are commonly used to sample the thermal response, one called synchronous and the other asynchronous.

1.3.1.1 Synchronous method

In synchronous configuration, the same laser is used as pump and probe leading to measure at exactly the same (synchronous) repetition rate the effects of the pump. For that a Titanium-Sapphire oscillator provides the femtosecond pump and probe pulses, which are separated by using a polarizing beam cube splitter. A mechanical delay is introduced into the path of the probe to modify its path length and delay its arrival on the sample surface, where the pump and probe pulses are focused by using a microscope objective. Since both the pump and the probe pulses have the same repetition rate, this method of measurement is usually called homodyne or synchronous pump-probe thermoreflectance. A schematic representation of the optical assembly of this method is shown in **Figure 1-6** [40].

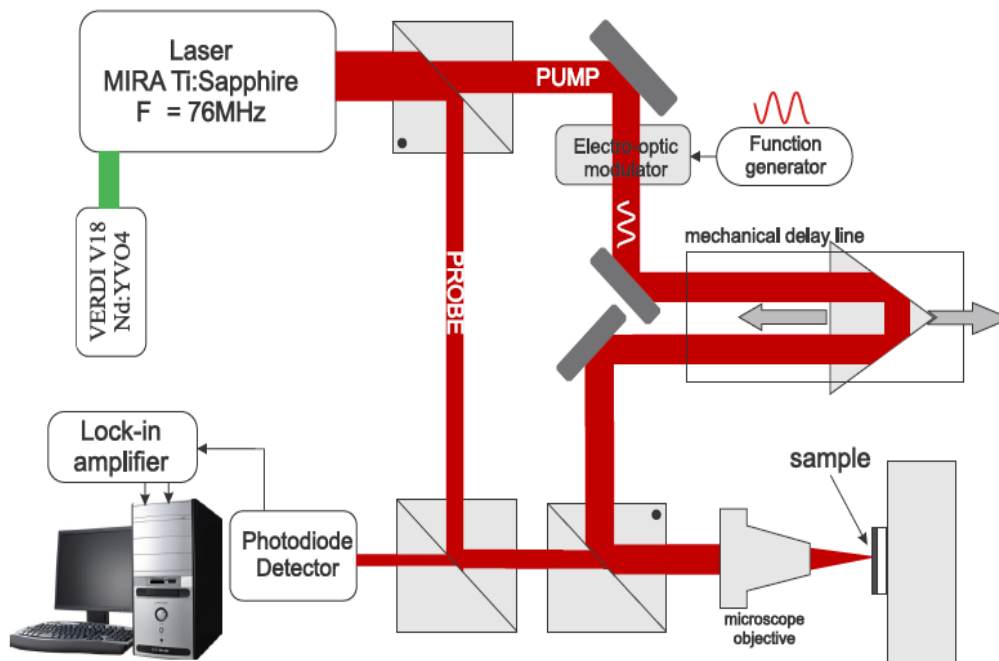


Figure 1-6: Schematic of a femtosecond pump-probe thermoreflectance measurement bench in synchronous configuration [40].

After its reflection on the sample, the probe beam is collected by a fast-response photodetector generating a signal proportional to the reflected beam intensity. The low variation of the

reflectivity ($10^{-6} < \frac{\Delta R}{R} > 10^{-2}$) and the non-negligible noises induced by the instruments of this method (mechanical vibration, laser fluctuation, electromagnetic interference) make the information hard to detect. To counter this, the pump is modulated and the energy phenomena generated by its excitation in the sample are then also modulated. A lock-in amplifier is employed after the detector that demodulates the acquired signal and extracts the information with a selective measurement around the pump modulation frequency.

The optical response of the material recorded in this configuration is sampled as a function of the pump-probe delay time at each stage position during the experiment. This sampling allows to generate a signal with a resolution of the order of femtosecond due to the translation, in which the pump-probe delay has the value:

$$\delta_s(t) = \frac{\Delta d(t)}{c} \quad 1.11$$

where c (m/s) is the celerity of the light and $\Delta d(t)$ is the length difference of the optical path from the pump and the probe to the sample. This length $\Delta d(t)$ controlled by the delay stage speed ϑ_s (mm/s) in time t :

$$\Delta d(t) = \vartheta_s \cdot t \quad 1.12$$

The transient response of the sample is reconstructed by gradually increasing the value of $\Delta d(t)$. For a 30 cm long delay line, the length difference of the optical path from the pump and the probe ($\Delta d(t)$) is increased by at best 60 cm. Considering that the celerity of light (c) in air is $3 \cdot 10^8$ m/s, the delay of the pump-probe delay ($\delta_s(t)$) cannot exceed 2 ns.

Despite its advantage, in the homodyne method there are several artifacts related to the employed mechanical delay stage. Indeed, the misalignment of this delay stage causes a pointing instability and a spot size variation on the sample surface, which affect the detected signal. These artifacts are increased by the large time range required for observation of the nanosecond transient phenomena, which imposes the need of a large magnitude delay line up to several meters. Another drawback depends on the translation speed of the stage, which introduces a mechanical vibration

during the experiment. When the traveling speed of the stage becomes faster, the vibrations increase and the shape of the thermal signal may then be affected. Therefore, it is necessary to maintain a low moving speed, which in return limits the speed of data acquisition.

1.3.1.2 Asynchronous method

In the asynchronous method, the mechanic stage is not used anymore. Instead, two different Titanium-Sapphire laser cavities are used, the first generates the pump pulses and the second the probe pulses. An asynchronous or heterodyne optical sampling is realized by fixing the pump and the probe frequencies F_p and F_s , respectively, at a slightly different repetition rate [41-42]. This frequency offset called the beating frequency ΔF is defined by:

$$\Delta F = F_s - F_p \quad 1.13$$

The pump and probe cavity lengths are actively controlled by a servo loop keeping the beat frequency constant. As their cavities are totally independent of one another, their wavelengths can be separately adjusted. The pump and probe wavelengths are chosen in order to have the highest absorption coefficient for the pump laser and the highest thermorefectance response for the probe laser, respectively. Parts of the outgoing beams are sent to a synchronization photodiode to trigger the acquisition. The reflected signal is recorded by the signal photodiode. The bench for an asynchronous pump-probe thermorefectance method is shown in **Figure 1-7** [41].

The optical sampling time resolution is ultimately limited here by the pulse duration. However, the actual time resolution is governed by the performances of the repetition rate stabilization servo loop [43]. In asynchronous optical sampling, the beat frequency acts as the delay line between the pump and the probe, and this delay depends on the time of acquisition t :

$$\delta_s(t) = \frac{\Delta F}{F_p} \cdot t \quad 1.14$$

where $F_p/\Delta F$ called the stretching factor.

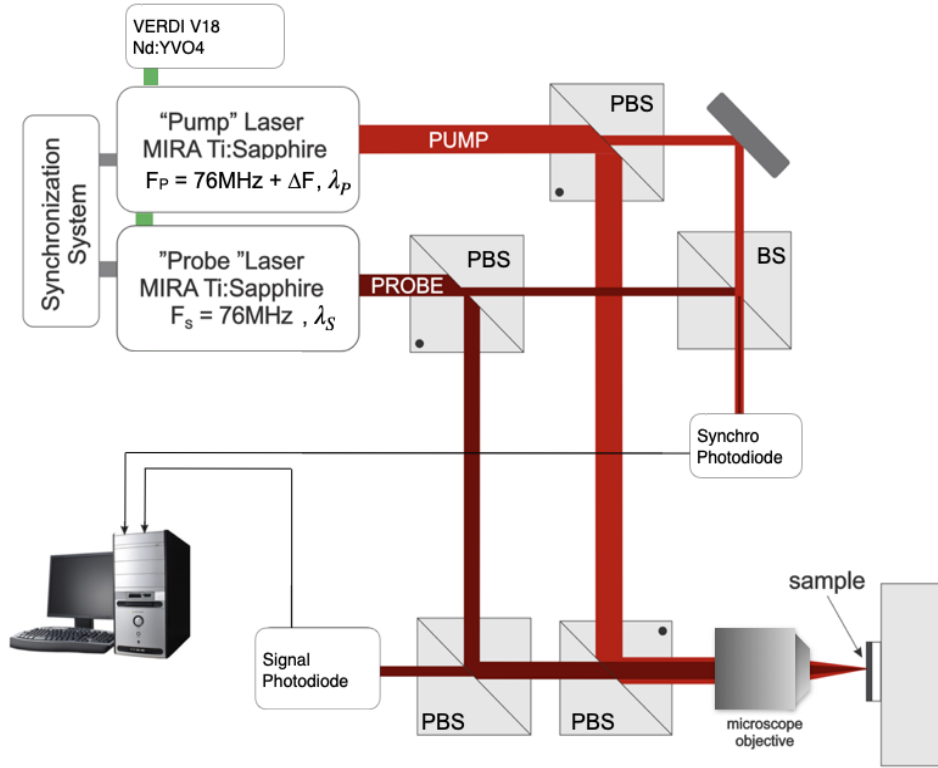


Figure 1-7: Schematic of a femtosecond pump-probe thermoreflectance measurement bench in asynchronous configuration [41].

The period of the acquired signal is then stretched into the equivalent actual time scale by a factor of $F_p/\Delta F$. **Figure 1-8** [44] details the principle of the heterodyne sampling and the orders of magnitudes of the different time scales. The transient signal, obtained by studying the variation of the intensity of the probe collected by the photodetector during a beat period, corresponds to the response of the sample dilated in time, which is similar to the strobe effect. The time resolution of the measurement is not limited by the photodetector as long as its time response τ_d satisfies the following condition:

$$\tau_d < \tau \cdot \frac{F_p}{\Delta F} \quad 1.15$$

where τ is the pulse duration of the laser pump (~ 200 fs). Hence, the beat frequency ΔF is adjusted to keep the measurement accuracy unaffected by the photodetector time response τ_d .

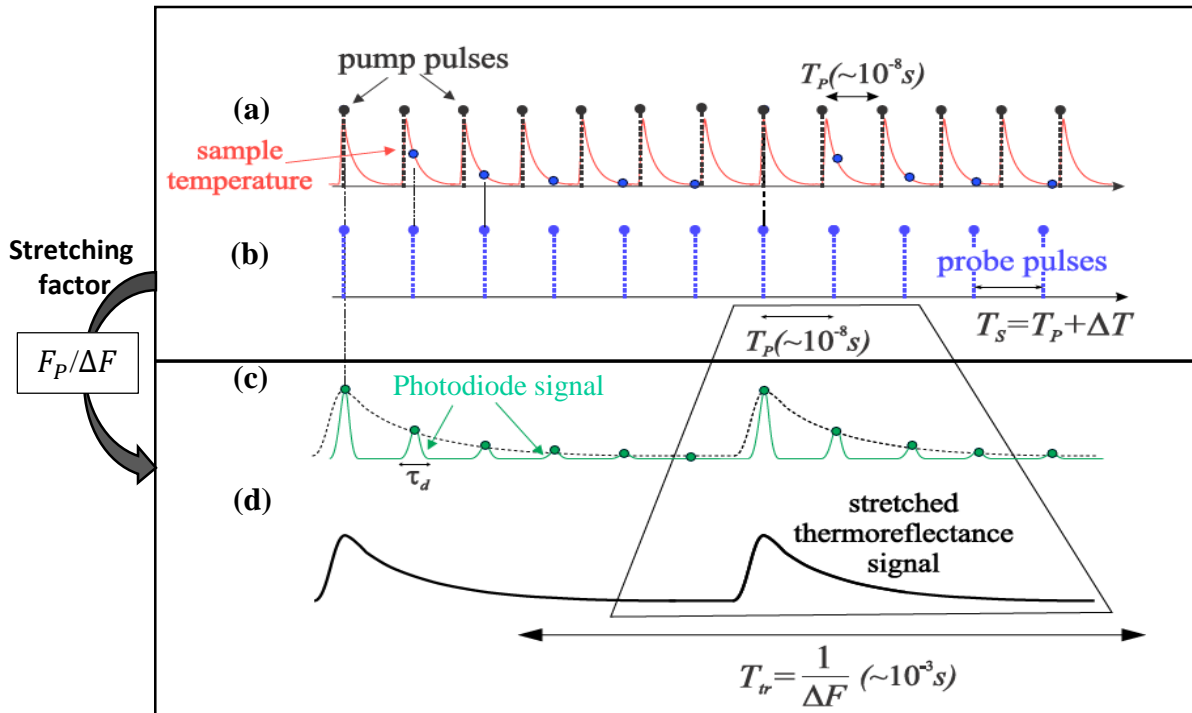


Figure 1-8: Principle of asynchronous optical sampling [44]. (a) Temperature induced reflectivity changes of the sample. (b) Probe pulse train sampling the reflectivity changes. (c) Reflected probe beam. Finally, (d) received signal by the photodetector.

Unlike the synchronous method described previously, the translation stage here is eliminated which makes it possible to avoid all the artifacts related to mechanical vibrations. In addition, the time range accessible by the heterodyne method no longer depends on the delay line but on the repetition period of the pump oscillator $T_p = 1/F_p$, which means a relaxation time up to 13.2 ns when the pump laser has a repetition rate of $F_p \sim 76$ MHz. Furthermore, the acquisition speed is often much faster ($\times 10^5$) since the time required to obtain the measurement response is now the inverse of the beat frequency ΔF instead of being limited by the speed of movement of the mechanical translation stage. **Table 1-1** compares the time acquisition in synchronous and asynchronous configurations. For an acquisition time identical to that of the asynchronous method (2 ms), it should be necessary to move the translation stage with a speed of 1000 m/s (\sim Mach 3).

The fast data acquisition in asynchronous method allows to average many repeated measurements, significantly reducing the detection noise to a very low level without using a lock-in amplifier.

Configuration Parameter	Synchronous	Asynchronous
Delay stage speed	$\vartheta_d=10^{-2}$ m/s	none
Beating frequency	none	$\Delta F=500$ Hz
Delay pump-probe variation	$\vartheta_d/c =6.10^{-11}$	$\Delta F/F_p =6.10^{-6}$
Acquisition time of a period	200 s	$1/\Delta F =2.10^{-3}$ s
Time for 10^5 average	~ 6 years	200 s

Table 1-1: Acquisition time characteristics in synchronous and asynchronous configuration.

1.3.2 Frequency-Domain Thermorefectance (FDTR)

In the frequency-domain thermorefectance technique, the thermorefectance effect is measured with respect to the modulation frequency of the pump laser. The pump beam heats the sample surface periodically at a frequency f_m , and the probe beam senses the temperature variation through a proportional change in surface reflectivity [45-46]. A FDTR method can be implemented with either a pulsed laser source with high repetition pulse rate or with two continuous wave lasers (CW). The first one is convenient for doing FDTR measurements with a TDTR system by holding the delay stage at a fixed location, while the last is significantly less expensive and less complex. Hereafter, we describe the system comprising the two continuous diode lasers.

The FDTR setup, typically as shown in **Figure 1-9**, uses two different CW laser sources, one as the pump beam and the other as the probe beam. The intensity of the pump beam is modulated either directly by a function generator or by passing the beam laser through an electro-optic modulator. For both modulation methods, the modulation frequency range is generally swept from a few kHz up to a few tens of MHz. The pump and probe beams are sent and focused onto the sample with the same objective. After the reflection, the intensity of the probe is detected by a photodiode, where a band pass filter is placed in front of it to block the pump return.

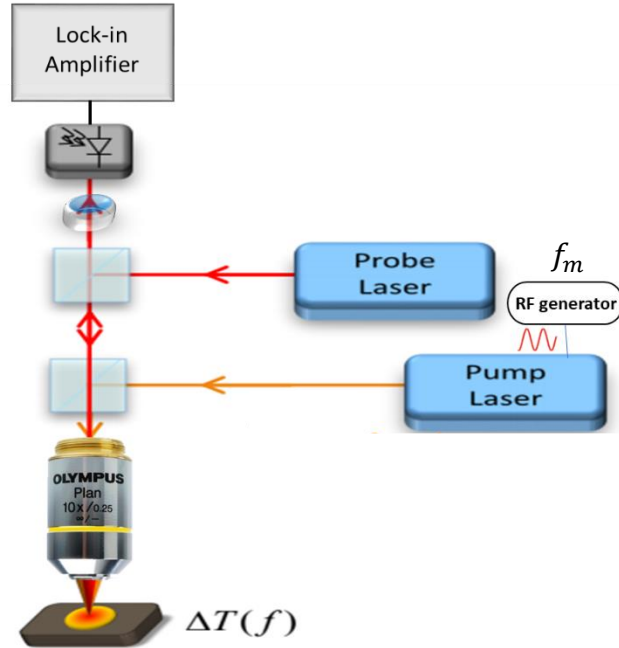


Figure 1-9: Schematic of a typical frequency-domain thermoreflectance.

The temperature of the sample lags behind the heat source because the sample needs time to absorb the thermal energy deposited by the pump. This delay in temperature depending on the thermal properties of the sample is represented in the frequency-domain by a phase lag φ_{therm} . A lock-in amplifier synchronized on the pump frequency is employed to measure the phase and magnitude of the thermoreflectance signal from the reflected probe beam intensity. An important aspect of FDTR is to accurately determine the thermal phase signal φ_{therm} . The measured phase signal of the probe φ_{probe} is actually a sum of contributions:

$$\varphi_{probe} = \varphi_{therm} + \varphi_{instrum} + \varphi_{path} \quad 1.16$$

where the second component $\varphi_{instrum}$ is introduced by the electronic instruments of the setup and the cables, and the last component φ_{path} is introduced by the different optical path lengths of the beam [23]. In order to eliminate these additional phase shifts, a common approach is used in FDTR called the calibration measurement, where the phase signal is measured from the reflected pump. In this approach, the probe beam is blocked, and the bandpass filter is removed from the

photodetector. Besides, the optical path of the reflected pump from the sample to the photodetector should be identical to that of the reflected probe. Hence, the pump laser is modulated over a prescribed frequency range and the measured phase signal would be:

$$\varphi_{pump} = \varphi_{instrum} + \varphi_{path} \quad 1.17$$

The thermal signal φ_{therm} can thus be deduced by subtracting the calibration signal, being the pump phase, at each frequency from the probe signal. After this processing, it becomes possible in data analysis to extract the desired thermal properties of the studied sample. FDTR has multiple advantages, it is a low-cost method by using continuous lasers and its measurements offer a good thermal sensitivity for thin films.

After this overview of thermorefectance techniques, we will now present the heat transfer models used in FDTR and TDTR measurements to study the thermal properties in materials.

1.4 Modeling thermal transport in thermorefectance experiments

The ultra-short pulses used in thermorefectance are essential for determining the time resolution of the system, while simultaneously inducing non-equilibrium heat in the metal transducer deposited on top of the material. The rate of energy deposition is so rapid that there exists a brief period following the pulsed heating event where the electrons and phonons are not in thermal equilibrium. A Two-Temperature Model is employed to predict this thermal inequality and describe the dynamics of the energy carriers in the heated sample. Furthermore, when the local thermal equilibrium is achieved, the thermal transport tends to a classical diffusion model based on Fourier's law. In this model, the occupation of all thermal excitations of electrons and phonons must be well described by a single temperature, hence its naming, the One-Temperature Model. In this section, we are going to present the 2TM and the 1TM used for modeling the thermal transport in thermorefectance.

1.4.1 Dynamics of electrons and phonons: Two-Temperature Model (2TM)

In order to assess the temporal response in thermoreflectance and characterize the dynamics of heat carriers, we will incorporate the time dependence in the Fermi-Dirac distribution via the electrons and phonons temperature. When considering the evolution of the absorbed energy in the metal irradiated by ultra-short laser pulses, we can distinguish three processes [47] occurring at successive time intervals as shown in **Figure 1-10**. When an optical pulse interacts with the surface of a metallic film, the electrons absorb the energy of the photons in the volume characterized by the optical penetration depth. A thermalization of the electrons occurs by electron-electron collisions within hundreds of femtoseconds, producing a Fermi distribution of hot electrons with a well-defined temperature T_e (**Figure 1-10(a)**). Once the thermal equilibrium is reached among the electrons, the physical situation of the system is modelled by a bath of hot electrons in a cold lattice, which can be described by two separate temperatures T_e and T_p (**Figure 1-10(b)**). The electrons then transmit their energy to the lattice via electron-phonon interactions, which leads the entire system to a thermal equilibrium in several picoseconds (**Figure 1-10(c)**).

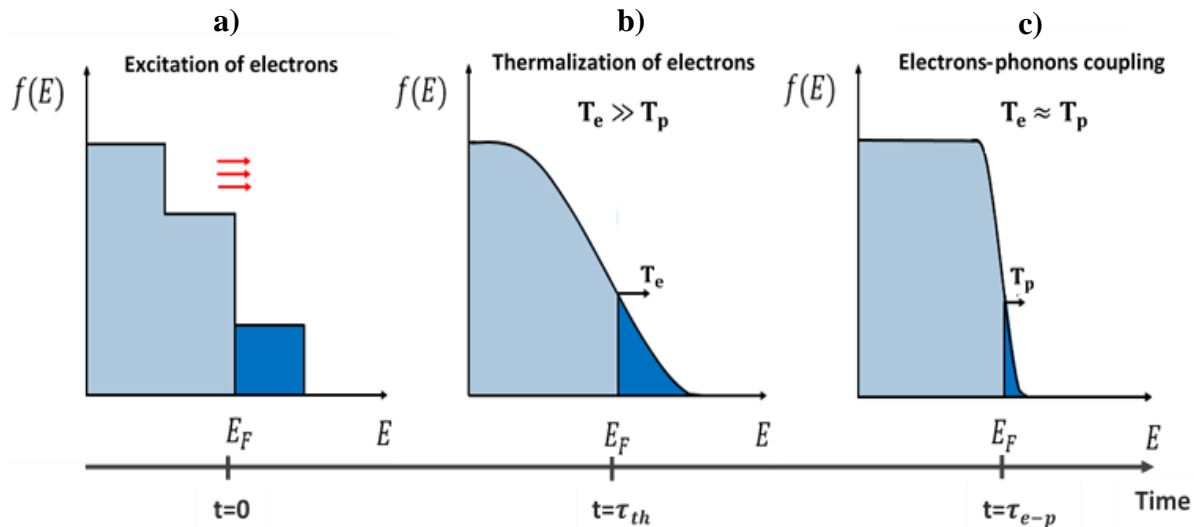


Figure 1-10: Schematic of electronic distributions in the metal after excitation by laser pulses. (a) Absorption of photons at $t=0$ generating no-equilibrium electrons. (b) At $t=\tau_{th}$ electrons have been thermalized forming a Fermi distribution. (c) Electrons reach the equilibrium with the lattice at $t=\tau_{e-p}$.

The temporal and spatial evolution of the temperature, and the energy exchanges between the electrons and the lattice in the metal are given by a system of non-linear coupled differential equations called the Two-Temperature Model originally proposed by Anisimov [48]. It can be written in the following form:

$$\begin{aligned}\rho C_e(T_e) \frac{\partial T_e}{\partial t} &= \nabla(k_e(T_e) \nabla T_e) - g(T_e - T_p) + q(\vec{r}, t) \\ \rho C_p \frac{\partial T_p}{\partial t} &= \nabla(k_p \nabla T_p) + g(T_e - T_p)\end{aligned}\tag{1.18}$$

where $\rho C_e = \gamma_e T_e$ (J/m³/K) is the specific heat capacity of electrons that is proportional to T_e and $k_e = k_{e0} \frac{T_e}{T_0}$ (W/m/K) is the thermal conductivity with T_0 (K) being the ambient temperature. The g (W/m³/K) term stands for the electron-phonon coupling constant and $q(\vec{r}, t)$ stands for the absorbed power volume density due to the laser optical pulse (\vec{r} is the position vector). Finally, ρC_p (J/m³/K) and k_p (W/m/K) are the specific heat capacity and the thermal conductivity of the metallic lattice, respectively, and are assumed to be constant due to the low temperature variation of the phonons.

The Two-Temperature Model makes it then possible to couple the two equations describing the thermal part of the sample. This model shows that the energy absorbed by the electrons relaxes in the metallic lattice due to the electron-phonon coupling, where the electronic temperature T_e decreases and that of the phonon increases T_p until reaching an equilibrium temperature. The heat generated after this equilibrium diffuses through the film and causes heat dissipation in the metal. The solving of the Two-Temperature Model to predict the time dependence of heat carriers, electrons and phonons, can be carried out numerically by the finite element method, which will be detailed in Chapter 2.

Once the thermal equilibrium is reached between electrons and phonons in excited materials medium, the thermal transport can be described by the classical 1TM. This model that is an asymptote of the 2TM at long time scales will be presented next.

1.4.2 Fourier heat transport: One-Temperature Model (1TM)

The One-Temperature Model, deduced from Fourier's law, has been used well in thermoreflectance experiments to describe the thermal response in material. The heat diffusion equation of this model is a valid description of the heat flux when all quasiparticles of electrons and phonons are in local thermal equilibrium, which occurs after exciting the metal transducer in a few picoseconds. This thermal equilibrium makes it possible to consider the temperature of the heat carriers to be uniform. Then, this assumption enables researchers to use the 1TM to predict the heat diffusion within the studied sample instead of the 2TM.

In Fourier's law of heat conduction [49], the heat flux $\vec{\phi}$ is proportional to the magnitude of the temperature gradient through the material thermal conductivity k , which is the sum of k_e and k_p . For a unidirectional conduction process this observation may be expressed as:

$$\vec{\phi} = -k\vec{\nabla T} \quad 1.19$$

The time is not involved in this relation indicating the instantaneity between the flux and the temperature gradient. The law of conservation of energy is used allowing for the derivation of what is known as the heat diffusion equation which can therefore be expressed in the following form:

$$\frac{\partial T}{\partial t} = \frac{1}{\rho C} \nabla[k\nabla T] \quad 1.20$$

The resolution of the heat equation that will be detailed in the next part makes it possible to determine the spatial distribution and the temporal evolution of the temperature in the studied medium according to its thermal properties.

1.5 Solving 1TM by quadrupole method

We are going in this part to set the bases of the One-Temperature Model used to describe the heat transfer obtained during a pump-probe experiment. Let us suppose that the multilayer sample, submitted to an excitation laser, has cylindrical symmetry around its axis of propagation, which is valid by considering the shape of the Gaussian beams. Assuming that the material is isotropic, the thermal response therefore also exhibits cylindrical symmetry. The material as shown **Figure 1-11** is made up of several layers deposited on a semi-infinite substrate and covered by a film of transducer. Then, the heat flux in each layer i is governed by the heat transport equation (1.20) with cylindrical geometry:

$$\rho_i C_i \frac{\partial T_i(r, z, t)}{\partial t} = k_i \left(\frac{\partial^2 T_i(r, z, t)}{\partial r^2} + \frac{1}{r} \frac{\partial T_i(r, z, t)}{\partial r} + \frac{\partial^2 T_i(r, z, t)}{\partial z^2} \right) \quad 1.21$$

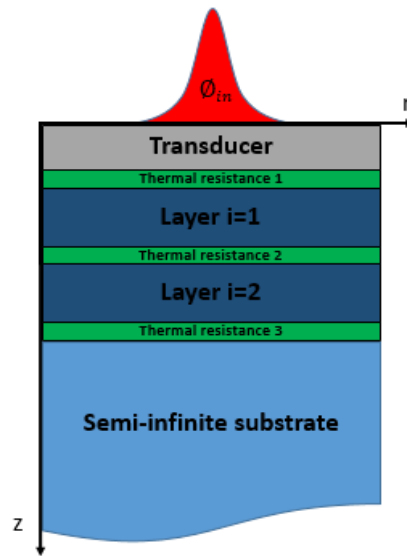


Figure 1-11: Modeling of a multilayer sample.

With the following conditions of continuity of the temperature field imposed on the material surface:

$$\frac{\partial T(r, z = 0, t)}{\partial r} = 0 \quad \text{for } r = 0 \text{ and } r \rightarrow \infty \quad 1.22$$

The resolution of this type of system can be handled in different ways. In the following paragraph, we will present a method based on the integral transformation of the heat equation, called the thermal quadrupole method. The importance of this method lies in its analytical character making the resulting formalism transparent, and in its rapid calculations making it a method well suited to system optimization.

1.5.1 Thermal quadrupole formalism

The thermal quadrupole method, extending the notion of electrical quadrupole, was initially proposed by Carslaw and Jaeger [50]. The couple voltage and current, connected by the quadrupole at the input and the output of an electrical system, is replaced by the couple temperature and heat flux in a thermal one, respectively. In this latter, each layer is represented by a matrix 2x2 containing all the thermal properties as represented in **Figure 1-12** [40].

This method determines the intrinsic relationship in the system and relates the boundary conditions to each other. This type of analogy is possible by involving a Laplace transform over time and Fourier transform to linearize the spatial dependence. By applying these two transformations, Laplace on the variable t and Hankel on the variable r , the equation 1.21 becomes:

$$\frac{\partial^2 \theta_i(\alpha, z, p)}{\partial z^2} - \left(\alpha^2 + \frac{\rho_i C_i}{k_i} \right) \theta_i(\alpha, z, p) = 0 \quad 1.23$$

where α (m^{-1}) is Hankel variable, p (s^{-1}) is Laplace variable and θ_i the temperature in Laplace-Hankel space. The solution of this differential equation can be written as:

$$\theta_i(\alpha, z, p) = \vartheta_i^{(1)} \cosh(q_i z) + \vartheta_i^{(2)} \sinh(q_i z) \text{ with } q_i = \sqrt{\alpha^2 + \frac{\rho_i C_i}{k_i} p} \quad 1.24$$

where $\vartheta_i^{(1)}$ and $\vartheta_i^{(2)}$ are integration constants. Using Fourier's law, we can obtain the expression of the heat flux in the Laplace-Hankel space as follow:

$$\phi_i(\alpha, z, p) = -k_i q_i \vartheta_i^{(1)} \sinh(q_i z) - k_i q_i \vartheta_i^{(2)} \cosh(q_i z) \quad 1.25$$

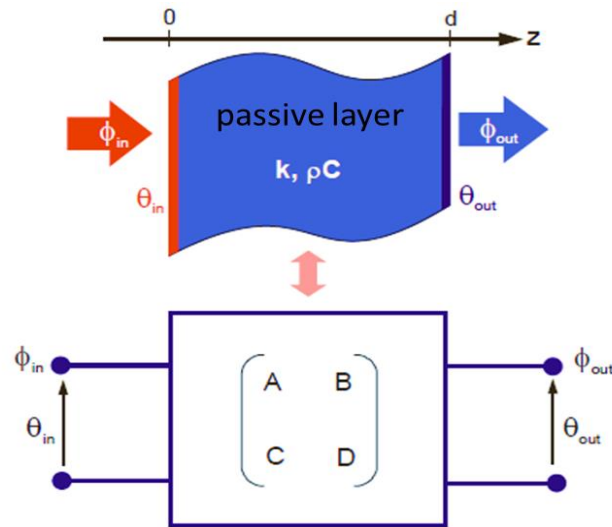


Figure 1-12: Modeling diagram of a passive layer by the thermal quadrupole method [40].

By using the quadrupole matrix formalism, the temperature-flux couple at the input and at the output of each layer can be linked in the form below:

$$\begin{bmatrix} \theta_{i,in} \\ \phi_{i,in} \end{bmatrix} = \begin{bmatrix} A_i & B_i \\ C_i & D_i \end{bmatrix} \begin{bmatrix} \theta_{i,out} \\ \phi_{i,out} \end{bmatrix} \quad 1.26$$

The elements A, B, C, and D of the matrix can be deduced from the equation. For a layer, these elements only depend on its thickness d_i and on its thermal properties:

$$\begin{aligned} A_i &= D_i = \cosh(q_i d_i) \\ B_i &= \frac{1}{q_i k_i} \sinh(q_i d_i) \\ C_i &= q_i k_i \sinh(q_i d_i) \end{aligned} \quad 1.27$$

One can deduce that the transfer matrix of a multilayer system is the product of the matrices relating to the different layers.

1.5.2 Particular cases and conditions

In order to solve the matrix of a multilayer system and obtain the surface temperature, several factors must be noted: the thermal resistance matrix, the boundary conditions and the heat flux imposed on the surface of the sample.

1.5.2.1 Thermal resistance

The thermal resistance is the break of the temperature field that exists at the interface between two thermally thick layers. Indeed, a significant discontinuity of the physical properties appears at the junction between two layers, as the disagreement caused in distribution of mesh between two materials of different nature. In addition, the imperfection of the layer deposition process and the crystallization state leads to the creation of the thermal resistance (R_i) at the interface, which is simply expressed in the following matrix form:

$$\begin{bmatrix} \theta_{i,in} \\ \phi_{i,in} \end{bmatrix} = \begin{bmatrix} 1 & R_i \\ 0 & 1 \end{bmatrix} \begin{bmatrix} \theta_{i,out} \\ \phi_{i,out} \end{bmatrix} \quad 1.28$$

1.5.2.2 Boundary conditions

The boundary conditions imposed in the quadrupole method are related to the transducer and to the substrate, which are parts of the sample. The transducer, as described before, is a metallic film of about ten nanometers deposited above the sample to enable the conversion of the pump beam into heat and the measurement of the surface temperature by the probe beam. This metallic transducer can be modelled by two layers. The first one is the upper layer with few nanometers thickness corresponding to the penetration depth e_0 in which the light is absorbed, and the other one is where the heat generated diffuses. As the heat is dissipated and instantly thermalized in the first nanometers of the metal, the temperature can be considered uniform within the penetration depth. The transfer matrix for this layer is then written:

$$M_t = \begin{bmatrix} 1 & 0 \\ k_0 e_0 q_0^2 & 1 \end{bmatrix} \quad 1.29$$

The substrate is a massive material on which the layers of interest are deposited. It is generally very thick ($> 100 \mu\text{m}$) and can be considered as a thermally opaque medium, and therefore semi-infinite. This last hypothesis imposes that no heat flux reaches the bottom at the output of the substrate. According to the transfer matrix of a layer and when the output heat flux $\phi_{sub,out}=0$, the flux and the temperature at the input of the substrate are:

$$\begin{aligned} \theta_{sub,in} &= \cosh(q_{sub} d_{sub}) \theta_{sub,out} \\ \phi_{sub,in} &= k_{sub} q_{sub} \sinh(q_{sub} d_{sub}) \theta_{sub,out} \end{aligned} \quad 1.30$$

The ratio of the flux and the temperature at the input of the thick substrate is then:

$$\frac{\phi_{sub,in}}{\theta_{sub,in}} = k_{sub} q_{sub} \tanh(q_{sub} d_{sub}) \xrightarrow{d_{sub} \rightarrow \infty} k_{sub} q_{sub} \quad 1.31$$

Thus, the semi-infinite substrate can be represented as an impedance Z :

$$Z = k_{sub} \sqrt{\alpha^2 + \frac{\rho_{sub} C_{sub}}{k_{sub}} p} \quad 1.32$$

1.5.2.3 Input flux: laser source

The input flux deposit by the laser excitation can be represented by a product of a temporal variable and another spatial one. The temporal variable is a Dirac function that translates the short duration of the laser pulse in reference to the time scale of the experiment, while the spatial variable is a Gaussian function representing its spatial extent. The source term is then written as:

$$\phi_{in}(r, z = 0, t) = Q e^{-\frac{r^2}{r_p^2}} \cdot \delta(t) \quad 1.33$$

Since the quadrupole method solves the heat equation in Laplace-Hankel space, the equation becomes:

$$\phi_{in}(\alpha, z = 0, p) = Q \left(\frac{r_p^2}{2} \right) e^{-\frac{r_p^2}{4} \alpha^2} \quad 1.34$$

where Q (w/m^2) is the power density term and r_p (m) is the radius of the laser spot on the surface.

1.5.3 Expression of the surface temperature

After modeling the matrix heat transfer of the transducer and the thermal resistance, we can then represent the multilayer system shown in **Figure 1-11**, a sample of two layers deposited on a semi-infinite substrate and covered by a metallic transducer, by the following transfer matrix:

$$\begin{aligned} \begin{bmatrix} \theta_{tr,in} \\ \phi_{tr,in} \end{bmatrix} &= \begin{bmatrix} 1 & 0 \\ k_0 e_0 q_0^2 & 1 \end{bmatrix} \begin{bmatrix} A_{tr} & B_{tr} \\ C_{tr} & D_{tr} \end{bmatrix} \begin{bmatrix} 1 & R_{tr/1} \\ 0 & 1 \end{bmatrix} \begin{bmatrix} A_1 & B_1 \\ C_1 & D_1 \end{bmatrix} \\ &\times \begin{bmatrix} 1 & R_{1/2} \\ 0 & 1 \end{bmatrix} \begin{bmatrix} A_2 & B_2 \\ C_2 & D_2 \end{bmatrix} \begin{bmatrix} 1 & R_{2/sub} \\ 0 & 1 \end{bmatrix} \begin{bmatrix} \theta_{sub,in} \\ \phi_{sub,in} \end{bmatrix} \end{aligned} \quad 1.35$$

which can be rewritten as:

$$\begin{bmatrix} \theta_{tr,in} \\ \phi_{tr,in} \end{bmatrix} = \begin{bmatrix} N_{11} & N_{12} \\ N_{21} & N_{22} \end{bmatrix} \begin{bmatrix} \theta_{sub,in} \\ \phi_{sub,in} \end{bmatrix} \quad 1.36$$

By using the boundary conditions, in particular the hypothesis of the infinite substrate in equation 1.31, the final expression of the Laplace-Hankel temperature at the transducer surface can be obtained:

$$\theta_{tr,in}(\alpha, z = 0, p) = \left(\frac{N_{11} + k_{sub} q_{sub} N_{12}}{N_{21} + k_{sub} q_{sub} N_{12}} \right) \phi_{tr,in}(\alpha, z = 0, p) \quad 1.37$$

This result is still in the transform domain. To have the frequency response in real space, the inverse Hankel transform must be applied. This will be elaborated furthermore in chapter 3. As for Laplace transform, one gets the real time numerically by Gaver-Stehfest algorithm [51].

1.6 Inverse method for thermal parameters identifications

The thermal characterization requires a comparison of the experimental data with the theoretical model of the heat transfer in the studied system. The properties being measured are treated as free parameters in the model and are adjusted by an inverse method, which is an optimization to match the model to the experimental data. In this section, we will first describe the inverse method used in this work for thermal identification. In a second step we will show examples of thermal parameters identification of silica and germanium layers obtained from experimental measurements carried out with the FTDR method. Finally, we end this chapter with describing the uncertainty sources in the inverse method.

1.6.1 Direct Problem / Inverse Problem

The direct problem enables to describe the response of a physical phenomenon from the bias of analytical or numerical solutions, and the knowledge of the input parameters such as the physical properties. In the case of a thermal study, the direct problem contributes by knowing the information about the heat source and the thermo-physical properties to calculate the temperature response of the system under study. The direct problem can be reversed to an indirect problem, which consists in determining one or more unknown input parameters from the measured response. The inverse term recalls that we use the information concerning the physical model "in reverse" knowing the outputs and seeking to go back to certain input characteristics. Therefore, the inverse problem allows in thermal domain to estimate the input parameters of the direct problem from the temperature measurement, such as the thermo-physical properties, flux, etc. This estimation of parameters can take various forms and is found in many fields of application, such as physical and engineering sciences, seismology, imaging, chemistry, economics and finance [52]. A diagram shows the principle of the direct and inverse problem for a thermal study in **Figure 1-13** [53].

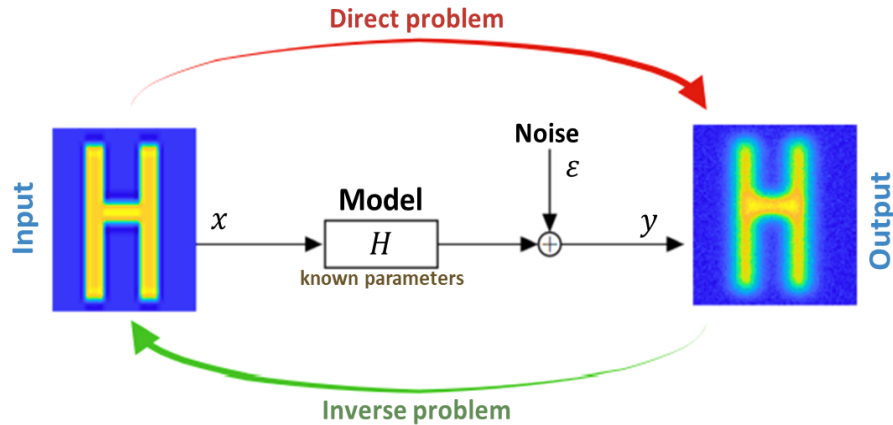


Figure 1-13: Schematic of the direct and inverse problem principle [53].

In a direct problem, the convolution between the known input parameters x and the function model H makes it possible to calculate the response y , which is expressed by the following equation:

$$y = x * H + \varepsilon \quad 1.38$$

where ε refers to the noise that may exist in this direct process. This noise appears in the form of uncertainties on the estimated input parameters

In the case of an inverse problem, the unknown causes x is determined from the observation y [54]. Solving such a problem must respect the notion “well posed problem” introduced by Jacques Hadamard [55]. This notion recommends that the solution of the problem must satisfy three conditions: a solution exists, the solution is unique, and it changes continuously with the initial conditions. If one of these conditions is not respected, the problem is then badly posed. Often in inverse problems of a thermal study, the first conditions are satisfied because a physical reasoning proves the existence. Moreover, if the solution is not unique, additional restrictions and information are needed to isolate a single solution. Finally, the continuity condition is without a doubt the most important and can cause the most problems, as it determines the stability of the problem and the errors that may occur in the obtained solutions.

1.6.2 Mathematical description of the inverse method

The inverse problem can be put in the form of an identification process, which consists in finding the unknown parameters from the experimental measurement. The unknowns are determined in such a way that they minimize the difference between the measurements of a system and the theoretical results calculated by the model. The identification of the parameters itself requires two distinct steps. First of all, it is necessary to put the mathematical problem in an adequate shape, then to choose an object function, also called criterion, that contains the observation and the input parameters. The estimation of the unknown parameters then consists in adopting as solutions the values which minimize this object function.

In this work, we used the function of least mean squares to identify the thermal parameters. This method consists in minimizing the sum of the quadratic errors between the experimental signal $y_{exp}(f)$ and the signal calculated by the theoretical model $y_{cal}(f)$. The least mean squares are represented by the following equation:

$$L_u = \sum_{i=1}^N |y_{cal}(f_i, X_u) - y_{exp}(f_i)|^2 \quad 1.39$$

where N is the number of samples, f is the frequency and $X_u (X_1, X_2, \dots, X_u)$ is the vector containing u unknown parameters that we aim to estimate.

The second step is the optimization, where the unknown properties are treated as free parameters in the heat transfer model. These properties are adjusted to minimize the difference of the functional equation at each frequency and find a minimum. The search for this minimum is carried out by an iterative methods, such as the algorithms of gradient-descent, genetic, Levenberg-Marquardt or even the Newton method [56]. We chose an algorithm of Levenberg-Marquardt already implemented in the Matlab optimization toolbox.

The Levenberg-Marquardt algorithm finds a local minimum starting at an initial guess of the parameter values. In systems where there is only one minimum, the logarithm will converge to this

global value even if the initial guess is arbitrary. On the other hand, in systems with several minima, the optimization algorithm leads to a different local minimum according to the initial value. To avoid this problem, especially that the non-linearity of the heat equation in a thermal system can cause the local minimum to be excited, we can launch several optimization procedures using different initialization values [57].

1.6.3 Experimental examples of SiO₂ and Ge thermal identification

In order to illustrate the identification method by the One-Temperature Model, we will show a study of thermal properties characterization of silica dioxide and germanium layers. The study was carried out in the frequency domain by the FDTR measurement method. The experiment was realized with a wavelength of 808 nm for the pump and 786 nm for the probe. In addition, the two beams were focused on the sample with an objective 10X.

Silica dioxide SiO₂

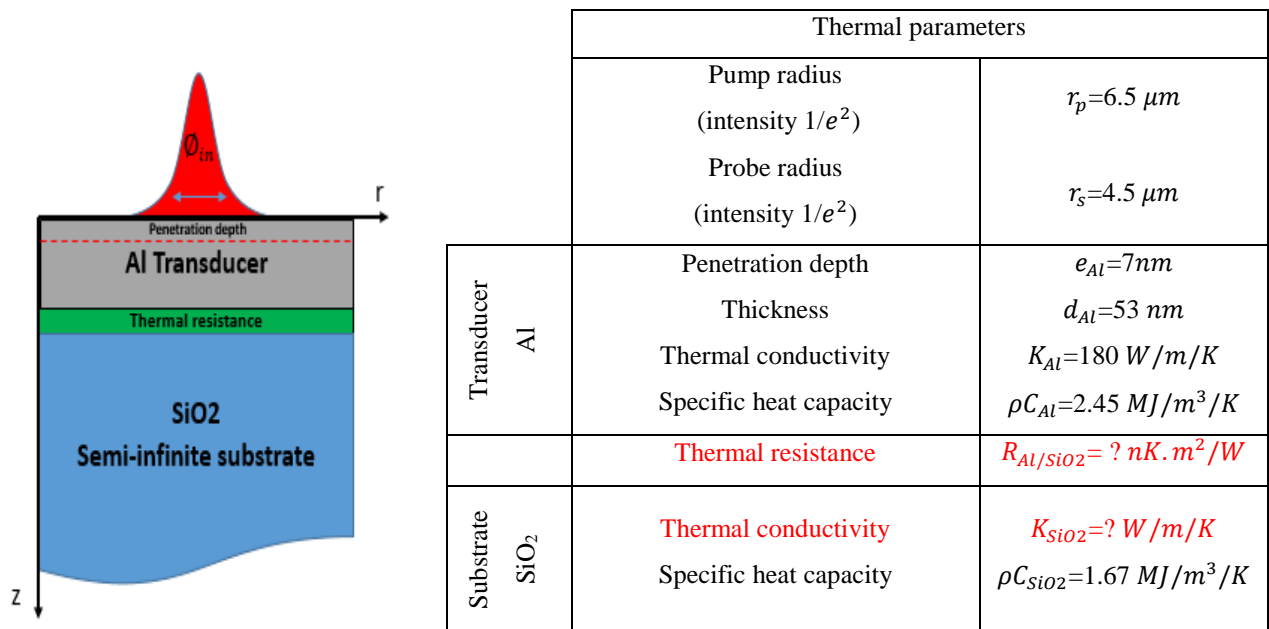


Figure 1-14: Schematic description of the sample Al/SiO₂ with the thermal properties used for the identification.

The structure of the studied sample is a semi-infinite substrate of SiO_2 , on which was deposited a thin layer of aluminum of 70 nm with the role of transducer, as described previously. **Figure 1-14** presents a schematic description of this sample, with a table showing the necessary properties for the optimization.

The thermal properties of the aluminum transducer as well as the heat capacity of the silica substrate are assumed to be known. Two parameters are left free during the identification procedure. The first one is the thermal conductivity of SiO_2 (k_{SiO_2}) and the other one is the thermal resistance at the interface between the aluminum transducer and the SiO_2 substrate ($R_{\text{Al/SiO}_2}$). The numerical optimization is realized on both the magnitude and the phase measurement response obtained by the FDTR method. The pump laser was modulated in a frequency range extending from 10 kHz to 30 MHz. The optimization results as well as the residuals obtained in the two cases are presented in **Figure 1-15**.

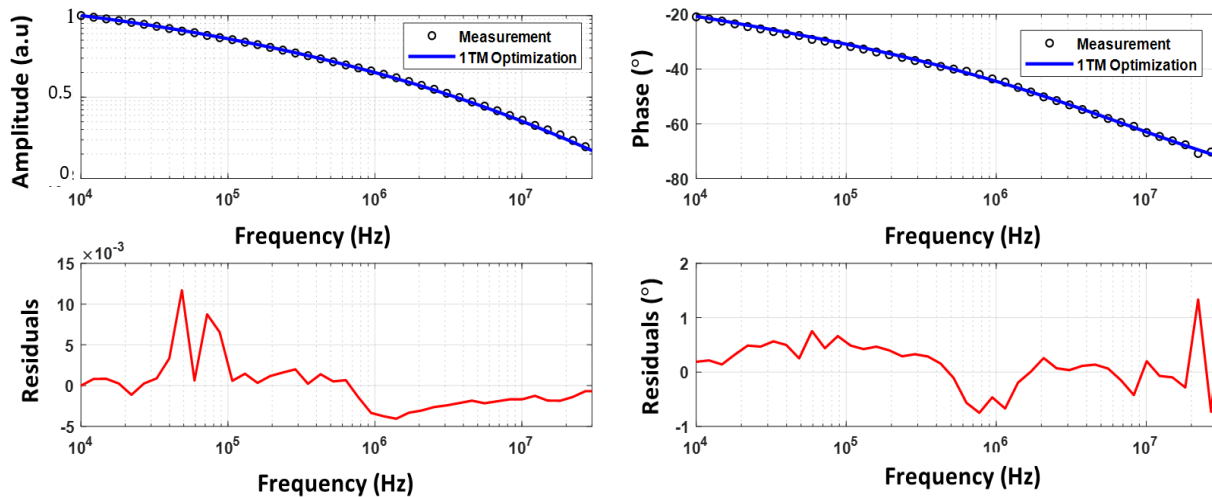


Figure 1-15: Measurement and optimization curves on the normalized amplitude and on the phase for the Al/SiO₂ sample and the residuals obtained in both cases.

The best optimization is obtained for a thermal conductivity of $k_{\text{SiO}_2}=1.21$ W/m/K and for an interface resistance of $R_{\text{Al/SiO}_2}=7$ nK.m² /W. The residuals show a small difference between the measurement and the thermal model. The identified value of the thermal conductivity and the

thermal resistance are in agreement with the theory and the previous published results for the SiO_2 layer [58-59].

Germanium Ge

The second studied sample is the Germanium substrate on which a 70 nm thick aluminum transducer has been deposited. As the previous sample, the two optimization parameters are the thermal conductivity k_{Ge} and the interface thermal resistance $R_{\text{Al/Ge}}$. The other thermal properties are fixed at the same values indicated before (see **Figure 1-14**) except the specific heat fixed at $C_{\text{Ge}}=1.65 \text{ MJ.m}^2/\text{K}$.

The optimization on the measurement curves are presented in **Figure 1-16**. The identified value for the thermal conductivity was $k_{\text{Ge}}=57 \text{ W/m/K}$ and for the interface thermal resistance was $R_{\text{Al/Ge}}=3.3 \text{ nK.m}^2/\text{W}$. The errors obtained during the optimization process are less than 5%. The identified values for both parameters are in agreement with the theory and the previous published results for the Ge layer [60].

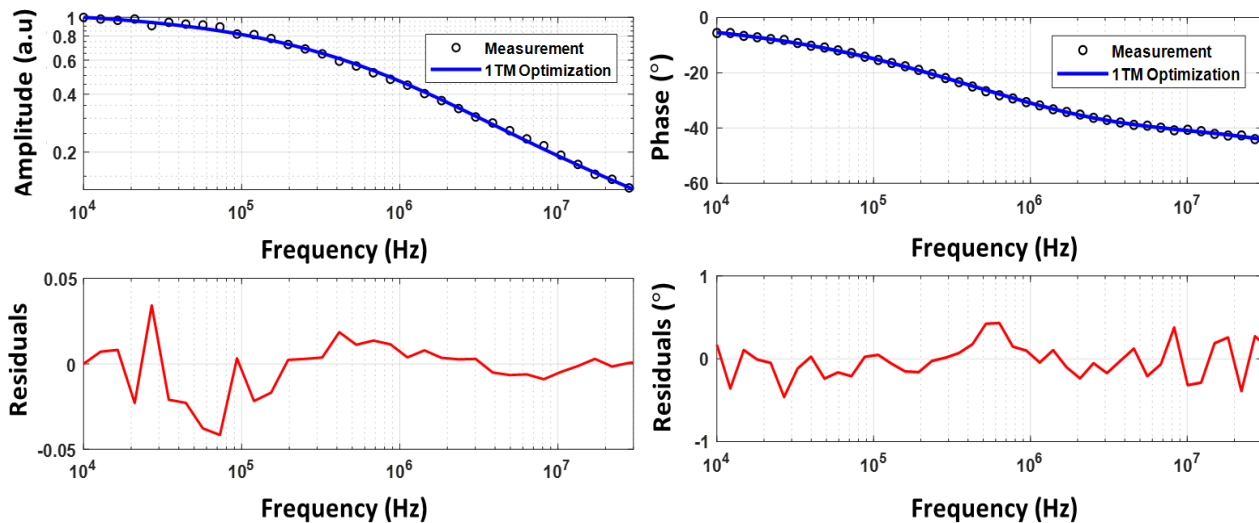


Figure 1-16: Measurement and optimization curves on the normalized amplitude and on the phase for the Al/Ge sample and the residuals obtained in both cases.

1.6.4 Uncertainty sources

During the optimization process, the residuals obtained show the difference between the experimental signals and the theoretical model data. This deviation, which determines the uncertainty of the identified values, is due to error sources that can affect the stability of the inverse problem. There are several sources that can have influence on the identified thermal properties.

First, one of these sources is due to the model error. The direct problem is used to predict the consequences of a phenomenon based on a model. If the model does not consider all of the parameters necessary to describe the phenomenon exactly, errors are likely to occur in the solution of the inverse problem. Second, the source of numerical error in the inverse problem where numerical errors can occur and result in an underdetermined inverse problem. Third, the errors source due to fixed parameters. In the inverse method, the fixed parameters in the model are assumed to be known. An error can therefore occur if one of the supposed known parameters is incorrectly estimated. And finally, the error source due to the measure of noise. The quality of the experimental data affects the solution of the inverse problem. The data may be noisy and lead to a lack of continuity which produces instability during the optimization process.

1.7 Conclusion

This chapter aimed to show the methodology of thermal characterization of materials using the techniques of pump-probe thermorefectance measurement and the Fourier model to identify the desired properties.

We have first detailed the basic principles and implementation of the thermorefectance method as well as its various configuration for measuring the thermal response of materials. In the time domain, we have presented the TDTR homodyne and the heterodyne techniques. The optical sampling with the femtosecond lasers used in these methods allows to measure a temporal response at time scales ranging from picosecond to nanosecond with sub-picosecond resolution. In the

frequency domain, we showed the FDTR method that has a lower cost and uses continuous lasers, where its response sampling depends on the frequency modulation of the pump laser.

For the modeling part, we have introduced the Two-Temperature Model that allows to describe the response of the metal after excitation by the femtosecond laser. This model will be used in chapter 2 to study the effect of the metallic transducer on the thermal response. We have also presented the One-Temperature Model based on the Fourier law in cylindrical coordinate for multilayer materials. The resulting heat equation is expressed in a matrix form and solved by applying a thermal quadrupoles method. The final equation obtained, representing the temperature response on the surface of the studied sample, is the basis of the model used to interpret the thermoreflectance response and to characterize the thermal properties.

Finally, we have shown an optimization method based on the function of the least mean squares for the thermal identification. The unknown properties are determined in such a way that they minimize the difference between the experimental measurement and the theoretical response calculated by the model. Experimental examples of thermal identification for SiO₂ and Ge layers have been presented on spectral responses obtained by the FDTR method. The identified values agree with the theory and the ones identified in the literature.

Chapter 2

Ultimate thermal resolution in TDTR: Influence of the transducer

Chapter 2 : Ultimate thermal resolution in TDTR: Influence of the transducer

2.1 Introduction

Among experimental techniques used to study the thermal properties and the transport of nanostructured materials, the pump probe femtosecond technique has proven to be the most efficient tool to access the dynamics of very fast phenomena, such as electron and phonon transport in nanomaterials [41, 61]. To study such high frequency phenomena, a large bandwidth is necessary. Yet, neither the pulse duration nor the detector time response is generally the bandwidth limiting factor. Indeed, in this pump-probe experiments, the transducer deposited on top of the material of interest, is usually the final limiting factor of the resolution and bandwidth through its thermal response to the excitation. This chapter will be devoted to study the thermal transport inside metal transducers used in Time-Domain Thermoreflectance experiments. This investigation will allow us to know the optimal film which provides the ultimate bandwidth of thermal resolution.

First, we will describe the criteria of the optimal transducer for the thermal spectroscopy in the TDTR heterodyne method. Then, we will implement and numerically solve the Two-Temperature Model to investigate the thermal transparency of several metal films. The study of heat carriers will be carried out inside thin and thick gold (Au) and aluminum (Al) transducers, which are commonly and currently used in femtosecond pump-probe experiments, in order to study the influence of both parameters (thickness, material) on the thermal response to the pump beam. Then, we will validate the model by measuring a TDTR heterodyne experimental signal for a gold film. Finally, the simulation will be extended to other metals for future possible experimental uses in order to determine the optimal transducer for the thermoreflectance study.

2.2 Ultra-fast transient thermal effects in the transducer

In thermoreflectance experiments, the transducer film plays a major role, especially for experiments with high temporal resolution, such as the heterodyne TDTR, that allow transient temperature measurements from hundreds of femtoseconds up to tens of nanoseconds. For such pump-probe methods, the corresponding spectral material response expands from 76 MHz up to 10 THz. However, the time resolution or the ultimate bandwidth of the technique are not limited by its optical sampling, but by the diffusion time of the heat flux in the transducer.

As we described before in chapter 1, during the first tens of femtoseconds after the pump beam interacts with the metal transducer, the absorbed energy induces a non-equilibrium thermal distribution of electrons before the thermalization through electron–electron collisions. Then, the system can be considered as a hot electron gas inside a cold phonon bath with an energy transfer through electron–phonon collisions, which can be described by the Two-Temperature Model. Finally, the thermal equilibrium between both electron and phonon baths is reached within a few picoseconds.

The thermal models used to adjust the experimental parameters and extract the desired thermal properties almost always consider the transducer layer as instantaneously thermalized, and then only as a heat reservoir which transfers its energy to the material of interest located below. In order to obtain reliable temperature measurements for thermo-physical parameter identification, two conditions must be checked: the thermal equilibrium must be reached, and the phonon relaxation within the layer of interest must have started. Since the transducer is a metal layer, its thermal conductivity is usually high but it must be as transparent as possible for the thermal transport in order to reach the thermal relaxation within the layer of interest as fast as possible. Apart from the thermal conductivity, other parameters, such as the electron–phonon coupling constant or the electronic capacity, are important factors and influence the thermal behavior of the metal transducer.

The actual bandwidth of the thermal response will then be determined by the thermal time of flight in the transducer. For that, one has to model the thermal transport in the transducer from the very early relaxation processes, when the electron gas is not yet thermalized with the phonon bath.

Thus, one key parameter to increase this bandwidth is the choice of the optimal transducer (material, thickness) delivering the best response to the pump laser pulse in order to reach the ultimate temporal resolution for thermal spectroscopy.

2.3 Thermal transport modeling of metal transducer: Solving non-linear 2TM by Finite element method

The transducer performances are obtained by calculating the transient electron and phonon temperatures. This relies on solving the non-linear equations of the semi-classical Two-Temperature Model. Within this framework, we have implemented an axisymmetric Finite Element Method (FEM) model to solve this thermal model. The system studied is a two-layer system of finite dimension, of which the first layer is that of the transducer, and the second one is a thermally thick substrate, which will be the layer of interest and it has been chosen to be Silica SiO_2 .

The simulation is established under femtosecond pump-probe experimental conditions. We focused our work on the transducer thickness. To do so, the model has to be fed with parameters such as laser temporal and spatial parameters and the optical penetration depth in the transducer. In this context, the material is assumed to be isotropic considering that the laser beams are Gaussian. The thermal response then presents a revolution symmetry around the axis of propagation. In the following, we will detail the thermal equations in each layer and the conditions used to solve the 2TM.

2.3.1 Transducer upon a layer of interest

As previously described, the transducer is needed to maximize the absorption of the laser pulse and convert it into heat transferred as fast as possible into the layer of interest. The transducer is described by the set of two equations for the electron and phonon temperatures presented by:

$$\begin{aligned}
 \rho C_e(T_e) \frac{\partial T_e}{\partial t} - \frac{1}{r} \frac{\partial}{\partial r} \left(k_e(T_e) r \frac{\partial T_e}{\partial r} \right) - k_e(T_e) \frac{\partial^2 T_e}{\partial y^2} &= -g (T_e - T_p) + q(r, y, t) \\
 \rho C_p \frac{\partial T_p}{\partial t} - \frac{1}{r} \frac{\partial}{\partial r} \left(k_p r \frac{\partial T_p}{\partial r} \right) - k_p \frac{\partial^2 T_p}{\partial y^2} &= g (T_e - T_p)
 \end{aligned} \tag{2.40}$$

The coefficients used in the equations of the 2TM are detailed in section 1.4 of chapter 1.

This temperature evolution, especially for electrons, cannot be applied in the silica substrate as it is a dielectric material and can then be assumed free of free electrons. As a consequence, the phonons lead the heat transfer that is fully described by the 1TM while taking into account the phonon bath [62]. The evolution of temperature in the substrate is then written as follow:

$$\rho C_s \frac{\partial T_s}{\partial t} - \frac{1}{r} \frac{\partial}{\partial r} \left(k_s r \frac{\partial T_s}{\partial r} \right) - k_s \frac{\partial^2 T_s}{\partial y^2} = 0 \tag{2.41}$$

where the terms ρC_s (J/m³/K), k_s (W/m/K) and T_s (K) are the specific heat capacity, the thermal conductivity and the temperature of the silica substrate, respectively.

The schematic modeling of the structure of the bilayer system, with the spatial coordinates and the conditions of the study, are shown in **Figure 2-1**. The boundary conditions are of Neumann type, where the normal components of fluxes are equal to zero all around the structure, especially on the y axis because of the axisymmetric aspect of the model. In addition, the SiO₂ substrate is thermally opaque due to its thermal diffusion characteristic time. This latter is, for a 250 nm thick SiO₂ and a diffusivity $D_{SiO_2}=0.87$ m²/s, given by:

$$\tau_{SiO_2} = \frac{250^2}{0.87} \approx 71ns \tag{2.42}$$

Indeed, the SiO₂ layer can be considered as a semi-infinite substrate at the time scales studied here (a few ns).

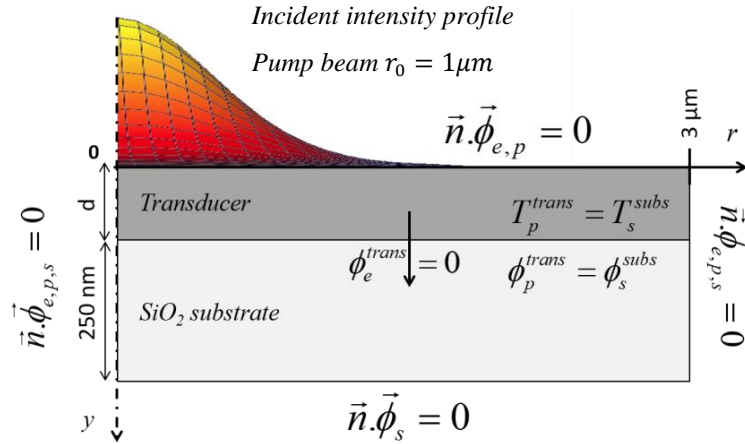


Figure 2-1: Cross section of the sample: $d=50$ or $d=150$ nm thick transducer upon silica layer (250nm). T and ϕ are the temperature and the heat flux respectively, \vec{n} is the outward unit normal vector, the superscript trans stands for the transducer while subs is for the substrate, the subscripts e, p, s denote the electrons, phonons and substrate respectively.

In the transducer, we will always consider the same amount of heat deposited by the pump laser so that it could be possible to compare the different materials. From a phonon point of view, we assume the continuity of the temperature and the flux at the interface between the transducer and the layer of interest. The electrons are considered confined in the metal layer leading to an adiabatic condition for them at all interfaces even between the transducer and the substrate [63]. This aspect implies an electron heat flux normal to this interface equal to zero.

One should notice that other pathways for the electrons to transfer their energy to the underlying layer can exist, such as a coupling between electrons and phonons in the dielectric layer by an harmonic interactions [64]. Moreover, a thermal resistance between the phonons coming from the metal and the dielectric layer can also exist. However, those pathways would be extremely dependent on the metal deposition process. Consequently, we have chosen not to consider these kinds of mechanisms that are furthermore screened by the low diffusivity of the dielectric layer.

2.3.2 Laser excitation

The power density coming from the absorbed laser pulse in the transducer, i.e. $q(r, y, t)$ in the equation, is modeled by a product of two Gaussian variables representing the spatial and the temporal extent of the pulse. This latter is not represented temporally by a Dirac function as in the One-Temperature Model, due to the short characteristic times in this approach, which considers the electrons excitation. The source term expression is then:

$$q(r, y, t) = E_{abs} \frac{\alpha e^{-\alpha y} e^{-\frac{r^2}{\sigma_r^2}} e^{-\frac{t^2}{\sigma_t^2}}}{\pi \sigma_r^2 \sigma_t \sqrt{\pi}} \quad 2.43$$

where σ_r (m) and σ_t (s) are constants equal to $\frac{r_0}{\sqrt{2}}$ and $\frac{\Delta t}{2\sqrt{\ln(2)}}$, respectively, E_{abs} (J) is the absorbed part of the incident laser energy, α^{-1} is the optical penetration depth, r_0 (m) represents the radius of the beam measured at $1/e^2$ of the maximum of intensity and Δt (s) is the duration of the laser pulse determined at full width at half maximum (FWHM).

2.4 Thermal investigation of aluminum and gold transducers

In this section, we focus on the most used metal films in pump-probe thermoreflectance, namely, Al and Au transducers. We will compare their thermal behavior during and just after coincidence, meaning during the first tens of ps, to concentrate on the electron-phonon interactions. Then, we will look at longer time scales and analyze the phonon relaxation in both materials. At the end of this section we will validate this study by an experimental measurement for a metallic Au film.

2.4.1 Electron and phonon dynamics through the films

The 2TM is applied to describe the heat transfer and the temperature dynamics in metals. In this part, we investigate the thermal relaxation predicted by this model in Al and Au films. The simulation is performed with two different thicknesses, 50 nm and 150 nm, for each film, in order to also study the effect of thicknesses on thermal transport. The thinnest value 50 nm is a good trade-off in order to avoid the optical interferences with the underlying material, which would change both thermal and optical responses of the transducer [65-66]. Our interest in the Al and Au transducer metals is due to their important characteristics and desirable properties for TDTR, such as high thermal conductivity, significant thermoreflectance coefficient and others [67].

2TM simulation parameters		
	Pump radius (intensity $1/e^2$)	$r_{0p}=1 \mu m$
	Probe radius (intensity $1/e^2$)	$r_{0s}=1 \mu m$
Transducer Al	Thickness	d=50, 150 nm
	Thermal conductivity	$k_e=232, k_p=5$ W/m/K
	Coupling constant	$g=25 \times 10^{16}$ W/m ³ /K
	Electronic capacity	$\gamma_e=133$ J/m ³ /K ²
	Specific heat capacity	$\rho C_{Al}=2.45$ MJ/m ³ /K
Substrate SiO ₂	Thickness	250 nm
	Thermal conductivity	$k_{SiO_2}=1.44$ W/m/K
	Specific heat capacity	$\rho C_{SiO_2}=1.65$ MJ/m ³ /K

Table 2-1: Parameters of Al/SiO₂ sample used for Two-Temperature Model calculations.

The Al film deposited on the silica layer is heated with an 800 nm pump beam that deposits 18 pJ of energy absorbed within the 7 nm optical penetration depth in the film. The thermal properties

of the sample Al/SiO₂ involved in this modeling are listed in **Table 2-1**. These values used were taken from the literature [58, 64].

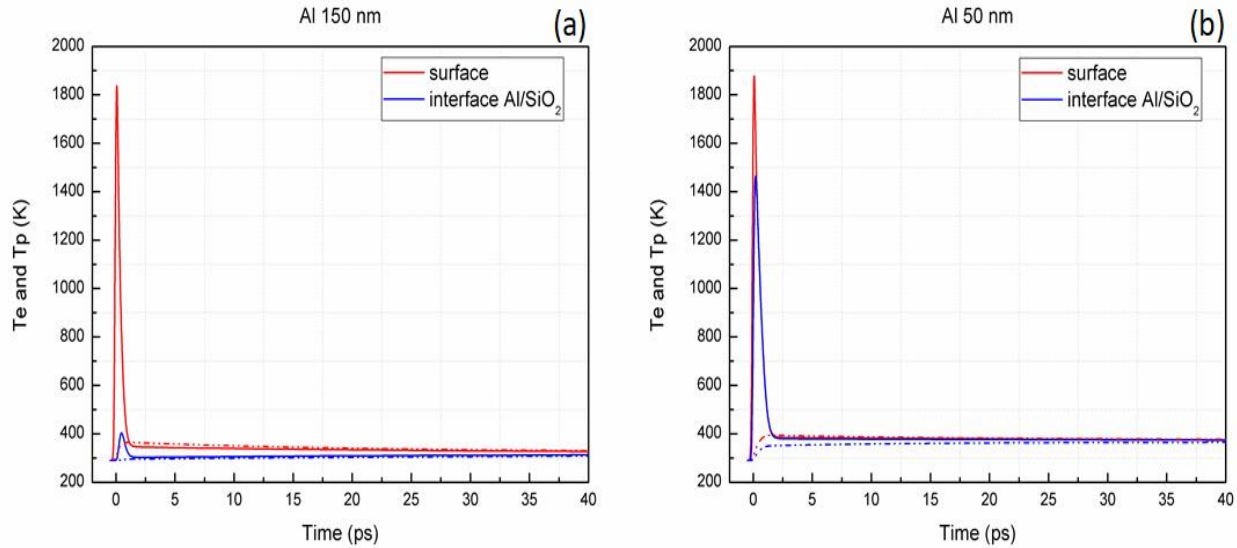


Figure 2-2: Electron T_e (solid lines) and phonon T_p (dashed lines) temperature at the surface (in red) and at the Al/SiO₂ interface (in blue) of a (a) 150 nm and (b) 50 nm thick Al film.

The electron and phonon temperatures in Al films predicted by the model are displayed in **Figure 2-2** for two different thicknesses, a 150 nm thick film (**Figure 2-2(a)**) and a 50 nm thick film (**Figure 2-2(b)**). In both cases, the temperature evolution at the surface and at the interface of Al/SiO₂ is plotted. The temporal response shows an increase of electronic temperature and then a rapid relaxation. This relaxation represents the fast transfer of energy from the electron gas to the phonon bath. As a consequence of the high electron–phonon coupling constant value in Al ($g=25 \times 10^{16}$ W/m³/K), the temperature reaches electron phonon thermal equilibrium within 2 ps. In comparison, there is no significant heat transport at the interface Al/SiO₂ for the 150 nm thick transducer where the temperature barely changes. However, for the 50 nm thick Al film, the electronic temperature at the interface increases, indicating a significant heat transport to the dielectric layer.

A similar calculation was performed for Au film deposited on SiO₂ substrate using thermal properties taken from the literature [38, 68] and reported in **Table 2-2**. Thus, we adjusted the

amplitude of the source term in order to obtain 18 pJ energy as in the Al film. This energy is absorbed in the optical penetration depth of Au, which is 12 nm at 800 nm laser wavelength.

		2TM simulation parameters	
		Pump radius (intensity $1/e^2$)	$r_{0p}=1 \mu m$
		Probe radius (intensity $1/e^2$)	$r_{0s}=1 \mu m$
Transducer Au	Thickness	d=50, 150 nm	
	Thermal conductivity	$k_e=318, k_p=3$ W/m/K	
	Coupling constant	$g=2.2 \times 10^{16}$ W/m ³ /K	
	Electronic capacity	$\gamma_e=67.7$ J/m ³ /K ²	
	Specific heat capacity	$\rho C_{Au}=2.49$ MJ/m ³ /K	
Substrate SiO ₂	Thickness	250 nm	
	Thermal conductivity	$k_{SiO_2}=1.44$ W/m/K	
	Specific heat capacity	$\rho C_{SiO_2}=1.62$ MJ/m ³ /K	

Table 2-2 Parameters of Au/SiO₂ sample used for Two-Temperature Model calculations.

The dynamics of the electron and phonon temperatures in Au film at the surface and at the interface Au/SiO₂ are plotted in **Figure 2-3(a)** and **Figure 2-3(b)** for a 150 nm and 50 nm thick transducers, respectively. The gold electrons exhibit a higher temperature rise than in aluminum for the same energy absorbed. This is explained by the lower electron thermal capacity in gold, about half the value of the aluminum one ($\gamma_e(\text{Au}) \cong \gamma_e(\text{Al})/2$). As for aluminum, the electrons relax into the phonon bath within the first 9 ps. This transfer is slower than in aluminum because of the weak electron phonon coupling constant in gold ($g=2.2 \times 10^{16}$ W/m³/K), that is 12 times smaller. In addition, gold has a higher electron thermal conductivity, allowing a fast electron heat flux in the Au film. This rapid propagation is observed by the difference between the temperature at the

surface and at the interface Au/SiO₂, which is far smaller than in the Al transducer, as well for the electrons as for the phonons.

Therefore, because of the weak electron phonon coupling, the temperature in Au films is rapidly homogenized, especially for thin films where electrons propagate through the entire film thickness before any interaction with the phonons. On the contrary, in Al films where the electron-phonon coupling constant is stronger, electrons rapidly relax their energy into the phonon bath and the phonons then start diffusing in the thickness of the metal film.

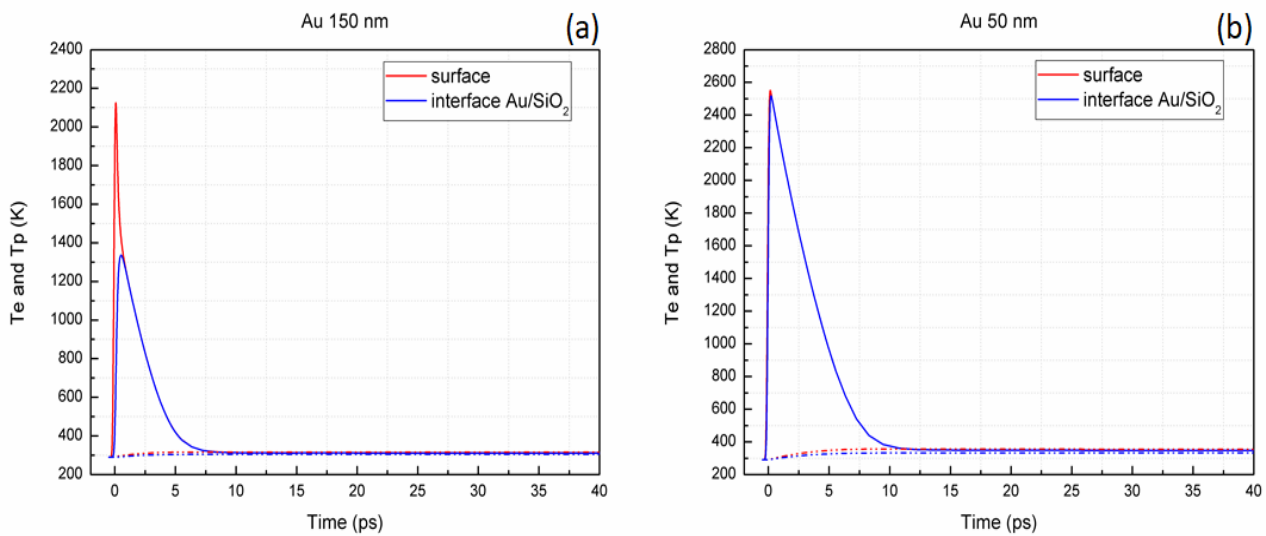


Figure 2-3: Electron T_e (solid lines) and phonon T_p (dashed lines) temperature at the surface (in red) and at the Au/SiO₂ interface (in blue) of a (a) 150 nm and (b) 50 nm thick Au film.

2.4.2 Phononic dynamics at the film–substrate interface

The nature of the transducer material plays a major role in the transport of the thermal energy to the underlying layer of interest. This transfer, specifically of the phonon energy, depends on the thermal properties of the transducer, leading to a thermal equilibrium and a different heat transport at the interface between the transducer and the layer. This phonon heat transport can be obtained when the phonon temperature starts decreasing after the thermal equilibrium is reached. To a better understanding of the behavior and the dynamics of the phonon energy in Au and Al films, **Figure**

2-4 shows the temperature of the phonons at the interface of Au/SiO₂ and Al/SiO₂, for both 150 nm and 50 nm thicknesses, calculated by the Two-Temperature Model on a longer time scale.

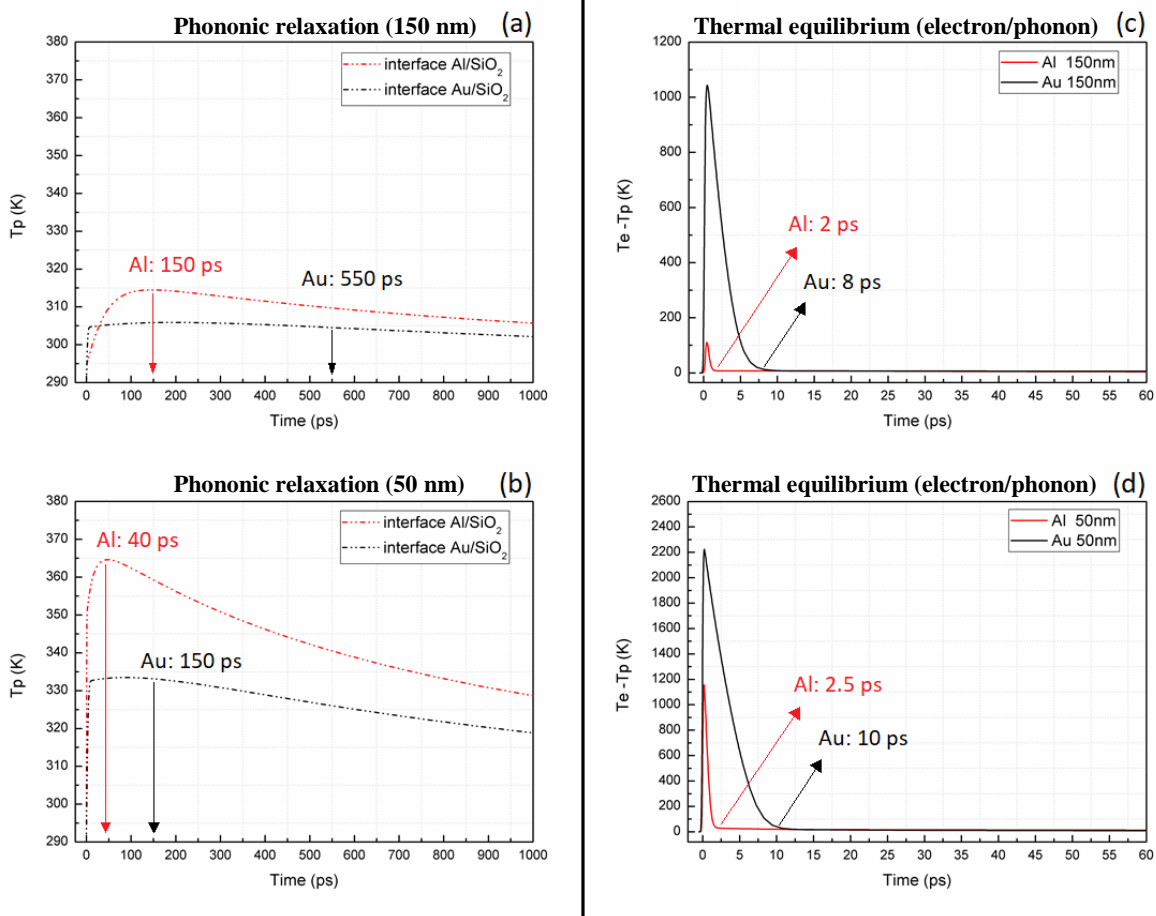


Figure 2-4: (a,b) Phonon temperature relaxation and (c,d) electron and phonon temperature differences at the interface of Au/SiO₂ (in black) and Al/SiO₂ (in red) films respectively for a (a,c) 150 nm and a (b,d) 50 nm thickness.

Figure 2-4(a) and **Figure 2-4(b)** show the influence of the electron–phonon coupling constant on the phononic temperature at the interface. The higher electron–phonon coupling in Al film allows the phonons to reach the thermal equilibrium with the electrons faster than in Au film, which is characterized by a low coupling constant. The subtraction of the electron and the phonon temperatures at the interface tends to zero indicating that thermal equilibrium is reached in aluminum and gold respectively around 2 ps and 10 ps as shown in **Figure 2-4(c)** and **Figure**

2-4(d). Furthermore, the amplitude of the phonon temperature at the interface of Al/SiO₂ rises to a higher value than the one at the Au/SiO₂ interface.

Moreover, when the Al phonons reach their thermal equilibrium, the temperature starts to relax and thermalize 40 ps after the excitation in thin films (50 nm). This relaxation starting time is 4 times shorter than for Au (150 ps). This fast relaxation of the phonon temperature in Al, even for thick films (150 nm), means a faster thermal transfer and a higher transparency of the Al film. Thus, the model shows that the large amount of the absorbed energy at the Al surface is transferred from the electrons to the phonons and thus is flowing inside the layer of interest. The thermal time of flight in the metal transducer is the actual limiting factor for TDTR thermal temporal resolution. On the contrary, the low electron phonon coupling in the gold film leads to a weak and slow phonon heat transport toward the interface and thus to a low sensitivity to the bottom layer thermal properties.

In the remaining of this chapter, the study continues for 50 nm thick films, which showed faster thermalization and heat transfer to the material of interest deposited below.

2.4.3 Spectral response study

After having simulated the temporal dynamics of the temperatures in Au and Al as well as indicating the heat transport provided by these two transducers, we will now study their thermal response in the frequency domain. In this case, to obtain the frequency response of these materials both Au/SiO₂ and Al/SiO₂ samples, the Fourier Transform of the impulse response was calculated.

The result is shown in **Figure 2-5** where the full lines in blue and orange are the spectra of the electron temperature shown previously in **Figure 2-2(b)** and **Figure 2-3(b)** at the top surface of the 50 nm thick transducer. It clearly appears that these spectra with a frequency band extending from 10 kHz to 10 THz, can be divided into four different regions (A, B, C, D) with a very different frequency behavior.

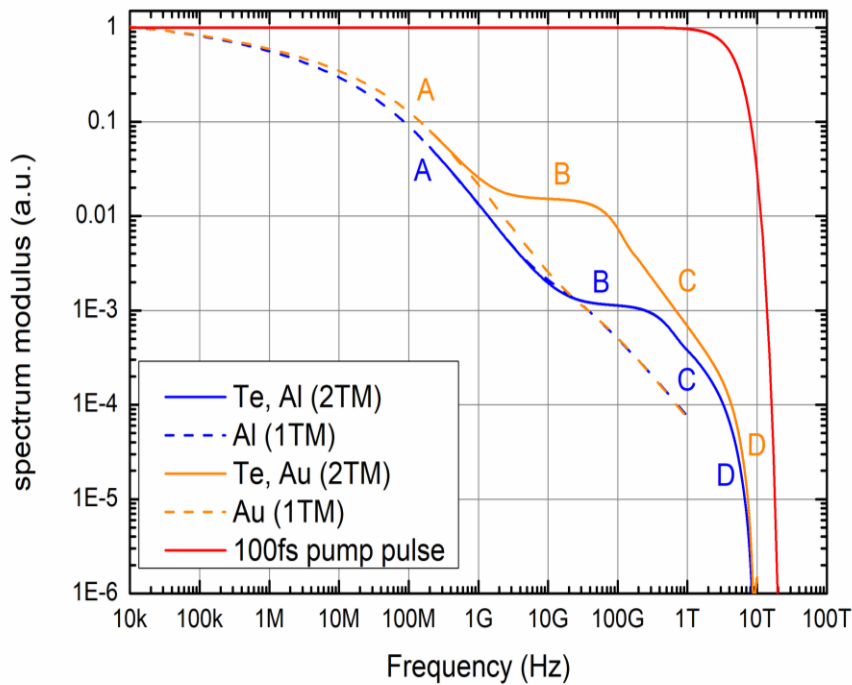


Figure 2-5: Comparison of the frequency response magnitudes normalized at 10 kHz of gold and aluminum with a thickness of 50 nm each. Dashed lines represent the 1TM response, full lines Blue and orange are the 2TM spectra and the red stands for the spectrum for the laser pump pulse of 100 fs at full width at half maximum (FWHM).

Region A is the frequency range where the heat is uniform at the depth of the transducer and transferred to the SiO_2 . The temperature relaxation in this range no longer depends on the transducer and can be modelled by the classical One-Temperature Model detailed in chapter 1. The 1TM response overlaps with the 2TM at low frequencies up to 1 GHz for gold and up to 10 GHz for aluminum. These two frequencies are related to the phonon thermal relaxation starting times at the interface between the transducer and the substrate for Al/ SiO_2 and Au/ SiO_2 , which are extracted from **Figure 2-4(b)**. Region B is the frequency regime where the heat is transferred in the transducer by the diffusion of electrons and phonons. The frequency limit of this region is governed by the electron-phonon coupling constant and the specific heat capacity. Region C is the adiabatic heating of the electron gas before any diffusion or thermalization process with the phonons occur. At last, region D is the ultimate frequency of the spectrum coming from the spectral extension of the laser pulse, represented by the full red line (**Figure 2-5**).

From a characterization point of view concerning the measurement of thermal properties of the underlying layer, the properties sensitivity to the layer of interest appears in region A where the phonon and electron are thermalized. The actual thermal bandwidth of the measurement is the region A width. It appears that the aluminum transducer provides the widest frequency bandwidth, about 10 GHz, in comparison to gold with a bandwidth of 1 GHz.

From a hot carrier analysis point of view, the non-equilibrium processes occur in regions B and C. The wider these regions, the better the hot carrier behavior is determined. The lower frequency is limited by the electron–phonon coupling constant while the upper limit is the extension of the spectrum of the laser pulse. In that case, gold is the best material for hot carrier study with a bandwidth extending from 1 GHz up to 5 THz.

2.5 Experimental validation of the modeling

In order to validate the thermal study carried out by the Two-Temperature Model, we will show in this part a thermoreflectance experimental measurement for a gold film. We will first describe the TDTR asynchronous setup employed in the laboratory. In a second step, we will develop a measurement realized with this device and compare it to the theoretical response.

2.5.1 Asynchronous TDTR setup

The asynchronous TDTR experimental bench used for the measurement in this part is presented in **Figure 2-6**. The laser cavities are two oscillators Ti:Sa pumped by a continuous Nd: YVO4 laser at 532 nm providing 18 W. The oscillators have a repetition frequency around $F_p=76.2$ MHz and generate pulses with a duration of ~ 100 fs. The difference in repetition rate between the two laser cavities is $\Delta F = 523$ Hz, thus giving a single acquisition in two milliseconds. The wavelengths of the laser beams are 808 nm for the pump and 786 nm for the probe. An optical parametric oscillator (OPO) is employed to change the wavelength of the probe according to the metallic transducer deposited on the studied sample.

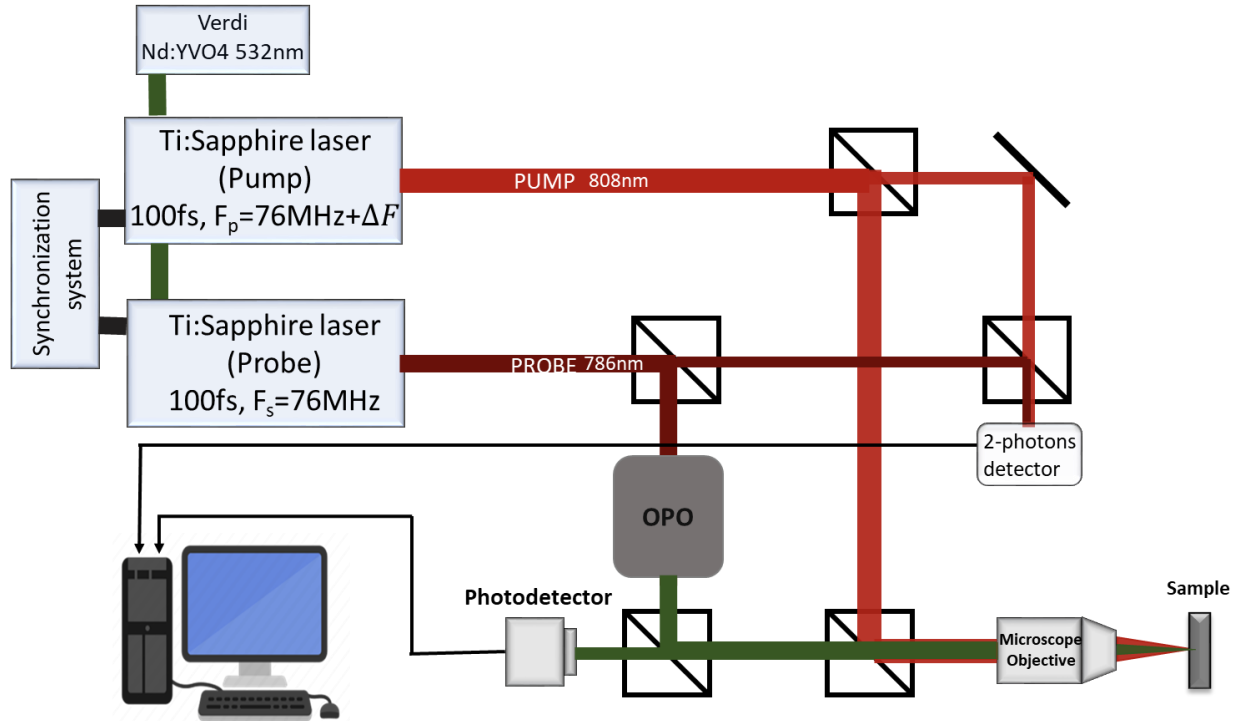


Figure 2-6: Sketch of the TDTR asynchronous set-up. An optical parametric oscillator is inserted to probe with 530nm wavelength.

The pump and probe beams are recombined and focused on the tested sample by a planar microscope objective having a magnification of 50X. The beam sizes were measured using a beam profiler. The pump and probe lasers have a respective radius of $4.5 \mu\text{m}$ and $3 \mu\text{m}$ on the sample surface. The signal reflected by the sample is detected by a silicon photodiode having a bandwidth of the order of several GHz, a bandwidth much higher than the frequency of the signals of interest.

Under these optimal conditions, this setup allows measuring the thermal response of nanostructured materials from ~ 100 fs (the pulse duration) up to 13,2 ns (the repetition rate of the pump laser). From a frequency point of view, the spectrum extends up to few THz with a spectral resolution equal to the repetition rate of the pump laser of 76 MHz. It should be noted that because of lenses of the different optical elements crossed by the laser this may lead to increase the pulse duration and thus to decrease the spectral bandwidth.

2.5.2 Spectrum of Au transducer film

To validate the modeling, we have tested a sample whose structure consisted of a 50 nm thick gold transducer deposited on a silica substrate. The probe wavelength is fixed at 532 nm due to the high thermoreflectance response of gold at this wavelength [38, 68]. In this case, the duration of the probe pulse increases to around ~ 1 ps due to the optical elements. The experimental spectral response of the Au/SiO₂ sample as well as the response simulated by the Two-Temperature Model are shown in **Figure 2-7**. The experimental spectrum is obtained by applying a Fourier transform of the TDTR temporal signal (inset of **Figure 2-7**). This temporal signal is negative because the thermoreflectance coefficient of Au at this wavelength is negative.

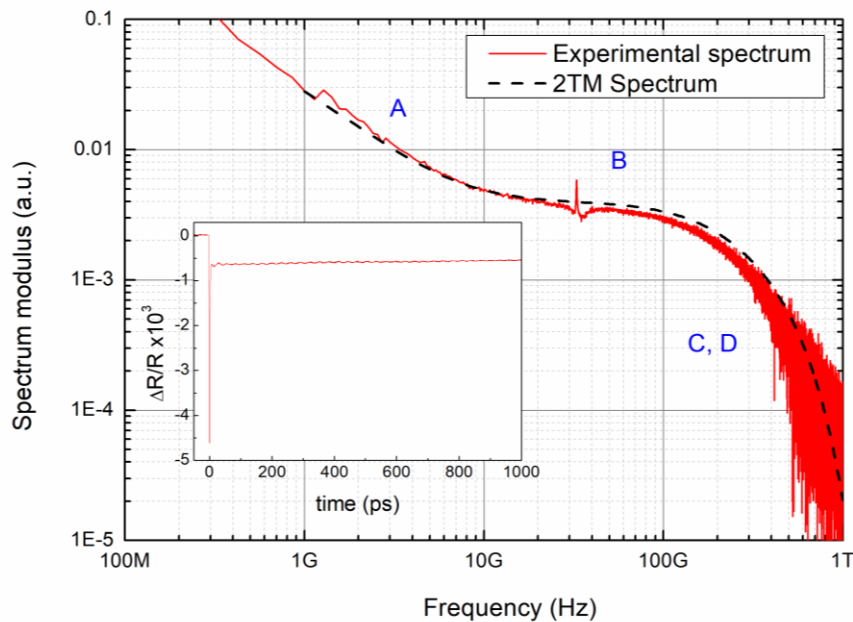


Figure 2-7: TDTR experimental and simulated (2TM) spectral responses for an Au film on silica layer. The temporal signal corresponding to the experimental spectra is presented in inset.

The comparison between the experimental and the theoretical spectra shows that the two curves are matching perfectly. The different regions of the spectral response, detailed in the previous section, are clearly visible even if regions C and D are superimposed due to the 1 ps experimental

pulse duration limiting the thermal bandwidth to 1 THz. In addition, the acoustic resonance frequency of the 50 nm Au film appears clearly at 32.8 GHz for a 3.24 nm/ps speed of sound in Au.

2.6 Thermal behavior of other metal films

We now investigate the thermal behavior of other possible metallic films to identify the most suited transducer for TDTR measurements, in particular, in terms of thermal temporal resolution. We hence investigate the phonon transport for four other metals: chrome (Cr), platinum (Pt), copper (Cu), and silver (Ag). Their thermal properties taken from the literature [62, 65, 69–71] are presented and compared to those of Au and Al in **Table 2-3**.

Metal	g ($10^{16}\text{W/m}^3/\text{K}$)	γ_e ($\text{J/m}^3/\text{K}^2$)	ρC_p ($10^6\text{J/m}^3/\text{K}$)	k_e (W/m/K)	k_p (W/m/K)
Au	2.2	67.7	2.49	318	3
Al	25	133	2.4	232	5
Cr	42	193	3.2	130	20
Pt	109	746	2.8	65	7
Cu	10	98	3.3	401	3.3
Ag	3.1	63.3	2.5	420	3.5

Table 2-3: Thermal properties of metals used for 2TM calculations.

The results calculated by the 2TM are displayed in **Figure 2-8**, presenting the phonon temperature obtained at the interface metal/SiO₂, with 50 nm thick transducers. According to the characteristics of the electronic structure of the metals, the graphs are regrouped for noble metals (Au, Ag, and Cu) and for non-noble metals (Al, Pt, and Cr). It should be noted that these curves were calculated

for the very same conditions for all metals, thus the laser incident energy changes with the optical properties of each one to achieve the same energy deposited in the transducer layer.

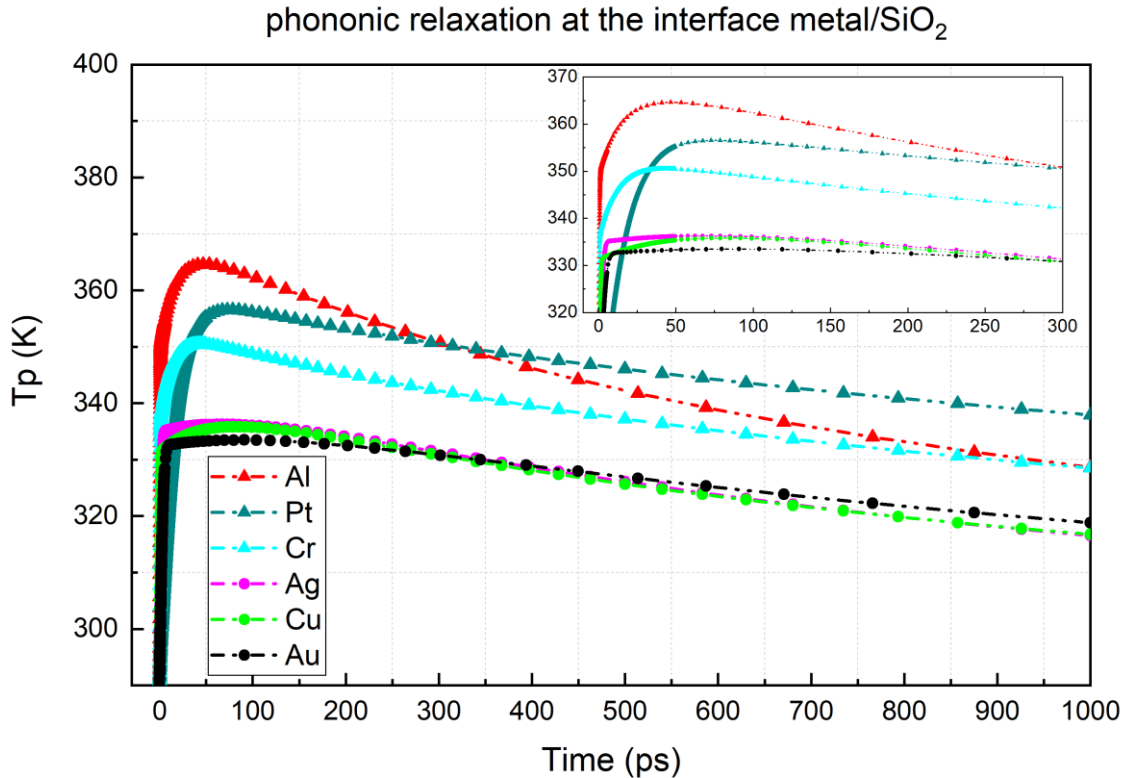


Figure 2-8: Transient phonon temperature predicted by 2TM at the surface film/SiO₂, for films Au, Pt, Cr, Ag, Cu and Au of 50 nm thickness. Zooming figure of the first 300 ps of the responses is represented in inset.

The temperature of phonon predicted at the interface for each one of the noble metals (Au, Ag, and Cu) are very similar (see **Figure 2-8**). This similarity of performance in heat transport results from the comparability of the thermal properties of these metals. Because of the high electronic conductivity and the low electron-phonon coupling constant, the hot electrons propagate directly to the interface with a low thermal relaxation toward the lattice, which means a weak phonon transfer at the metal/SiO₂ interface. However, the phonon transfer increases and reaches an important temperature at the interface in the non-noble metals (Al, Pt, and Cr). Here, the important electron-phonon coupling in these metals induces a large thermal relaxation to the lattice. Although Pt and Cr films have a very strong electron-phonon coupling, the highest phonon

temperature reaching the interface metal/SiO₂ is obtained with the Al interface. This is due to the lower thermal capacity in Al compared to that of Cr and Pt (see **Table 2-3**).

From the inset of **Figure 2-8**, representing the metal/SiO₂ interface phonon temperature during the first 300 ps for the 6 considered materials, we can estimate the phonon relaxation starting time as it was previously done for Al and Au. The Al and Cr films own an important feature: the interface phonon temperature relaxes in a shorter time (40 ps) compared to other metals, all represented in **Table 2-4**.

Metal	Au	Ag	Cu	Al	Cr	Pt
trp (ps)	150	80	90	40	40	80

Table 2-4: The phononic relaxation starting time obtained by TTM for the studied metals.

This rapid relaxation at the metal/SiO₂ interface leads to a fast phonon transport toward the layer of interest. Therefore, the thermal behavior of Al film, characterized by the fastest thermal transfer with high amplitude, makes it a preferable transducer in TDTR experiments for spectroscopic lattice temperature measurements.

2.7 Conclusion

In TDTR experiments, the metal transducer thermal transparency appears to be the most limiting factor of the temporal resolution. As the accessible temporal range expands over five decades from 100 fs up to 10 ns, the fundamental assumption of local thermal equilibrium between electrons and phonons is no longer valid over the entire response. In this chapter, a Two-Temperature Model has been implemented to describe the dynamics of both phonon and electron temperatures through the metal films.

We have simulated the heat transfer after a 100 fs laser strike in a metal transducer deposited upon a silica layer, this latter standing for the material of interest in common TDTR thermo-physical parameter metrology experiments. We have studied the role of the transducer thickness (50 nm and 150 nm) on one hand; and on the other, the role of the material nature with a set of six different materials: three metals, chrome (Cr), platinum (Pt), and aluminum (Al); and three noble metals, gold (Au), copper (Cu), and silver (Ag).

We showed that the TDTR frequency response is governed by the electrons in the high frequency range [10 GHz – 5 THz] and phonons in the low frequency range [100 MHz – 10 GHz]. From a hot carrier point of view, noble metals, especially gold, are well suited for carrier dynamics studies. In that case, the temporal resolution limiting factor is the spectral extension of the laser pulse. Besides, from a metrological point of view, non-noble metals have the best phonon transparency allowing thermo-physical property measurements in a wide frequency range. Among them, 50 nm aluminum transducers reveal to be the best candidates exhibiting a frequency bandwidth up to 10 GHz. Finally, the optical sampling performances limit the spectral bandwidth to 1 THz for electronic studies, while the phonon time of flight in the transducer limits the spectrum in thermal metrology to 10 GHz.

The following work of this thesis is devoted to study and characterize the heat transfer in many types of materials. Therefore, the aluminum transducer will be the better suited for this study.

Chapter 3

Ultra-broadband spectroscopy of heat transport

Chapter 3 : Ultra-broadband spectroscopy of heat transport

3.1 Introduction

In this chapter we will investigate and characterize thermal properties of different types of materials through an ultra-broadband spectroscopy. For this, we will use a spectral thermal sensor that combines the measurements of FDTR and TDTR methods. The power and efficiency of this measurement approach is based on several points: the ability to characterize a wide range of materials thermal conductivity; having a wide frequency range for the sensor response, being a correlation suppression of the sensitivity of thermal properties, which allows these latter to be identify simultaneously; and the ability to measure the superdiffusive regime existing in an unspecified frequency range in alloys (detailed later in chapter 4).

In the beginning of this chapter, we will study in frequency domain the theoretical thermal response of different types of materials from the One-Temperature Model. Then, we will show a sensitivity analysis of the materials response to the thermal properties. This analysis will allow a better understanding of the correlations between parameters and their impact over the studied frequency range.

In a second time, we will present the FDTR/TDTR spectral sensor used in this work for thermal measurements of materials. We will see the capacity of this sensor to probe the different thermal behaviors with a wide spectral bandwidth.

Later, we will present the results of thermal measurements obtained using the spectral sensor on many materials. These studied samples will be characterized by a different heat transfer with a wide range of thermal conductivity to illustrate performance of the sensor. Finally, an uncertainty analysis will be performed on the error sources of the thermal identification by the inverse method.

3.2 Scenario of thermal parameter identification in frequency domain

In the One-Temperature Model, detailed in chapter 1, we have seen that the heat diffusion equation was solved by analytical approach, which is the quadrupole method. The model describes the thermal transport of a multilayer system heated periodically with radial symmetry at the top surface. The final expression of the surface temperature was obtained in Laplace-Hankel space, as presented previously by equation 1.37, which becomes:

$$\theta_{tr,in}(\alpha, z = 0, p) = G(\alpha, p)\Phi_{tr,in}(\alpha, z = 0, p) \quad 3.44$$

with,

$$G(\alpha, p) = \left(\frac{N_{11} + k_{sub}q_{sub}N_{12}}{N_{21} + k_{sub}q_{sub}N_{12}} \right)$$

where α (m^{-1}) is Hankel variable, p (s^{-1}) is Laplace variable, $G(\alpha, p)$ is the medium response, $\theta_{tr,in}$ is the surface temperature and $\Phi_{tr,in}$ is the laser flux in Laplace-Hankel space.

In order to analysis the heat response, we are considering here the simple case of a transducer deposited on a semi-infinite substrate. By taking the inverse Hankel transform, we get the frequency response of the temperature in real space, with G being a matrix of the thermal properties of the studied system:

$$T(r, z = 0, p) = \frac{1}{2\pi} \int_0^{\infty} G(\alpha, p) Q \left(\frac{r_p^2}{2} \right) e^{\frac{r_p^2}{4}\alpha^2} J_0(\alpha r) \alpha d\alpha \quad 3.45$$

where J_0 is a zero-order Bessel function.

The surface temperature is measured by the reflected intensity of the probe laser. We must then weight the equation by the probe intensity distribution, which is taken as a Gaussian spot, although the radius may be different than the pump beam:

$$T(r, z = 0, p) = \frac{A_0}{2\pi} \int_0^\infty G(\alpha, p) e^{\left(\frac{r_p^2 + r_s^2}{4}\right)\alpha^2} J_0(\alpha r) \alpha d\alpha \quad 3.46$$

where the constant A_0 (W) is equal to $Q \left(\frac{r_p^2}{2}\right)$, and r_s (m) is the $1/e^2$ radius of the probe beam spot on the surface.

Thus, the frequency domain response can be qualitatively understood by examining the temperature expression solution at the low and high frequency limits. At the low frequency limit ($p \rightarrow 0$), the temperature expression is:

$$T(r, z = 0, p) \xrightarrow{p \rightarrow 0} \frac{A_0}{k_{sub} \sqrt{2\pi(r_p^2 + r_s^2)}} \quad 3.47$$

In this case, the amplitude of the temperature response is inversely proportional to the thermal conductivity of the medium, and the phase is synchronous with the incident heat flux. This equation is equivalent to the solution for three-dimensional (3D) heat distribution where the local steady state temperature rise of the sample can be estimated [72].

On the other hand, at the high frequency limit ($p \rightarrow \infty$), equation 3.46 becomes:

$$T(r, z = 0, p) \xrightarrow{p \rightarrow \infty} \frac{A_0}{\pi r_p^2 \sqrt{ik_{sub} \rho C_{sub} \omega}} \quad 3.48$$

where ω is the angular frequency. In this second case, the amplitude temperature response is this time inversely proportional to $\sqrt{k_{sub} \rho C_{sub}}$, which is the substrate thermal effusivity ($\text{W/m}^2/\text{K}\cdot\text{s}^{1/2}$). Moreover, the phase of the surface temperature lags relative to the heat flux by $\frac{\pi}{4}$. This

temperature equation (3.48) at high frequencies thus corresponds to the solution for one-dimensional heat flow (1D) [72].

Actually, the sensitivity of the temperature surface depends on the characteristic penetration length scale of the thermal wave, which decays exponentially into the solid. This penetration scale, known as the thermal diffusion length L_h (m), is defined as:

$$L_h = \sqrt{\frac{2D}{\omega}} = \sqrt{\frac{2K}{\omega\rho C}} \quad 3.49$$

where D (m²/s) is the thermal diffusivity of the studied medium. The associated thermal length scale, compared to the spot size of the pump laser, determines whether the temperature surface approaches more the one-dimensional or the 3D thermal transport. If thermal diffusion length is bigger than the pump size ($L_h \gg r_p$), the isotherm within the sample tends to be spherical and the temperature response approaches more the 3D distribution. Alternatively, if thermal diffusion length is smaller than the pump size ($L_h \ll r_p$), the isotherm becomes relatively planar and therefore the temperature surface can be approximated with the 1D distribution.

3.3 Direct problem and sensitivity study of 1TM

Identifying the thermal properties of different materials requires a study of their theoretical spectral response based on the thermal model. The resolution of this direct problem makes enable the evaluation of the sensitivities of the model and the influence of the thermal properties. This study is critical to determine the variation and the existing correlations between parameters. This allows us to know the identifiable properties, those that must be fixed as well as the adequate measurement method. For that, we will study in this section by the One-Temperature Model, the spectral response of several types of materials characterized by different thermal conductivities, and then a sensitivity analysis will be performed. In this case, the sensitivity of both the phase and the

amplitude of the spectral response, are defined by the upcoming functions. The phase variation function Δ_{ph} at a given parameter Y is:

$$\Delta_{ph} (^\circ) = Ph(f, Y + \Delta Y) - Ph(f, Y) \quad 3.50$$

and, the relative amplitude variation function $\Delta_{Amp\text{relative}}$ at a given parameter Y is:

$$\Delta_{Amp\text{relative}} = \frac{A(f, Y + \Delta Y) - A(f, Y)}{A(f, Y)} \quad 3.51$$

where A and Ph are the amplitude and the phase spectral response calculated from the thermal model, respectively, f (Hz) is the frequency of the pump laser and Y represents the studied parameter. In the following, this parameter is varied constantly for all the studied samples by attributing 10% variation to the parameter.

3.3.1 Case study: transducer on substrate to evaluate the range of measurement

For this thermal investigation, we considered the simple case of an Al transducer layer of a few tens of nanometers, deposited on a semi-infinite substrate which is the layer of interest. Among the thermal properties used for the calculation, one is the optical penetration depth in aluminum with a value equal to 7 nm at the 800 nm excitation wavelength. The discontinuity of the temperature field at the interface between the two layers is modelled by an interface resistance. In addition, to study the thermal response of several types of materials and the sensitivity of their thermal properties, the substrate will have different thermal conductivities. The values chosen are 10^2 W/m/K (metal), 10^1 W/m/K (alloy), 10^0 W/m/K (glass) and 10^{-1} W/m/K (polymer). **Figure 3-1** presents a schematic description of the sample, with all the required properties for its modeling.

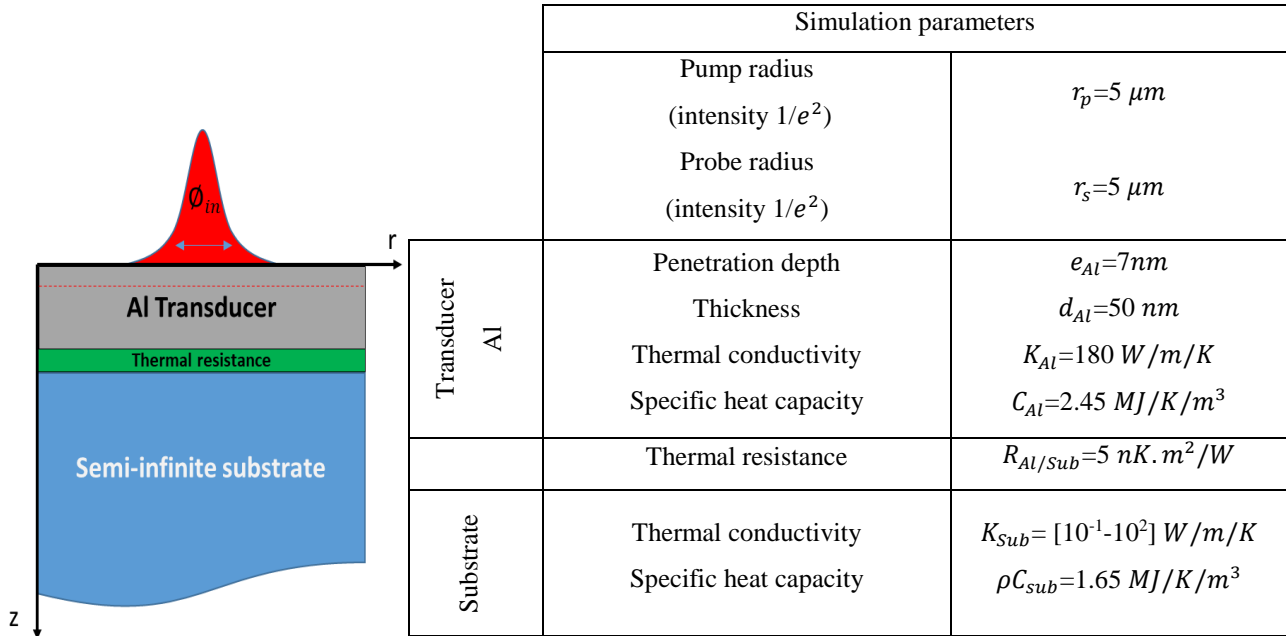


Figure 3-1: Modeling of an Al transducer deposited on a semi-infinite substrate.

3.3.2 Modeling over 3 decades of thermal conductivities

The frequency band of the 1TM simulation extends from 10 kHz to 1 THz. This band takes into consideration the spectral response of the two methods of the thermoreflectance measurement, FDTR and TDTR Heterodyne. As we have seen before, the FDTR experiment typically measure the spectral response at low frequencies in the range of kHz up to MHz, while the TDTR heterodyne experiment can probe the response at high frequencies from MHz up to THz.

Figure 3-2 shows the spectral response in amplitude and phase calculated by the 1TM for the sample with $k_{sub}=1 W/m/K$. To analyze the spectral response behavior, the spectrum is divided into four different regions (A, B, C, D) corresponding to different frequency behaviors.

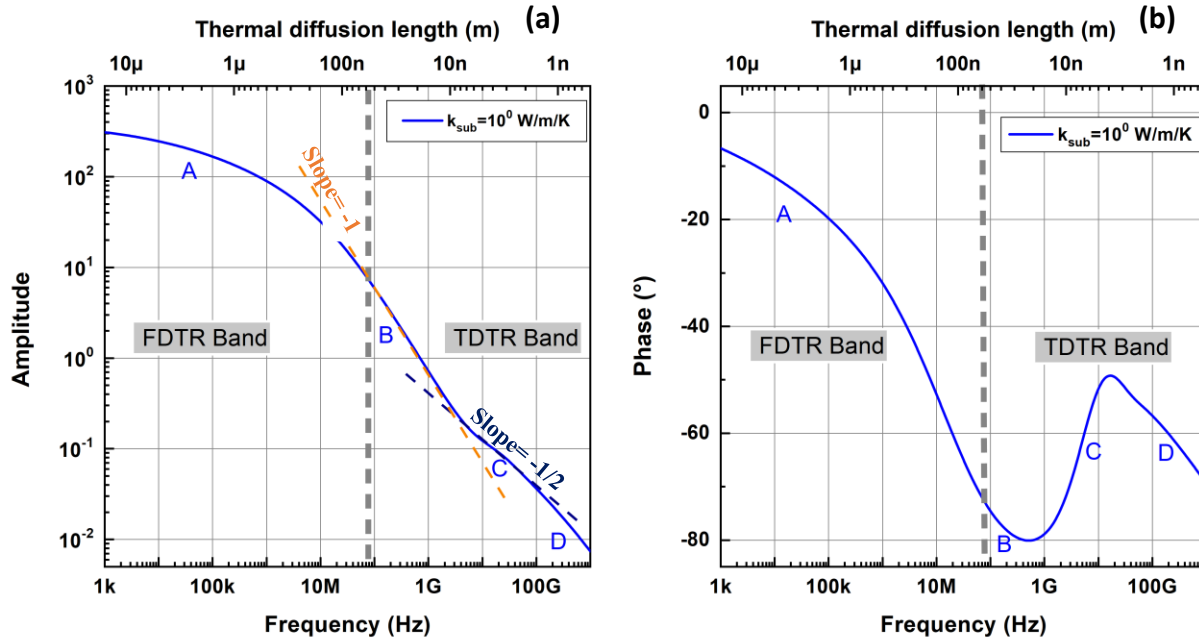


Figure 3-2: The theoretical spectral responses in (a) amplitude and (b) phase obtained by the 1TM for the sample with $k_{sub}=1$ W/m/K.

Region A is the frequency range where the heat flow has passed completely and been transferred by the transducer to the underlying layer. At the low frequencies of this region and specifically when the diffusion length becomes bigger than the pump size ($L_h \gg r_p = 5 \mu\text{m}$), the heat transfer approaches the 3D temperature distribution presented in equation 3.47. Region B, which appears with a slope of -1 in the amplitude response (**Figure 3-2(a)**), is the frequency range where the temperature is homogeneous in the transducer after the heat thermalization. Region C appears with a slope of 1/2 in the amplitude response and the corresponding phase goes toward -45° (**Figure 3-2(b)**). This is the frequency range where the surface temperature is approximated by the 1D distribution presented in equation 3.48. This is due to the heat diffusion length that becomes smaller than the laser spot size ($L_h \ll r_p = 5 \mu\text{m}$); therefore, the transducer film becomes a semi-infinite medium for the heat. Finally, region D is the high frequency range where the heat is no longer 1D due to the finite extension of the pump and the probe.

In order to see the response behavior of other material types, **Figure 3-3** presents the theoretical spectral responses, in amplitude and phase, for different thermal conductivities of substrate.

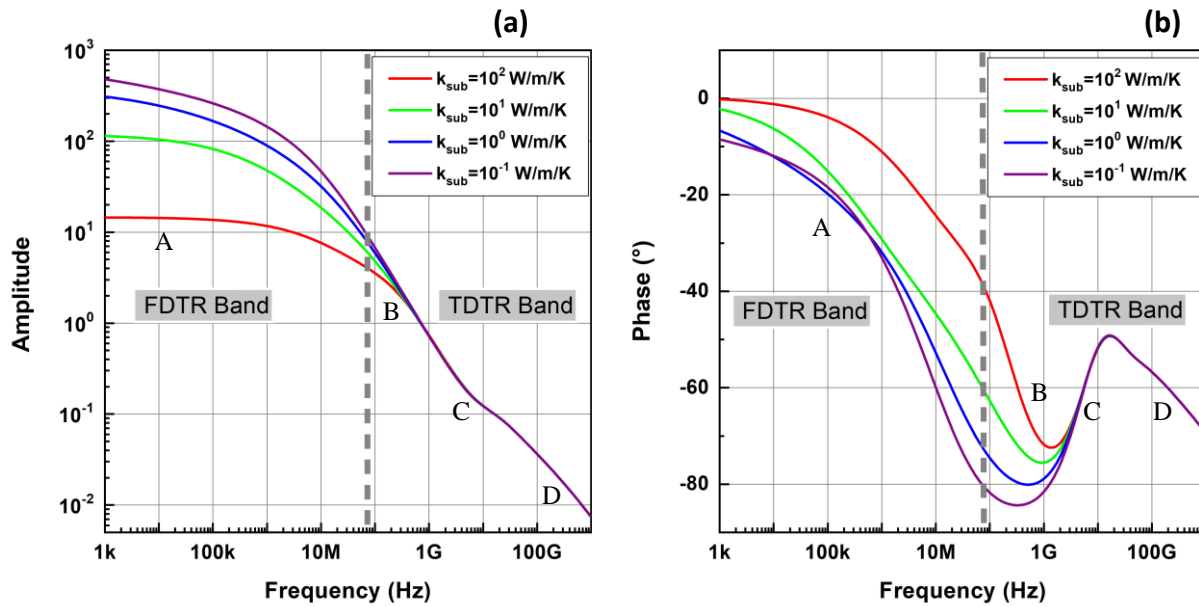


Figure 3-3: The theoretical spectral responses in (a) amplitude and (b) phase obtained by the 1TM for different material thermal conductivities.

The amplitude response presented in **Figure 3-3(a)** shows the dependence on the thermal conductivity of the substrate at low frequencies (region A). The estimated temperature amplitude at the surface increases when the sample becomes thermally insulated, due to the slower heat dissipation in the medium. On the other hand, the amplitude response beyond 100 MHz (regions B, C and D) is identical for all the studied samples. This is due to the transient thermal effects in the same transducer deposited above each substrate.

As for the phase response shown in **Figure 3-3(b)**, the semi-infinite substrate no longer exhibits a phase shift between the response and the thermal excitation, and its phase consequently tends towards 0° at low frequency (region A). In this case, the increase in the thermal conductivity of the substrate leads to a significant heat dissipation. These materials will have larger thermal diffusion length and therefore smaller phase lags over a given frequency range, than materials with low thermal conductivity. On the other hand, due to the transducer thermal effect, the phase response of the different samples behaves in a similar way beyond 1 GHz. This means the phase response has more sensitivity to the thermal effect of the material of interest rather than the amplitude.

3.3.3 Influence of transducer thickness on the sensitivity of thermal properties

As we have seen in the second chapter, the thickness of the transducer affects the heat transfer to the layer of interest, which then means an effect on the sensitivity to thermal parameters. For that, we carried out a sensitivity study of thermal parameters depending on the transducer thickness. The parameters chosen for this study are those on which depends the layer of interest: the thermal conductivity (K_{sub}) and the thermal resistance at the interface ($R_{Al/sub}$). The amplitude and the phase sensitivity curves for the case of 10 W/m/K substrate are shown in **Figure 3-4**. The shape of the curves for the other substrates, with different thermal conductivities, is almost identical.

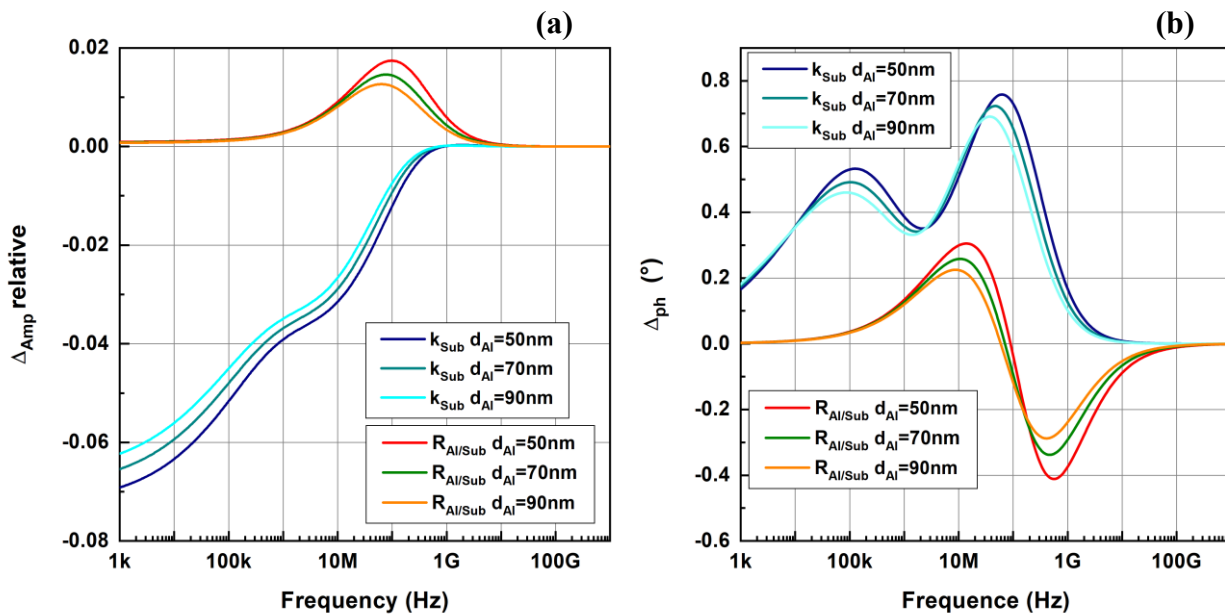


Figure 3-4: Sensitivity (a) in amplitude and (b) in phase to the thermal conductivity k_{sub} and to the interface resistance $R_{Al/sub}$ for several thicknesses of the transducer.

The thermal response in amplitude and phase (**Figure 3-4(a)** and **(b)**), for the different transducer thicknesses, is sensitive to the thermal resistance at high frequencies. The influence of the substrate thermal conductivity remains slightly weak compared to the thermal interface resistance. From a temporal point of view, when the energy deposited in the transducer dissipates towards the

surrounding environment, the heat flow encounters a thermal barrier that is the interface resistance between the two transducer/substrate layers. This explains the influence of the sensitivity to thermal resistance at high frequencies.

In addition, we can also notice on the simulated curves that the sensitivity (amplitude and phase) of the studied thermal parameters of the substrate depends on the thickness of the transducer. The thicker the transducer, the less sensitive is the surface to both the thermal conductivity and the interface resistance; and vice versa. Therefore, the best choice for thermal identification is the thin transducer, which brings a rapid transfer of its energy (chapter 2) and a great sensitivity to the thermal properties of the layer of interest located below.

3.3.4 Asymptotic behavior

In the context of thermal characterization, it is interesting to study the sensitivity of the model response to the properties that govern the heat exchange of materials. Among these properties, there is the thermal conductivity and the thermal capacity of the material of interest. In this part, we will investigate if it is possible to identify these two thermal parameters simultaneously in a wide measurement frequency range. This analysis will be carried out for the amplitude and the phase of the spectral response for the 4 materials with different thermal conductivities [$10^{-1} - 10^2$ W/m/K].

➤ Sample with $k_{\text{sub}}=10^2$ W/m/K

Figure 3-5 presents the curves of the 1TM sensitivity to the thermal conductivity and the specific heat of the sample with $k_{\text{sub}}=10^2$ W/m/K. For the amplitude spectral response (**Figure 3-5(a)**), the sensitivity curves are correlated with frequencies higher than 20 MHz. Indeed, at these frequencies, the thermal diffusion length decreases and becomes lower than the size of the laser spot ($L_h < r_p=5$ μm). The heat transfer in this case approaches the one-dimensional limit (1D) and then the surface temperature is determined by the effusivity, as equation 3.48 has shown. At lower frequencies, where the diffusion length becomes bigger than the size of the spot ($L_h > r_p=5$ μm), the correlation

no longer exists. The specific heat sensitivity decreases till the amplitude response becomes only sensitive to the thermal conductivity, and this corresponds to the three-dimensional temperature distribution that have been presented in equation 3.47.

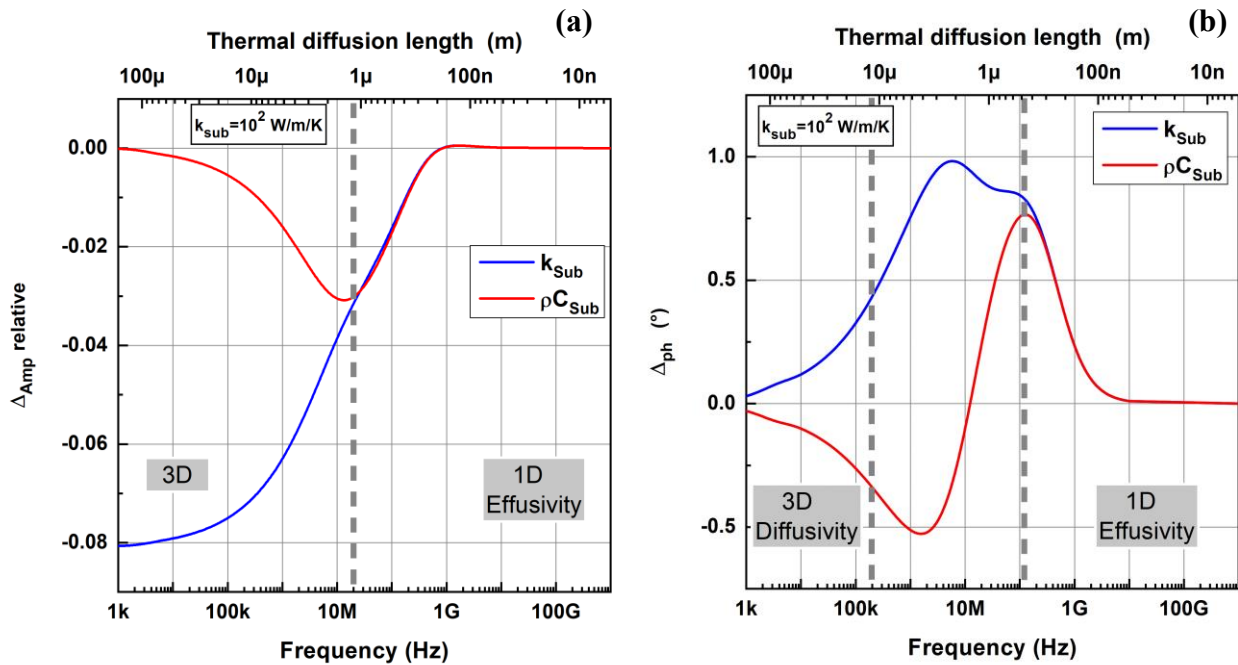


Figure 3-5: 1TM sensitivity in (a) amplitude and (b) phase to the thermal conductivity and the specific heat of the sample $k_{\text{sub}} = 10^2 \text{ W/m/K}$.

On the other hand, for the phase response (**Figure 3-5(b)**), the sensitivity to the thermal conductivity and the specific heat are correlated above the modulation frequency of 100 MHz. The thermal model is then sensitive to the substrate thermal effusivity. At lower frequencies, the two curves are separated for the magnitude, but they become correlated in absolute values (opposite signs) below the 200 kHz. In this case, the heat transfer approaches the three-dimensional (3D) limit with a phase response sensitive to the substrate thermal diffusivity.

For this sample, the simulation study showed that there is an intermediate frequency range (between 200 kHz and 30 MHz), where the sensitivity to the thermal conductivity and the thermal capacity are not correlated. Therefore, the two thermal properties can be identified simultaneously

from measurements that span this frequency range. On the other hand, for a measurement in the correlation range, the determination of the thermal conductivity requires fixing the heat capacity in the identification model; and vice versa.

➤ **Sample with $k_{sub}=10$ W/m/K**

The same previous study was carried out for the sample with $k_{sub}=10$ W/m/K. The 1TM sensitivity curves to the thermal conductivity and the thermal capacity of the substrate are presented in **Figure 3-6**.

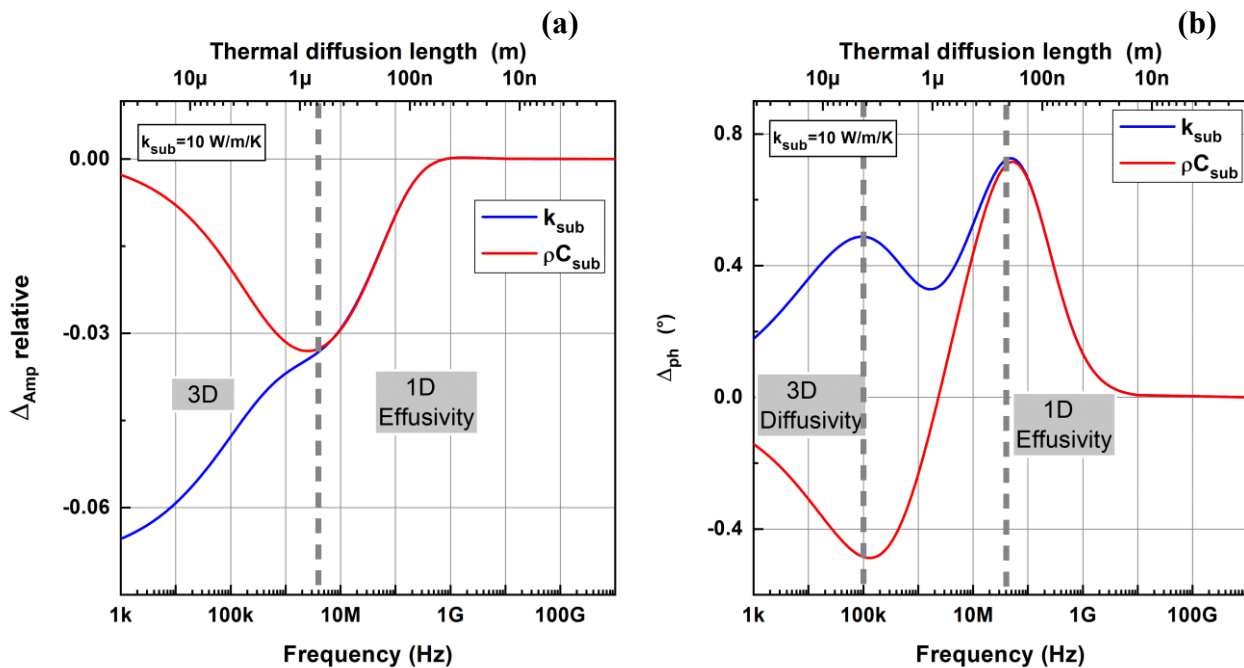


Figure 3-6: 1TM sensitivity curves in (a) amplitude and (b) phase to the thermal conductivity k_{sub} and to the specific heat ρC_{sub} for the sample with $k_{sub}=10$ W/m/K.

The sensitivity curves to the thermal conductivity and the specific heat are correlated for frequencies above 6 MHz for the amplitude and 30 MHz for the phase. This effusivity sensitivity, which is due to the one-dimensional heat flow within the sample, exists in a frequency range greater than the previous case for substrate with high thermal conductivity. At lower frequencies,

the two sensitivity curves to the thermal parameters separate and the distribution of the heat transfer becomes three-dimensional. For the amplitude response, the thermal conductivity can be uniquely determined. As for the phase, the response at a frequency less than 100 kHz is sensitive to the substrate diffusivity because sensitivity to both the thermal conductivity and the heat capacity are correlated in absolute value.

In this case, even if the sensitivity to the thermal effusivity increases, the thermal conductivity and the heat capacity can be identified simultaneously from 100 kHz to 6 MHz.

➤ **Sample with $k_{sub}=1$ and 10^{-1} W/m/K**

In order to complete the sensitivity study for the different types of materials, the same study is carried out for a material with low thermal conductivity. **Figure 3-7** shows the sensitivity curves of the thermal conductivity and the specific heat for a sample with $k_{sub}=1$ W/m/K and another with $k_{sub}=10^{-1}$ W/m/K.

For the case of substrates with low thermal conductivity values, the surface temperature is only sensitive to the thermal effusivity. The sensitivity curves for the thermal conductivity and the specific heat parameters are correlated over the entire typical acquisition frequency range, especially for the substrate with $k_{sub}=10^{-1}$ W/m/K. Indeed, the thermal insulated materials have shorter thermal diffusion length. This latter remains smaller than the size of the laser spot ($L_h < r_p$) even at low frequencies, always resulting to the one-dimensional heat transfer within the sample. In this case, the identification of the thermal conductivity and the thermal capacity cannot be carried out simultaneously. It will be necessary to fix one of the two parameters to identify the other in any measurement frequency range.

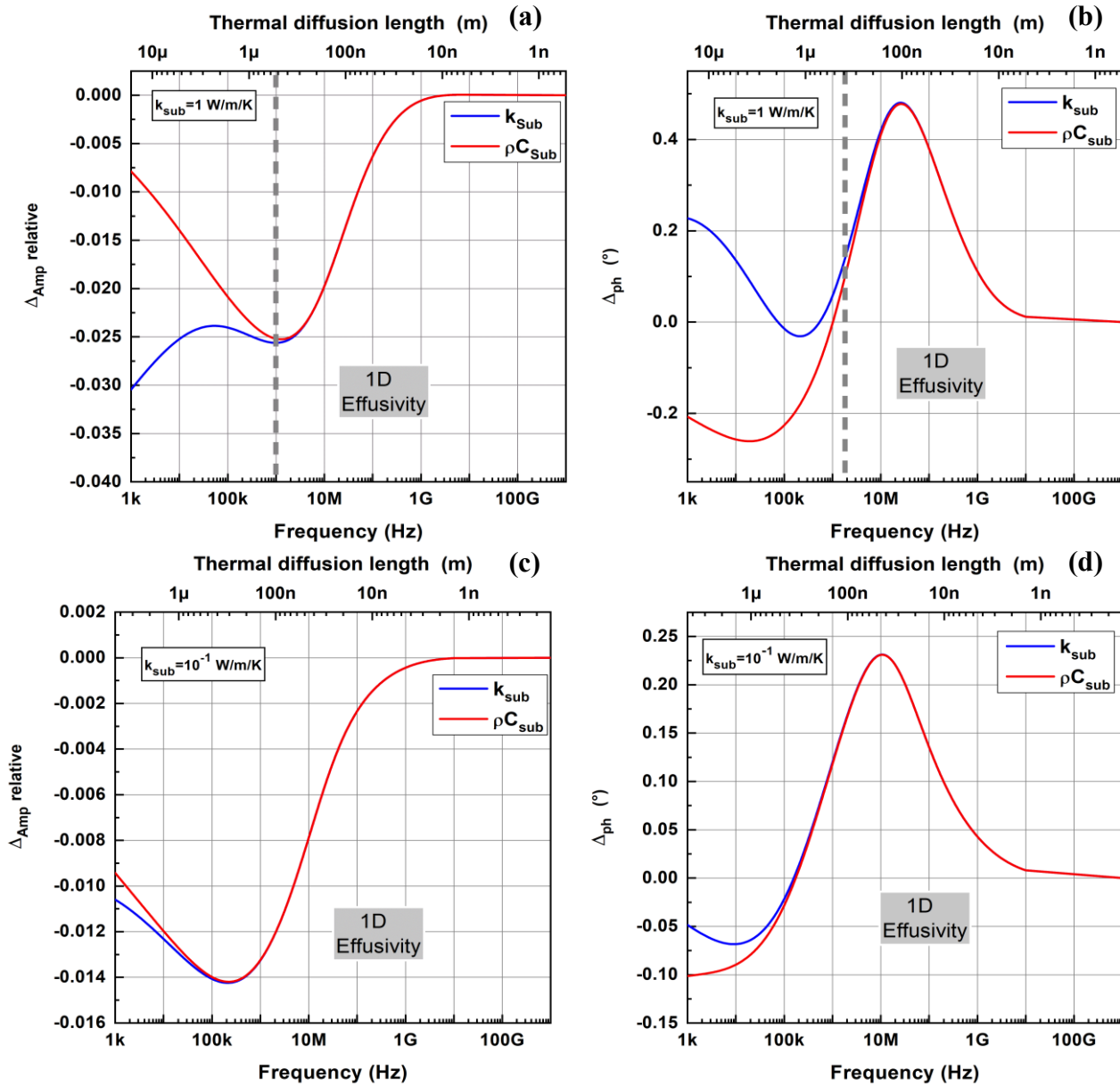


Figure 3-7: 1TM sensitivity curves in (a), (c) amplitude and (b), (d) in phase to the thermal conductivity and the specific heat for the sample with (a), (b) $k_{\text{sub}}=1 \text{ W/m/K}$ and (c), (d) $k_{\text{sub}}=10^{-1} \text{ W/m/K}$.

3.3.5 Additional thermal parameters sensitivity

In the identification process of thermal properties, at least two unknown parameters can be determined. For this, a study of the 1TM sensitivity to different thermal parameters is carried out in order to show their impact on the spectral response and indicate which of those should not be identified simultaneously. In addition to the thermal parameters of the layer of interest studied above, this part also presents the sensitivity to transducer thermal properties (thickness, thermal conductivity, and specific heat), the thermal resistance at the interface as well as the sensitivity to the size of the spot. This sensitivity analysis is performed for samples with high and low thermal conductivities of $k_{sub}=10^2$ W/m/K and $k_{sub}=1$ W/m/K, respectively.

Figure 3-8 shows the 1TM sensitivity curves, in amplitude and in phase, to the different thermal properties for the sample of Al/substrate with $k_{sub}=10^2$ W/m/K. We can see that the sensitivity of transducer thermal properties, presented in **Figure 3-8(a)** and **(b)**, only exists at high frequencies, which corresponds to the TDTR band analysis. This sensitivity becomes negligible at frequencies corresponding to the FDTR range, especially the thermal conductivity k_{Al} . The low impact of transducer parameters is due to the rapid heat thermalization towards the underling layer, which is here also a good conductor of heat. This explains the important sensitivity of the response to the parameters of the substrate layer as shown in **Figure 3-8(c)** and **(d)**. The TDTR response has a good sensitivity to the interface thermal resistance $R_{Al/sub}$. However, the FDTR frequency range is more sensitive to the thermal conductivity k_{sub} and to the specific heat ρC_{sub} of the substrate material with no correlation. On the other hand, the significant influence of the pump size r_p is limited at the FDTR frequency range. Thus, for thermal identification of this material type, measuring a response over this wide frequency range (FDTR and TDTR) allows the identification of several thermal parameters simultaneously, such as k_{sub} , $\rho C_{Al/sub}$ and $R_{Al/sub}$.

It should be noted that in this study, we did not represent the response sensitivity to the probe size that has the same effect as the pump size.

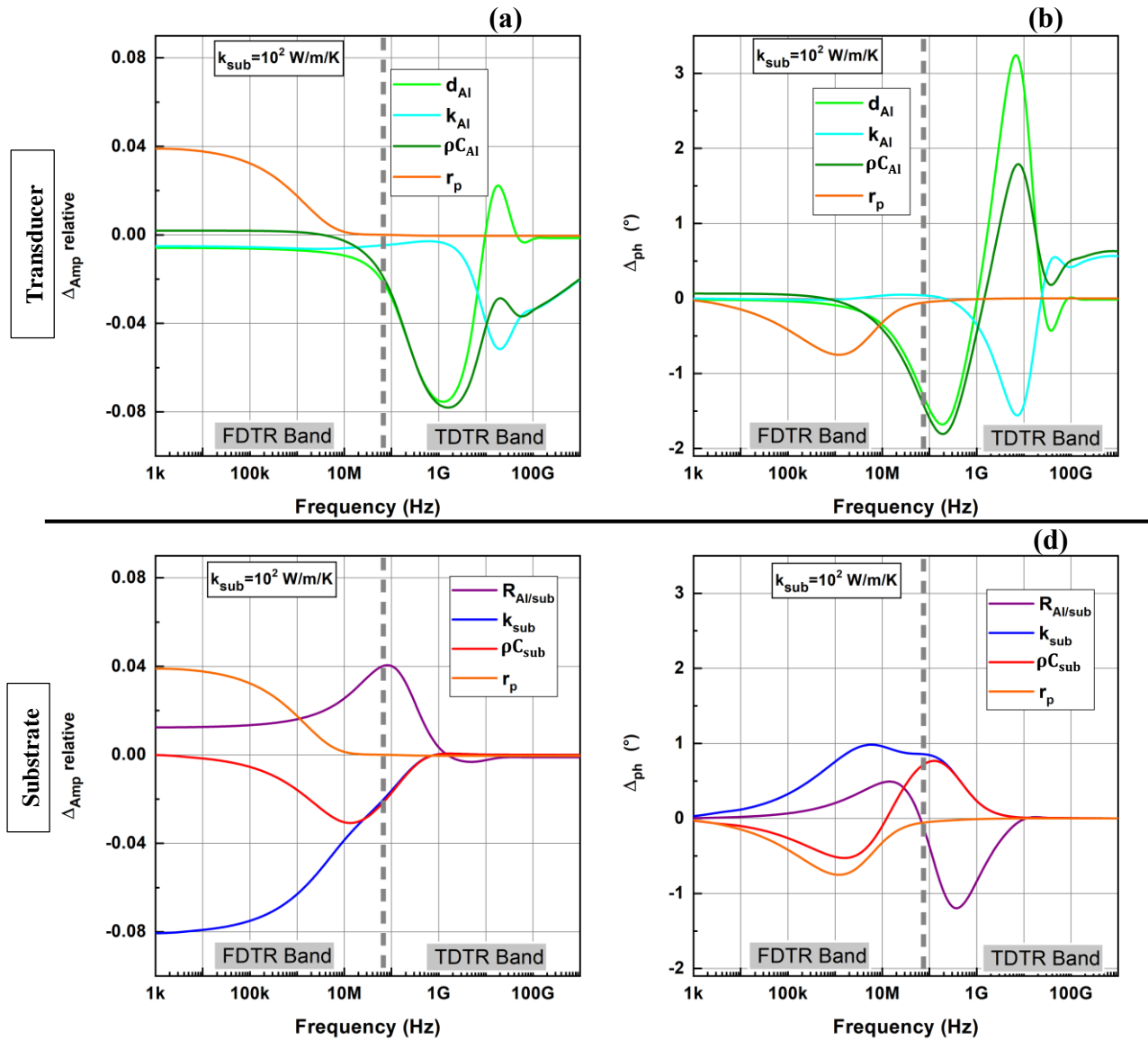


Figure 3-8: Sensitivity (a), (b) for transducer thermal properties and (c), (d) for material properties in (a), (c) amplitude and (b), (d) phase for the sample with $k_{\text{sub}}=10^2 \text{ W/m/K}$.

The nature of the substrate strongly affects the sensitivity to the different thermal parameters. **Figure 3-9** presents the curves of the 1TM sensitivity to thermal properties, in amplitude and in phase, for the sample with $k_{\text{sub}}=1 \text{ W/m/K}$. In this case, the sensitivity to the transducer parameters (**Figure 3-9(a), (b)**) is dominant in both FDTR and TDTR frequency range. On the other hand, the sensitivity to the interface thermal resistance $R_{\text{Al/sub}}$ (**Figure 3-9(c), (d)**) is low in the whole frequency range. Indeed, when the substrate is an insulator, its thermal resistance becomes much

higher than the interface resistance. Therefore, the influence of the thermal response to this parameter becomes very weak. Moreover, the low conductivity of the underlying material k_{sub} leads to an accumulation of energy in the transducer, then to a significant influence of its thermal properties on the spectral response.

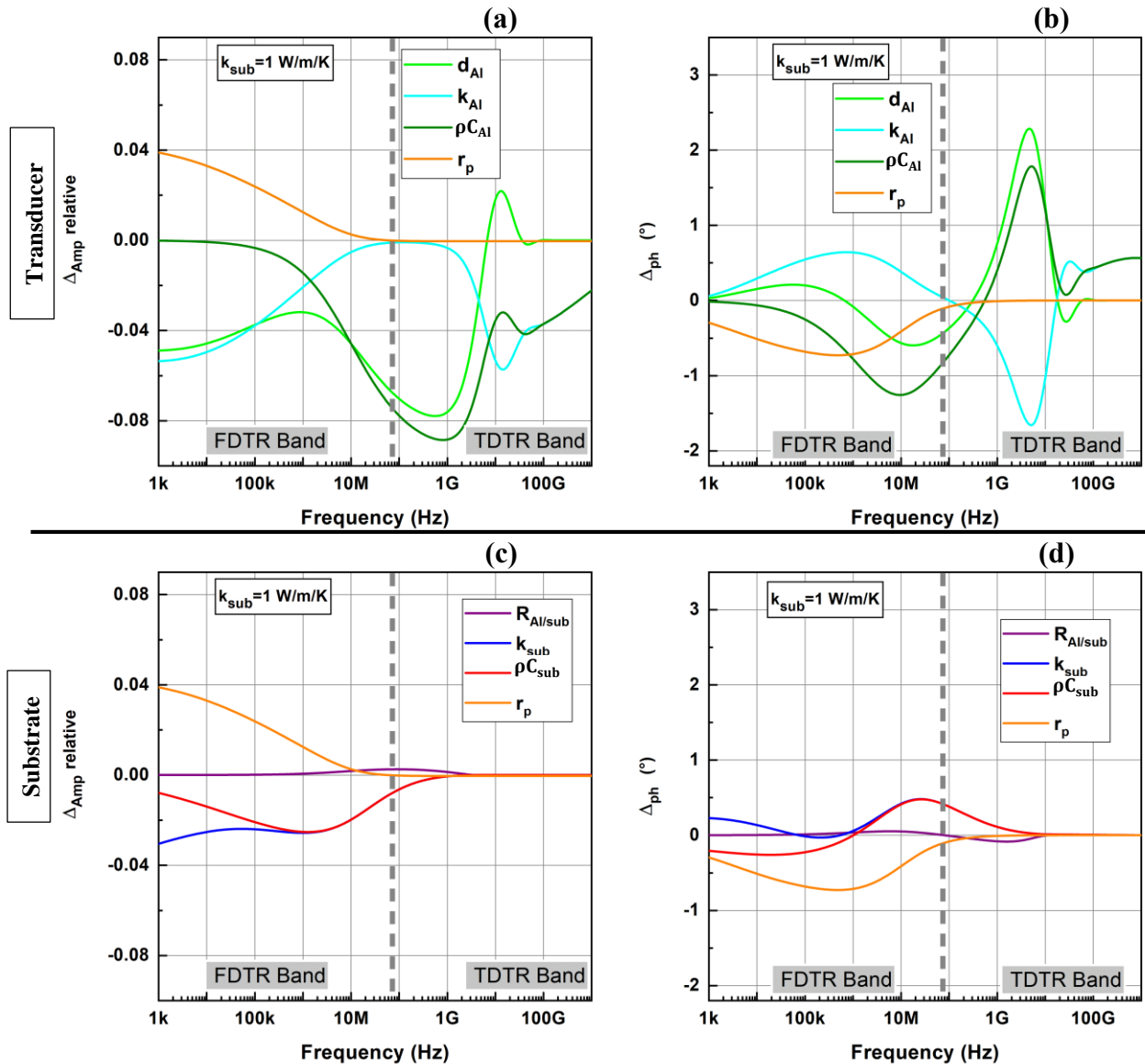


Figure 3-9: Sensitivity (a), (b) of transducer thermal properties and (c), (d) of material properties in (a), (c) amplitude and (b), (d) phase for the sample with $k_{sub}=1$ W/m/K.

It is noted also that the influence of the pump size on the thermal response still occurs at low frequencies as the previous study with $k_{sub} = 10^2$ W/m/K. As for the substrate properties, the response is sensitive to the thermal effusivity. This is due to the correlation between k_{sub} and $\rho C_{Al/sub}$ sensitivities in all the frequency range measurement of FDTR and TDTR. Therefore, in this type of material, the thermal conductivity k_{sub} can only be determined by fixing the specific heat $\rho C_{Al/sub}$ in the model.

Consequently, the dominant parameters in the thermal response are strongly dependent on the insulating nature of the studied substrate. According to this nature and the measured frequency range, certain parameters can only be identified by fixing certain others, due to the correlation sensitivity. Thus, the wide bandwidth of the spectral response increases measurement sensitivity and enables enhanced simultaneous thermal property characterization of the material of interest.

3.4 Ultra-broadband spectral thermal sensor from 10 kHz to 1 THz

In this section, we will first describe how we combined two experiments in order to obtain a broadband thermal spectral sensor. In a second step, we will show the capacity of this sensor by experimental results of thermal characterization for several types of materials.

3.4.1 Spectroscopic measurements via combined time- and frequency-domain thermorefectance.

As we have seen in the 1TM sensitivity study, the identifiable thermal parameters depend on the measured frequency range. The wide spectral band of the system increases the measurement sensitivity, and enables multiple combinations of thermo-physical properties to be simultaneously extracted from a single measurement. In this work, we apply a broadband spectral sensor using a dual of TDTR and FDTR experimental methods. This technique is a very valuable tool linking the

advantages of the two methods for thermal characterization. The combined measurements allow to investigate the thermal transport on a wide frequency range from kHz up to THz.

3.4.1.1 Spectral sensor setup

The experimental setup used in this work for the FDTR thermoreflectance method is shown in **Figure 3-10**. The pump and the probe are continuous beams (CW) generated by two laser diodes emitting different wavelengths 810 nm and 780 nm, respectively. The pump beam is modulated sinusoidally in amplitude by a radiofrequency generator.

The pump and probe beams are focused on the sample surface by a microscope objective with a magnification of 10X. They have a respective radius of 6.5 μm and 4.5 μm on the sample surface measured using a coherent beam master. Following the reflection, the probe beam is returned to a silicon photodiode passing through an interference filter preventing any detection of the reflected pump beam during the measurement. The phase-shift of the temperature (probe) to the heat flux (pump) is monitored by a lock-in amplifier synchronized on the modulation frequency. This FDTR setup produces a high-fidelity thermal signal and allows heating frequencies up to 200 MHz. Increasing the frequency beyond 200 MHz causes signal-to-noise issues, because the amplitude of the temperature response decreases, whereas coherent and ambient noise increase. However, achieving this high frequency measurement is very important for thermal study, because the most recent FDTR-based techniques do not modulate the pump laser higher than 20 MHz [73-74].

For the TDTR method, we use the heterodyne setup presented in chapter 2 (see **Figure 2-6**). In this study, the optical parametric oscillator used to change the probe wavelength is removed. Therefore, the wavelength of the probe will be 780 nm, which is suitable for thermoreflectance measurements with the Al transducer deposited on the studied samples.

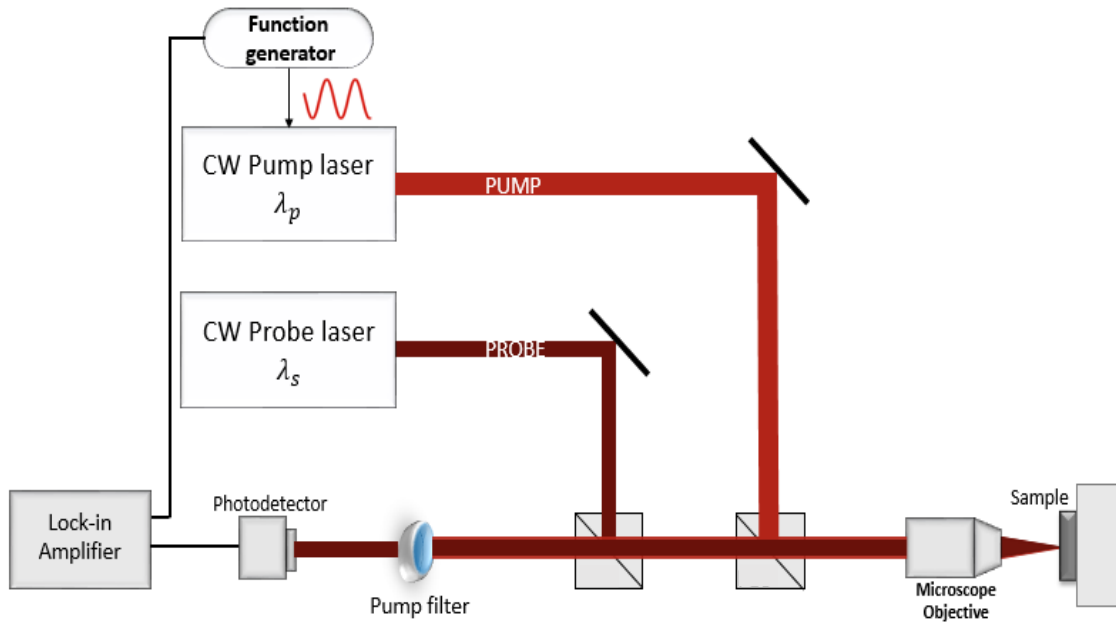


Figure 3-10: Schematic of the FDTR setup used for the thermal sensor.

3.4.1.2 Ultra broadband spectroscopy

In order to show the capacity of the thermal spectral sensor, an experimental measurement was carried out for a silica sample. **Figure 3-11** presents the wide thermal response in amplitude and in phase obtained by combined measurements of FDTR/TDTR methods. The FDTR experiment accesses the frequency response of the sample for a range from 10 kHz to 200 MHz, while the TDTR experiment probes frequencies from 76 MHz up to 1 THz. Hence, the overlap between the two measurements leads to an ultimate thermal spectroscopy with a bandwidth extending from 10 kHz to 1 THz.

It should be noted that the spectral response of the TDTR heterodyne is obtained by performing a Fourier transform of the measured temporal response.

The overlap between the FDTR and TDTR in amplitude and in phase response is possible because we use the same conditions for measurement in the two methods, which are the microscope objective, pump, probe wavelengths and of course the same studied sample. In addition, the

amplitude response depends on the absorbed energy within the sample, which requires the use of the same pump power.

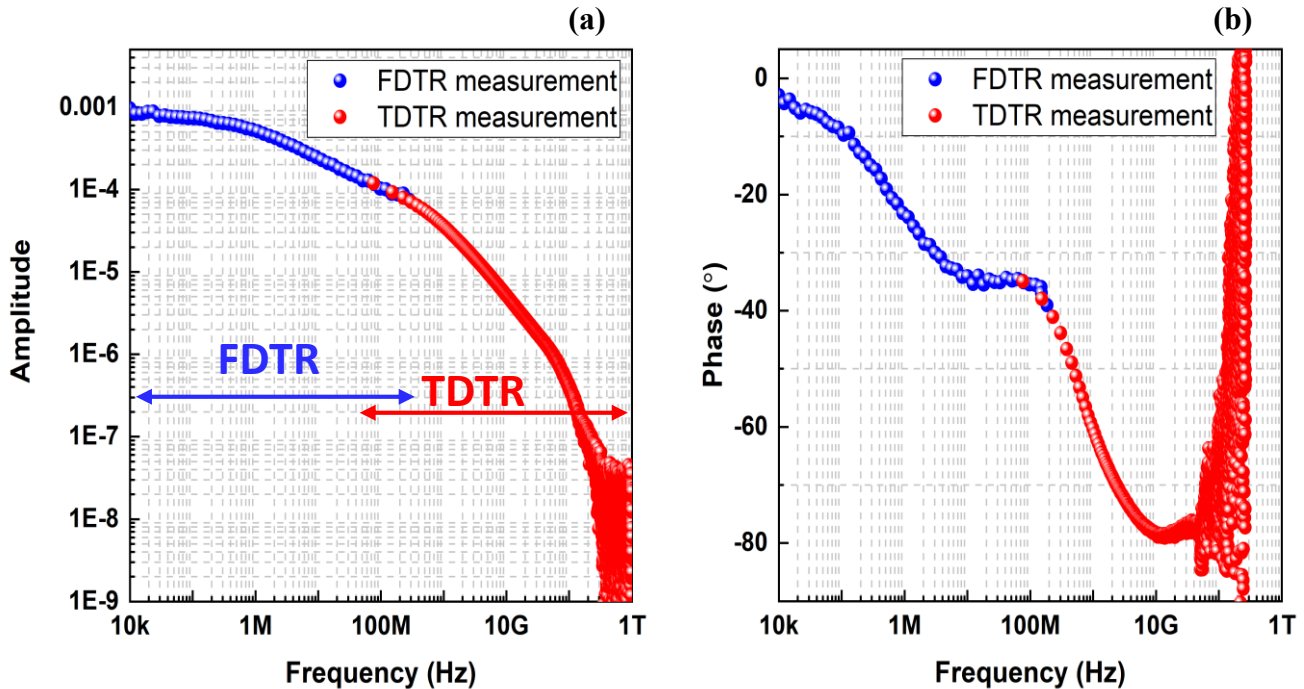


Figure 3-11: spectral response in (a) amplitude and (b) phase of Si sample measured by the thermal sensor FDTR/TDTR.

Moreover, the sensitivity study showed that the TDTR response is not sensitive to the laser spot radius (see **Figure 3-8**). Therefore, any small variation in the size of the TDTR beam lasers (pump or probe), compared to those of FDTR, will not have any influence especially on the phase response.

The next part of this work consists in identifying thermal properties from the response of the FDTR/TDTR sensor. For this, we will focus on the measured phase response, which is independent of the wavelength and the power of the laser. The thermal identification model was carried out with the 1 TM on the phase response up to 10 GHz in frequency, being the ultimate phononic range of the Al transducer, as we have seen in chapter 2.

3.4.2 Over 3 decades thermal conductivity identification

The wide spectral response provided by the thermal sensor FDTR/TDTR allows us to measure the different thermal behaviors in nanomaterials. The reliability and the capacity of these measurement techniques for thermal characterization has been verified on a series of material samples over a wide range of thermal conductivity values.

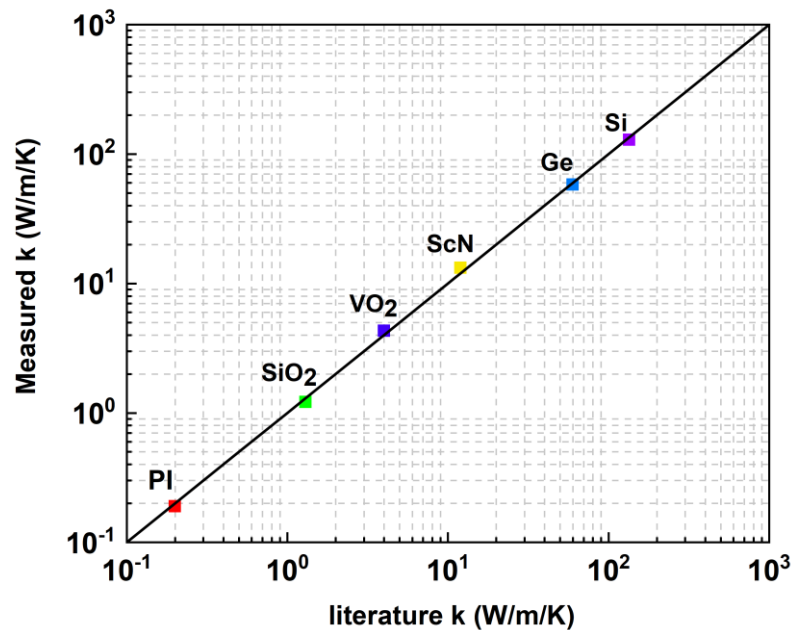


Figure 3-12 TDTR/FDTR sensor measurements of a wide range of materials thermal conductivity.

Figure 3-12 shows studies of the thermal spectral sensor over a wide range of thermal conductivity, from 10^{-1} to 10^2 W/m/K. These thermal characterizations carried out during the thesis work include several materials: silicon (Si), germanium (Ge), scandium nitride (ScN), vanadium dioxide (VO₂), silica (SiO₂) and a polymer (PI). The thermal conductivities of these materials determined by the One-Temperature Model are in good agreement with the literature values with an overall experimental uncertainty of $\pm 5\%$ [58, 75–80]. In the following we will show some detailed examples for the thermal identification of these studied materials.

It should be noted that in this study, the size of the pump and the probe are known model parameters at the values of the FDTR method. The radius values described before are $6.5 \mu\text{m}$ for the pump and $4.5 \mu\text{m}$ for the probe.

➤ Silicon Si

The first thermal identification example is for the silicon layer. The structure of the sample consists of a 40 nm thick aluminum transducer deposited on a semi-infinite Si substrate.

According to the thermal sensitivity studies presented in section 3.3, three parameters will be identified simultaneously with the wide response of the FDTR/TDTR sensor. These parameters, which will be left free during the identification process, are the thermal conductivity and the heat capacity of Si, and the thermal resistance $R_{Al/Si}$ at the interface. The other properties are assumed to be known and fixed at the values shown in **Table 3-1**.

Transducer Al	Penetration depth	$e_{Al}=7 \text{ nm}$
	Thickness	$d_{Al}=32 \text{ nm}$
Substrate Si	Thermal conductivity	$k_{Al}=180 \text{ W/m/K}$
	Specific heat capacity	$C_{Al}=2.45 \text{ MJ/m}^3/\text{K}$
	Thermal resistance	$R_{Al/Si}= ? \text{ nK} \cdot \text{m}^2/\text{W}$
Substrate Si	Thermal conductivity	$k_{Si}= ? \text{ W/m/K}$
	Specific heat capacity	$\rho C_{Si}= ? \text{ MJ/m}^3/\text{K}$

Table 3-1: Fixed and to be identified thermal properties for the Al/Si sample.

In order to extract the desired thermal properties, the numerical optimization is performed on the measured phase response by FDTR/TDTR. **Figure 3-13** shows the optimization and the experimental curves of Al/Si sample as well as the residuals, which represent the subtraction between the two curves. The best optimization is obtained for a thermal conductivity of $k_{Si}=135 \text{ W/m/K}$, a specific heat capacity of $\rho C_{Si}=1.69 \text{ MJ/m}^3/\text{K}$, and an interface resistance of $R_{Al/Si}=2.3$

nK.m²/W. The identified values are very close to those found in the literature [75, 76] from where the thermal conductivity values vary around 140 W/m/K. The residuals obtained during the optimization show a small difference between the experimental measurement and the theoretical response of the 1TM.

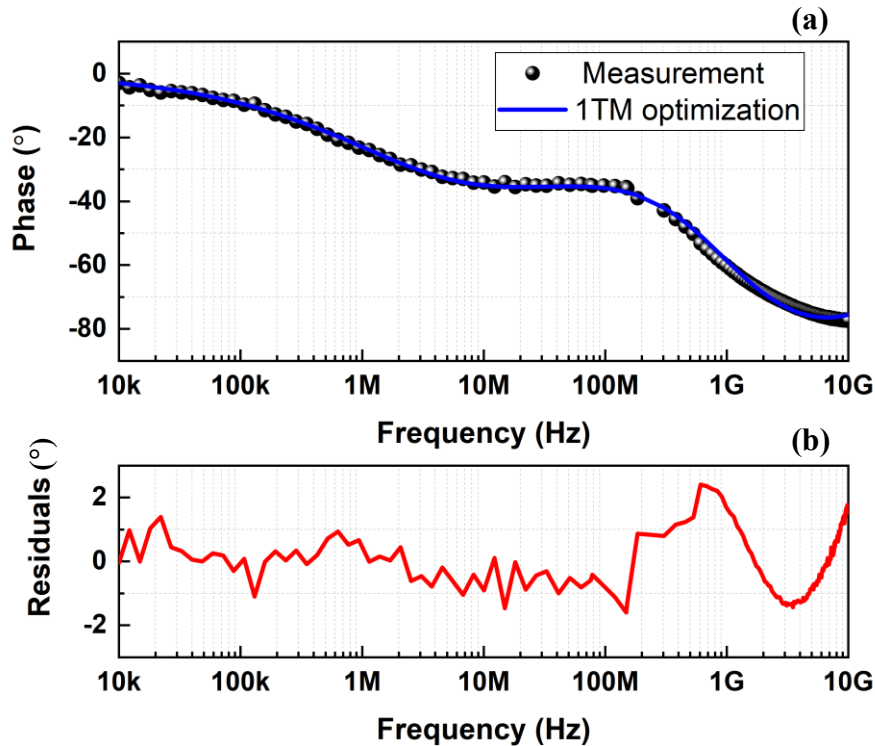


Figure 3-13: (a) Typical phase data measured by the FDTR/TDTR sensor and the best 1TM fit for Al/Si sample. (b) Optimization residuals.

➤ Scandium nitride ScN

The second example of thermal characterization is for the ScN layer. The studied sample is a 240 nm ScN layer, deposited on a sapphire substrate, on which a 70 nm aluminum transducer has been deposited. **Table 3-2** presents all the properties necessary for its modeling with the known values are taken from the literature [81].

Transducer Al	Penetration depth Thickness Thermal conductivity Specific heat capacity	$e_{Al}=7 \text{ nm}$ $d_{Al}=60 \text{ nm}$ $k_{Al}=180 \text{ W/m/K}$ $C_{Al}=2.45 \text{ MJ/m}^3/\text{K}$
	Thermal resistance	$R_{Al/ScN}=? \text{ nK.m}^2/\text{W}$
Layer ScN	Thickness Thermal conductivity Specific heat capacity	$k_{ScN}=? \text{ W/m/K}$ $\rho C_{ScN}=? \text{ MJ/m}^3/\text{K}$
	Thermal resistance	$R_{ScNb/Al_2O_3}=1 \text{ nK.m}^2/\text{W}$
Substrate Al ₂ O ₃	Thermal conductivity Specific heat capacity	$k_{Al_2O_3}=35 \text{ W/m/K}$ $\rho C_{Al_2O_3}=2.98 \text{ MJ/m}^3/\text{K}$

Table 3-2 Fixed and to be identified thermal properties for the Al/ScN/Al₂O₃ sample.

In this case, the properties of the sapphire substrate as well as those of aluminum are fixed at the tabulated values. The interface resistance R_{ScN/Al_2O_3} between the ScN layer and the sapphire substrate is considered negligible. Thus, three parameters are left free during the identification procedure: the thermal conductivity k_{ScN} , the specific heat capacity ρC_{ScN} and the thermal interface resistance $R_{Al/ScN}$.

The result of the optimization on the phase measurement is shown in **Figure 3-14**. The two curves are matching very well for all the frequency range. The identified values are for the thermal conductivity $k_{ScN}=12.5 \text{ W/m/K}$, the specific heat capacity $\rho C_{ScN}=3.9 \text{ MJ/m}^3/\text{K}$ and for the interface resistance $R_{Al/ScN}=14 \text{ nK.m}^2/\text{W}$.

The residuals show a small error between the experimental and the optimized curves. Moreover, the identified value of the thermal conductivity and the specific heat capacity are in agreement with both the theory and the previous results published for the ScN [77-78]. However, the identified thermal resistance is a little high, which indicates the tough grip between the aluminum and the ScN layer.

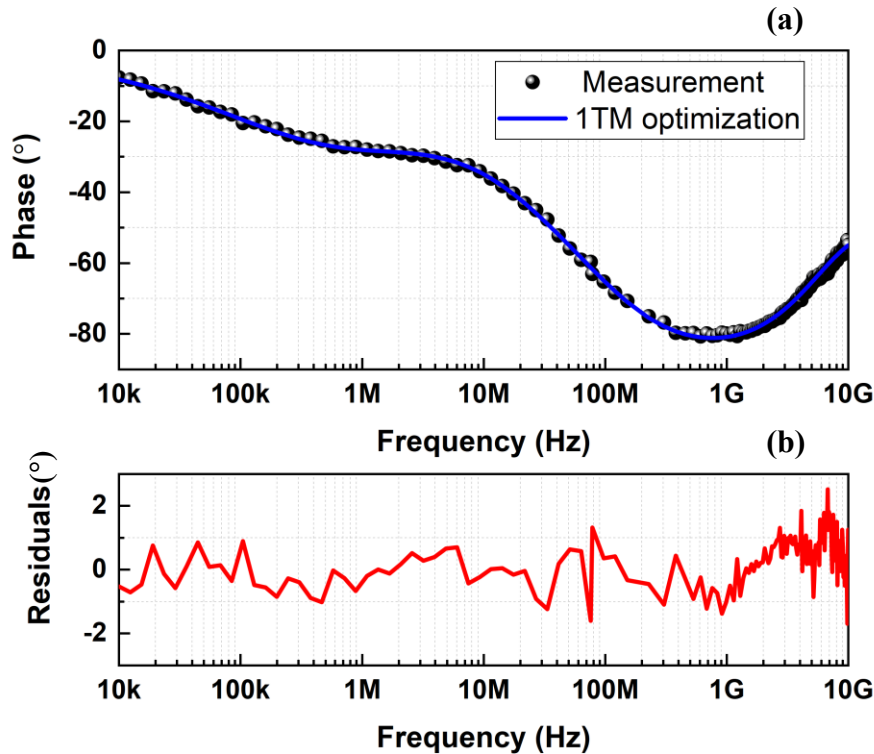


Figure 3-14: (a) Measurement curve and calculated curve for Al/ScN/Al₂O₃ sample. (b) Optimization residuals.

➤ Polyimide (PI)

The last example is for the polymer PI characterized by a low thermal conductivity. The structure consists of a semi-infinite PI substrate, on which a 70 nm thick Al transducer is deposited.

According to sensitivity studies for a thermal insulated layer, the thermal conductivity and the heat capacity cannot be identified simultaneously. For this, the heat capacity of the polymer substrate will be fixed at $\rho C_{PI} = 2 \text{ MJ/m}^3/\text{K}$. In addition, the thermal properties of the Al transducer will be also fixed as the previous sample.

The interface resistance $R_{Al/PI}$ between the Al transducer and the insulated substrate is negligible (see **Figure 3-9**). Thus, the size of the pump will be left free with the thermal conductivity k_{poly} during the optimization.

The result of the optimization on the experimental phase curve is presented in **Figure 3-15**. The best optimization is obtained for a polymer thermal conductivity of $k_{PI}=0.2$ W/m/K and for a pump radius of $r_p=6.5$ μm . The identified value of the thermal conductivity agrees with the theory, and the value of the pump size is very similar to that measured by the beam master.

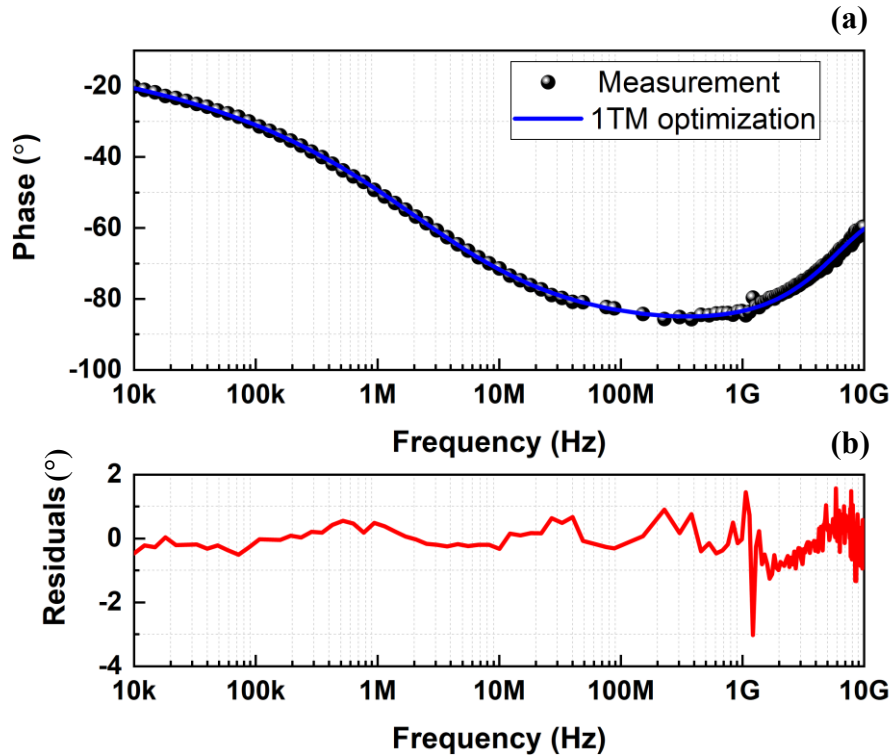


Figure 3-15: (a) Measurement and optimization curves for the Al/PI. (b) Optimization residuals.

3.4.3 Conclusion

These three examples of different samples, Si, ScN and polymer PI, illustrate three different cases for which the thermal sensor FDTR/TDTR shows its potential. First, the thermal conductivity of a thick layer of a conductive material (Si) has been identified simultaneously with the heat capacity and agrees with literature results. Then, in a multilayer sample, the thermal conductivity and heat capacity were also measured together for a thin layer (ScN), with values equal to the ones found

in the literature. Finally, the last sample illustrates the possibility of measuring the thermal conductivity of a thick layer of an insulating material (polymer). These three examples, with the other materials presented before (**Figure 3-12**), show the extent of the performance of this measurement method. Thus, the wide range thermal response makes it possible to simultaneously determine both thermal conductivity and heat capacity. It also allows to identify the properties of samples with different thermal conductivities [$10^{-1} - 10^2$ W/m/K] and thicknesses, even for a multilayer sample where the excitation is carried out on the surface of the latter.

3.5 Uncertainty analysis

In the identification procedure, there are always systematic errors that affect the uncertainty of the measured thermal properties. As we have mentioned in chapter 1, the errors are caused by one of the following main factors: experimental noise in the response, uncertainty in the fixed parameters in the model or the correlations of the free parameters. In this section, we will study and analyze in detail the influence of these factors on the determination of thermal properties.

3.5.1 Experimental noise

The confidence associated with the measured values is a critical aspect of any experimental measurement technique. Despite the widespread use of FDTR and TDTR thermoreflectance methods and their effectiveness in measuring thermal properties, noise still exists in the measured signal. This noise is generated by the artefacts inherent in this type of experiment, including the power fluctuation, the laser stability, the mechanical vibrations of the measuring bench or the electronic parasites. The noisy experimental data can affect the stability of the inverse method and lead to uncertainties on the identified values. We will study in this part the noise impact of the FDTR/TDTR sensor on the parameters determined by the inverse method (least mean squares method).

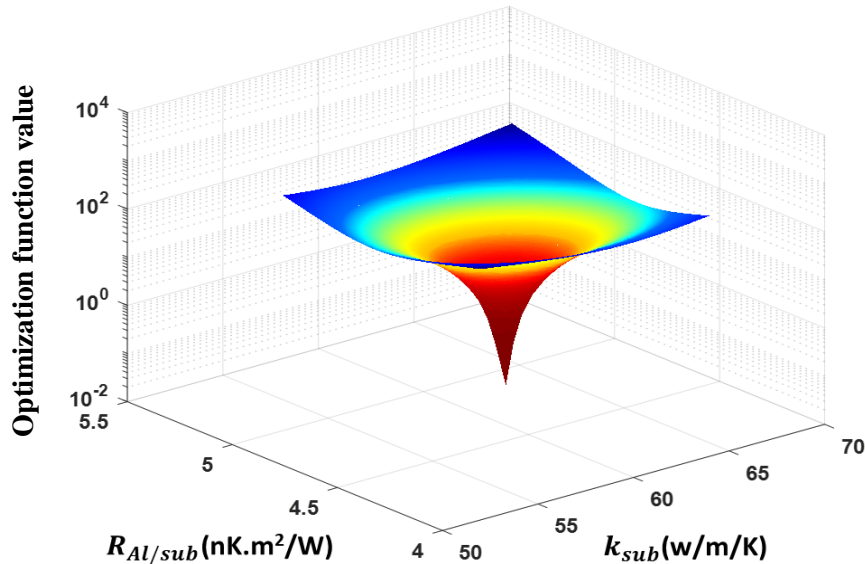


Figure 3-16: Cartographic simulation of the least squares method for the optimization on the theoretical curve as a function of the thermal conductivity k_{sub} and the thermal resistance $R_{Al/sub}$.

First, we have checked the performance of the least mean squares method in an ideal case with a response without any noise. For that, a theoretical response of Al/substrate sample provided by the 1TM is used as an experimental response for the optimization by the inverse method. During the optimization, the thermal conductivity k_{sub} and the interface resistance $R_{Al/sub}$ are left free. The other thermal parameters are fixed in the thermal model. The mapping simulation of the least mean squares variation as a function of the free parameters are presented in **Figure 3-16**.

The 3D cartographic simulation shows that the optimization algorithm converges to a unique and precise minimum. The values at this minimum are $k_{sub} = 60$ W/m/K for and $R_{Al/sub} = 4.6$ nK.m²/W, which are the same as those used to calculate the theoretical response.

After that, a measurement of the FDTR and TDTR noises was carried out in order to show its effect on the parameter's estimation by the least mean squares method. For that, the noise measurement in FDTR method was obtained by computing the standard deviations of phase data points, measured at multiple modulation frequencies. For the TDTR method, the procedure is the same, except that the phase data points are measured at multiple delay times. Then, the

experimental noises of the FDTR and TDTR are added to the 1TM theoretical response. It should be noted that the measurements in both methods were performed on an Al/Ge sample.

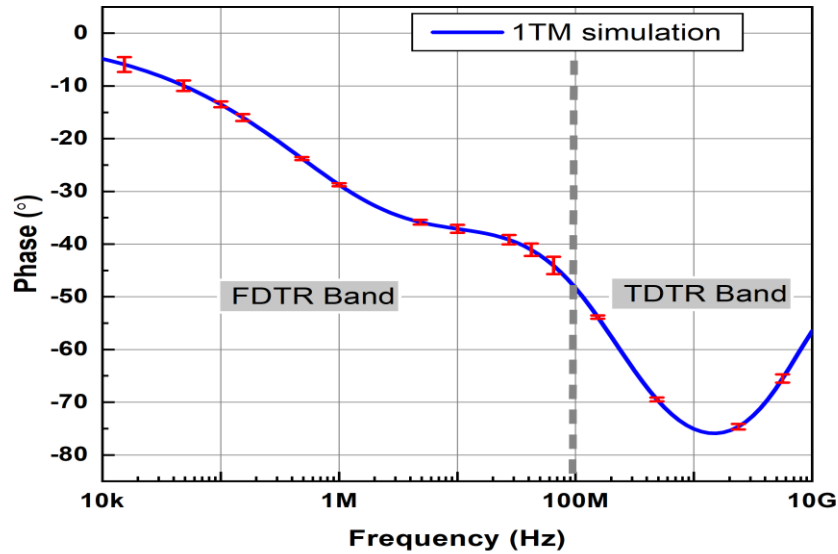


Figure 3-17: Experimental uncertainties of FDTR and TDTR measurements on a theoretical response of 1TM for an Al/substrate sample.

Figure 3-17 presents the experimental noises of the FDTR and TDTR methods on the 1TM response. It can be seen that the noise in both methods depends on the measurement frequency. In the FDTR response range, the noise generally increases at low frequencies because of the increased $1/f$ noise and also increases at high frequencies due to a lower signal to noise ratio. However, this ratio becomes better in the measurements in the TDTR response range.

An optimization was performed on the phase curve incorporated with the experimental FDTR and TDTR noises. As the previous study, the thermal conductivity k_{sub} and the interface resistance $R_{Al/sub}$ are left free. **Figure 3-18** shows the variation of the squared differences as a function of the free parameters.

The variation of the squared differences is affected by the noise and it resembles to an elliptical bowl. Although, the parameters values at the minimum are 59 W/m/K for k_{sub} and 4.65 nK.m²/W for $R_{Al/sub}$ are very close to those used to calculate the theoretical phase curve. This uncertainty

on the measured values, which is less than 3%, is due to the experimental noise of the FDTR and the TDTR methods.

Consequently, the stability of the FDTR and TDTR thermoreflectance methods makes it possible to measure signals with low artifact, which leads then to the identification of the thermal parameters with low uncertainties.

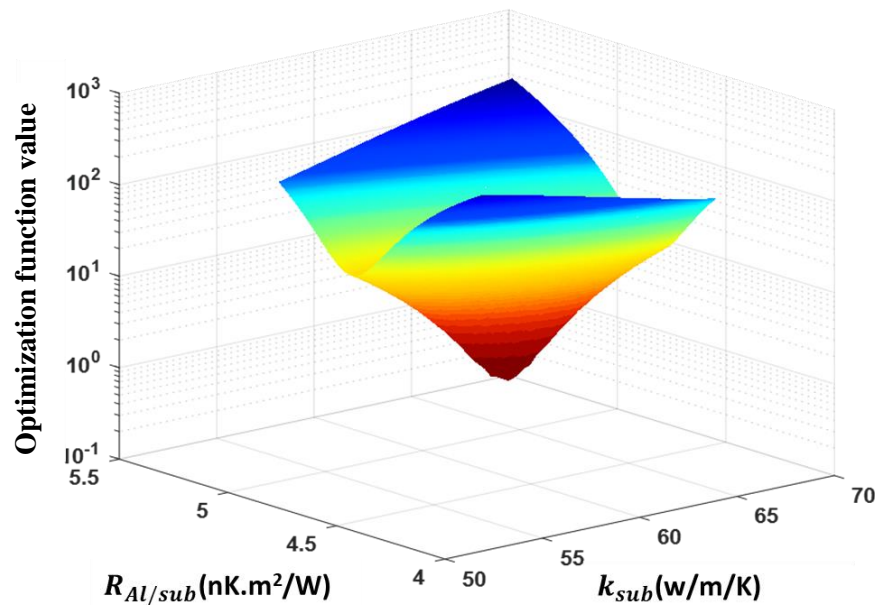


Figure 3-18: Cartographic simulation of the least squares method for the optimization on the noised theoretical curve as a function of the thermal conductivity k_{sub} and the thermal resistance $R_{Al/sub}$.

3.5.2 Fixed parameters

The second studied factor that affect the uncertainty of the determined thermal properties is the fixed parameters in the model. The underestimation of these supposedly known parameters causes errors in the identification process. For this, we have chosen to vary the fixed parameters values by assigning 10%, in order to show their effect on the identified parameters.

This study is performed on the parameters of the Al/Si sample presented previously (section 3.4). For this sample, the identified properties were set to $k_{Si}= 135$ W/m/K for the thermal conductivity and $R_{Al/Si}= 2.3$ nK.m²/W for the thermal resistance. In this case, we supposed that the heat capacity C_{Si} is among the fixed parameters to see its variation effect on the estimated parameters.

Free parameters Fixed parameters	k_{Si} (W/m/K)	Errors	$R_{Al/Si}$ (nK.m ² /W)	Errors
$d_{Al}+10\%$ (nm)	127	-6%	2.1	+8%
$k_{Al}+10\%$ (W/m/K)	136	+1%	2.3	0%
$\rho C_{Al}+10\%$ (MJ/K/m ³)	126	-7%	2.1	+8%
$\rho C_{Si}+10\%$ (MJ/K/m ³)	136	+1%	2.2	-3%
$r_p+10\%$ (μ m)	129	-5%	2.2	-3%
$r_s+10\%$ (μ m)	130	-4%	2.3	0%

Table 3-3: Estimation of the uncertainties committed on the identified parameters for the Al/Si sample.

The estimated uncertainties on the identified thermal properties for the Al/Si sample are presented in **Table 3-3**. As expected, the uncertainties of the values for the estimated properties change from one parameter to another. The highest impact on the identification comes from the thickness of the layer and the specific heat capacity of the aluminum transducer (d_{Al} and ρC_{Al}). The other parameters have less influence. This variation of the uncertainties depends on the nature of the studied sample and the sensitivity of the response to the thermal parameters.

Due to their influence on the identification, the values of the fixed parameters in the model must be chosen carefully and with high precision. Thus, any incorrect assessment of the values of these parameters causes significant uncertainties on the identified ones. This is why before any thermal identification of the studied sample, we measure the thickness of Al transducer with great precision by the heterodyne method, which detects the acoustic effects propagating in the film. As for the heat capacity, the value is well known and has been measured by many studies in the literature [82-83].

3.5.3 Correlated parameters

Another factor is causing errors on the optimization by the inverse method, which is the identification of the correlated parameters. We have seen earlier in this chapter that the sensitivity of the sample response to thermal effusivity or diffusivity is a result to the correlation between the thermal conductivity and the heat capacity. This correlation adds an error factor whether the least squares algorithm was able to find a unique global minimum in the parameter space or not, and thus will strongly affect the identified parameters uncertainty.

In order to show the influence of the correlation parameters on the thermal identification, two separate optimizations were performed on a theoretical response of Al/substrate sample. The response is calculated with the thermal properties presented previously (**Figure 3-1**, $k_{Sub}=1.3$ W/m/K).

According to the sensitivity study (see **Figure 3-9**), the first optimization was carried out with two non-correlated free parameters: the thermal conductivity k_{Sub} and the interface resistance $R_{Al/Sub}$. The second one was performed with two correlated parameters: the thermal conductivity k_{Sub} and the specific heat capacity ρC_{Sub} . **Figure 3-19** presents the 2D maps of the sum of squared differences for the two optimization cases.

In **Figure 3-19(a)**, the optimization with the uncorrelated parameters shows that the least squares algorithm leads to a unique minimum. The values of the identified parameters at this minimum are 1.3 W/m/K for the k_{Sub} and 5 MJ/m³/K for the $R_{Al/Sub}$. On the other hand, this is not the case in **Figure 3-19(b)** where the optimization with the correlated parameters shows that the algorithm was not able to find a unique solution. Indeed, the correlation between the sensitivity of k_{Sub} and C_{Sub} produces the same minima for different points in the parameter space and the optimization method can converge to any one of them. In this case, the identified physical quantity is the substrate thermal effusivity, $e = \sqrt{\rho C_{Sub} k_{Sub}}$. Therefore, all minima of the optimization simulation lead to identify the same value of the thermal effusivity as shown in **Figure 3-19(b)**.

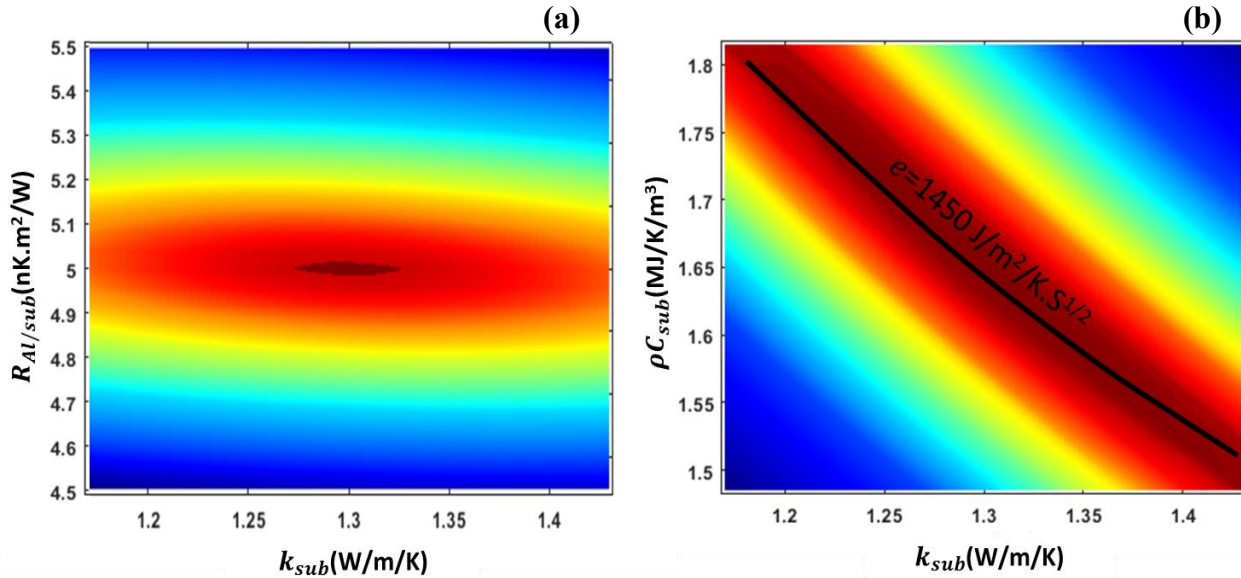


Figure 3-19: 2D cartographic simulation of the least squares method for the optimization as a function of (a) the thermal conductivity k_{sub} and the interface resistance $R_{Al/sub}$ and (b) the thermal conductivity k_{sub} and the heat capacity ρC_{sub} . The black line (b) stands for the thermal effusivity calculated at the minima.

This simulation study verifies the importance of the sensitivity analysis, in order to determine the correlations that may exist between the thermal properties, and thus to know the physical parameters that can be identified by the optimization.

3.6 Conclusion

In this chapter, we have studied the thermal transport for different types of materials using a spectral thermal sensor that combined the FDTR and TDTR experimental measurements.

First, with the One-Temperature Model, we showed the theoretical thermal response of the multilayer sample in the frequency domain. This study of the direct problem allowed the evaluation of the sensitivities of the model and the influence of the thermal properties on the response. We have seen that the dominant parameters in the thermal response are strongly dependent on the nature of the studied material and of course the frequency range of measurements. For that, the

sensitivity study was necessary to determine the parameters which can be identified, the parameters must be fixed and the existing correlations between certain quantities.

For experimental measurements, we have developed a spectral sensor allowing to obtain an ultimate bandwidth thermal response. This sensor combines the measurements of the FDTR and the TDTR methods and leads to investigate the thermal transport in materials in wide frequency range extending from 10 kHz to 1 THz. Using this approach allowed to observe all the thermal effects in the sample and enabled to enhance simultaneous thermal property characterization.

The performance of the sensor has been validated by characterizing the thermal properties of different materials. These studied samples represented a wide range of the thermal conductivity, the thickness, and the structure. In addition, for the conductor materials, the sensor wide response has allowed to identify simultaneously the thermal conductivity and the heat capacity. The identified values agreed with the theory and measurements listed in the literature.

Finally, we have presented an analysis of the identified parameters uncertainty by studying the impact of the experimental noise, the fixed parameters errors and the influence of determining the correlated parameters in the optimization. The study has shown that the high signal to noise ratio of the FDTR/TDTR sensor response leads to the identification of the thermal properties with low uncertainty. The highest error source on the estimated parameters comes from the ignorance of the fixed ones. By varying these parameters, we conclude that the properties of the aluminum transducer mainly influence the identified values.

Chapter 4

Spectroscopy of superdiffusive phonons in non-Fourier materials

Chapter 4 : Spectroscopy of superdiffusive phonons in non-Fourier materials

4.1 Introduction

Thin films have been extensively used in engineering systems to improve their optical, electrical, and thermal functionalities. When the thickness of a thin film becomes smaller than the mean free path of its heat carriers (electrons or phonons), the thermal properties of the film become significantly different from its bulk counterpart due to the geometric constraints. In this case, the energy transfer is known as an intermediate regime between the ballistic flight and purely diffusive regime, which can be described by the framework of Lévy Walks theory, i.e. the superdiffusive regime. This behavior is different from the conventional Brownian motion and is theoretically expected in different semiconductors. A detailed understanding of this superdiffusive thermal transport is crucial for many technological engineering applications including nano-electronic devices, heat management and thermoelectric materials. In this chapter we aim to use our ultra-broadband measurement, FDTR/TDTR spectral thermal sensor, as a new metrology to probe the ballistic-diffusive heat transfer in nanostructured semiconductors and then seek to verify the existence of this regime in artificial materials mixing alloy and nano-inclusions.

In the first part, we will describe the foundations of superdiffusive regime and its physical origin in alloys, then comes its numerical modeling. We will introduce a formalism based on the truncated Lévy statistics, allowing experimental analysis of quasi ballistic heat flow. Then, we will do a comparative study of the theoretical thermal response of this model with the purely diffusive 1TM, and show that the frequency range of the quasi-ballistic regime is accessible by the FDTR/TDTR thermal sensor. Next, the thermal characterization will be performed on the experimental measurements of semiconductors. We will show the validity of the truncated Levy model to describe the transition between the ballistic and diffusive regimes existing in InGaAs alloy. Then, we will study the thermal behavior of Ge-based model materials containing nano-inclusions that

are expected to scatter photons at a different length scale and enhance the ballistic-diffusive transition in the material medium.

The second part of this chapter will be dedicated to the preliminary study of the in-place diffusion analysis. We will begin by introducing a new optical system employed in the heterodyne TDTR allowing to probe the spatial heat distribution on the surface of materials. Second, we will propose a thermal method based on the spatial logarithmic processing of the temperature response for a semi-infinite layer. This model makes it possible to estimate the thermal properties in particular the diffusivity in the plane of heterogeneous and anisotropic mediums. Finally, we will show the experimental measurement and the characterization results of in-plane thermal diffusivities obtained for electrons and phonons in a gold film.

4.2 Superdiffusion heat conduction and Lévy processes

The high-resolution experimental systems based on femtosecond lasers or near field probes has highlighted new transport mechanisms and interactions demonstrating the failure of classical physical laws in nano-systems. One of the main reasons for this failure is the transition between ballistic and diffuse heat transfer systems. In the following, we give few examples of recent literatures showing a clear deviation from classical diffusive theory demonstrating the need for improved experimental characterization techniques and new ways of modelling.

4.2.1 Bird's eye view of non-Fourier transport

In 2006, Koh and Cahill reported an anomalous frequency dependence of the thermal conductivity in semiconductor alloys revealed by femtosecond laser Time-Domain Thermoreflectance experiments [84]. When a modulated heat source, created by a laser pulse, is oscillating above the MHz, the apparent thermal conductivity of alloys drops by more than 50% compared to its bulk value. **Figure 4-1** shows that this apparent frequency dependence appears solely in alloys while the apparent thermal conductivity remains constant in pure crystals (InP, GaAs...) and amorphous materials (SiO₂). The authors claimed that ballistic phonons, with a mean free path longer than the

thermal diffusion length of the heat source do not contribute to the measured thermal conductivity. However, their cumulative approach [85] is inherently biased because it maintains a diffusive-Fourier regime. This converts the used thermoreflectance experiment into a method that measures the mean free path spectrum of phonons [86-87].

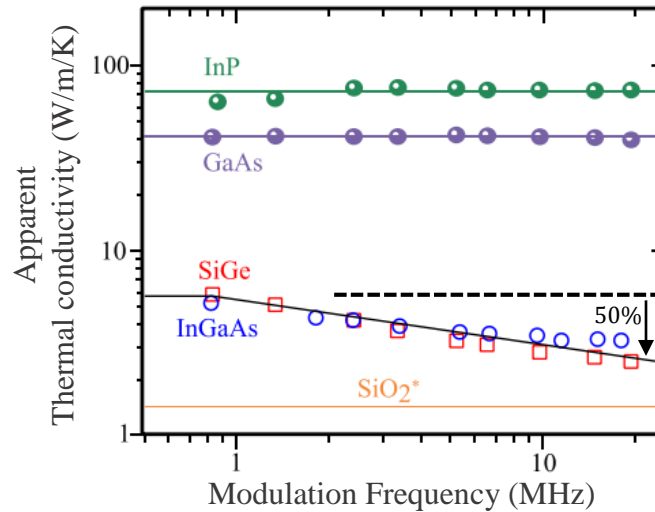


Figure 4-1: Apparent frequency dependence of the thermal conductivity in crystalline, alloy semiconductors and amorphous [84].

In 2010, Siemens *et al* [88] used a soft X-Ray TDTR experiment to observe deviation in Fourier predictions while varying the size of metallic heaters from 65 nm to 2 μm . Soft X-Ray features increased drastically the spatial resolution of their experiment and allowed the authors to observe a ballistic-diffusive transition. They tempered this effect by assuming an additional ballistic boundary resistance between the heater and their medium, but once again, their theoretical approach was Fourier based.

In 2014, Nelson and Minnich presented an experimental measurements with a Transient Thermal Grating (TTG) [89-90] and demonstrated a similar anomalous behavior of the thermal conductivity with a spatially modulated heat source [91]. The absorption of crossed laser pulses sets up a sinusoidal temperature profile that is monitored via the diffraction of a probe laser beam controlled by the temperature induced index grating. By changing the period of the thermal grating, the heat penetration length can be adjusted within the range from 1 to 10 μm . At small spatial periods

corresponding to high frequency excitation, a reduction in the apparent thermal conductivity can also be interpreted as a transition from the diffusive to the ballistic transport regime. This explained by considering that only phonons with mean free path less than the size of the source contribute to the thermal conductivity.

Indeed, the frequency dependence of the thermal conductivity observed by thermoreflectance occurs due to a bias appearing when a purely diffusive-Fourier model fails to take into account the transition diffusive-ballistic regime. In 2015, Vermeersch *et al* showed, using first-principle calculations and solving the Boltzmann transport equation [92], that a quasi-ballistic transition regime appears naturally in alloys. For that, they described a new model based on the Lévy dynamic which was a key parameter to apprehend ballistic-diffusive effects. In their work, Lévy dynamics [93] in alloys is called superdiffusion. The results revealed that the earlier mentioned reductions of apparent conductivity in semiconductor alloys are a direct manifestation of superdiffusive Lévy transport. Additionally, the formalism indicated that the transient temperature inside the material differs significantly from Fourier theory and brings improvement to thermal characterization of alloys and material interfaces. In the following, we will describe the origin and the principle of superdiffusion regime and its modeling.

4.2.2 Thermal transport regimes in alloys

In order to identify key regimes of thermal transport inside the semiconductor alloys, Vermeersch [92, 94–96] introduced analytical solutions of the Boltzmann transport equation using *ab initio* phonon dispersions and scattering rates. This investigation study led to the analysis of spatiotemporal dynamics of the thermal heat conduction in close detail and highlight the presence of an intermediate regime between the ballistic and diffusive regimes in alloys. **Figure 4-2** shows the transient evolution of the normalized mean square displacement of the thermal energy deposited by a single pulse.

In silicon, two well established regimes of thermal transport exist. The heat is progressively transferred from the purely ballistic regime ($\sigma^2 \sim t^2$) to the purely diffusive regime ($\sigma^2 \sim t$). In fact, a transit ballistic-diffusive regime exists in InGaAs and SiGe alloy materials. This thermal

transport generally qualified as a quasi-ballistic or superdiffusive ($\sigma^2 \sim t^\beta$, $1 < \beta < 2$) appears over a time range extending from picoseconds to few nanoseconds.

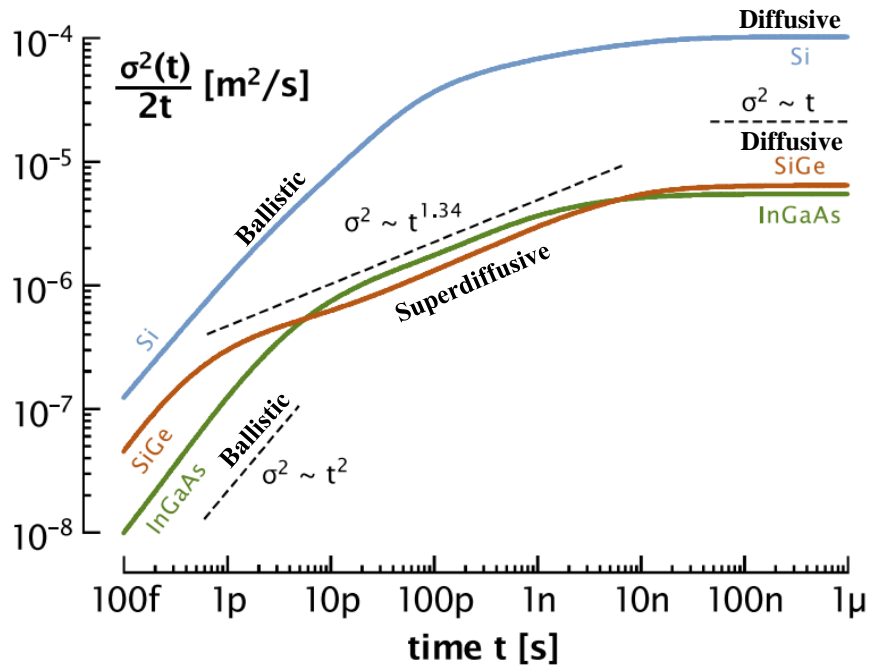


Figure 4-2: Normalized mean square displacement of thermal energy deposited by a single pulse as a function of time [92].

The superdiffusivity term was introduced by the mathematician Paul Lévy to describe the “heavy-tails” distribution of jumps experienced by a random walker [97]. Lévy behaviors are observed in several domains such as travel patterns of foraging animals, protein movements along a DNA chain, turbulence in fluids, pulsar scintillation, financial market fluctuations, etc [98]. Applied to phonon transport, the formalism of Lévy walks is based on a probabilistic framework where the random motion of phonons propagating inside a material is described in terms of a stochastic process (travel and scattering).

In order to show the difference between the superdiffusive and diffusive transport regimes, **Figure 4-3** shows an example of a phonon trajectory in each transport case.

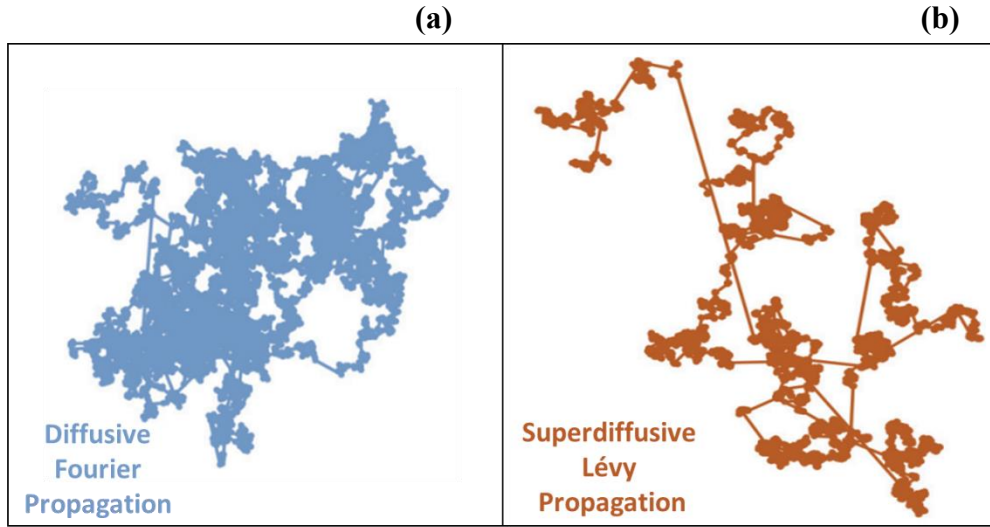


Figure 4-3 Example of a phonon trajectory subjected to a (a) purely diffusive Fourier motion and (b) Lévy superdiffusive motion [92].

The pure diffusive regime (**Figure 4-3 (a)**) is stochastically equivalent to a Brownian process in which the phonons travel along random trajectories. Therefore, the heat carriers follow a Gaussian distribution with a mean square displacement of $\sigma^2 \sim 2Dt$, where D is the diffusion coefficient. Its thermal energy density described by Fourier is expressed in the spatio-temporal domain in the following form:

$$\mathcal{P}_{Fourier}(r, t) \propto e^{-\frac{r^2}{4Dt}} \quad 4.52$$

Thus, in the Fourier-Laplace space, it is expressed as:

$$\mathcal{P}_{Fourier}(\xi, s) \propto \frac{1}{D\xi^2 + s} \quad 4.53$$

where ξ is the spatial Fourier variable (m^{-1}) and s is the Laplace variable (s^{-1}). The stochastic diffusion regime can be also characterized by the probability of phonon displacements. For this classic diffusion process, the probability of heat carriers making a jump length of u is given by:

$$\psi_{Fourier}(u) \propto |u|^{-3} \quad 4.54$$

On the other hand, in the superdiffusive regime (**Figure 4-3(b)**), considering entangled ballistic and diffusive processes, the distribution of mean-free path cannot be described by a Gaussian distribution, in which long “ballistic jump” are unlikely to happen. However, it can be mathematically apprehended by a “heavy-tail” distribution of possible jump length. In a Lévy flight, the steps of the random walk process have a power law distribution, meaning that extremely long jumps can occur. Consequently, the average step length diverges and the energy propagates faster than the normal diffusion.

A thermal transport in which the step length is governed by Lévy statistics, leads to superdiffusion, where the mean squared displacement increases faster than linearly with time $\sigma^2 \sim t^\beta$ and the thermal regime can be interpreted from phenomenological point of view by an energy density of this form:

$$\mathcal{P}_{Lévy}(\xi, s) \propto \frac{1}{D_\alpha \xi^\alpha + s} \quad 4.55$$

where $\alpha = 3 - \beta$ ($1 < \alpha < 2$) and D_α is a fractional diffusivity constant related to the classical diffusivity as $D_\alpha \propto D/l^{2-\alpha}$ (m^α/s), l can be interpreted as a characteristic length of the superdiffusive regime. The energy density corresponds to the characteristic function of Lévy process and immediately implies that the quasiballistic energy transport is stochastically equivalent to a random walk with fractal dimension α . The jump probability distribution associated with this Lévy dynamic is then simply written in the following form:

$$\psi_{Lévy}(u) \propto |u|^{-(1+\alpha)} \quad 4.56$$

with $\alpha=2$, and the distribution properties of Lévy process become identical to those of the diffusive Fourier regime. This inherent fractal distribution of pure Lévy dynamics maintains the quasiballistic regime indefinitely spatially, and therefore temporally. However, as we have seen

earlier in alloys, the thermal transport recovers to regular Fourier diffusion at sufficiently long length and time scales. For that, the jump probability distribution becomes:

$$\psi_{L\acute{e}vy}(u) \propto \frac{e^{\left(\frac{-|u|}{u_{BD}}\right)}}{|u|^{(1+\alpha)}} \quad 4.57$$

where $e^{\left(\frac{-|u|}{u_{BD}}\right)}$ is an exponential truncation to force the jump tail of $\psi_{L\acute{e}vy}(u)$ to drop equally or more steeply, in a way that Brownian dynamics can be recovered at sufficiently large distances. u_{BD} is then the characteristic length associated with the time scale t_{BD} over which the transition from quasiballistic to diffusive transport occurs. This leads to long jumps of Lévy dynamics only appearing at short scales ($t < t_{BD}$ or $u < u_{BD}$) and therefore limiting the spatial and temporal extent of the superdiffusive regime.

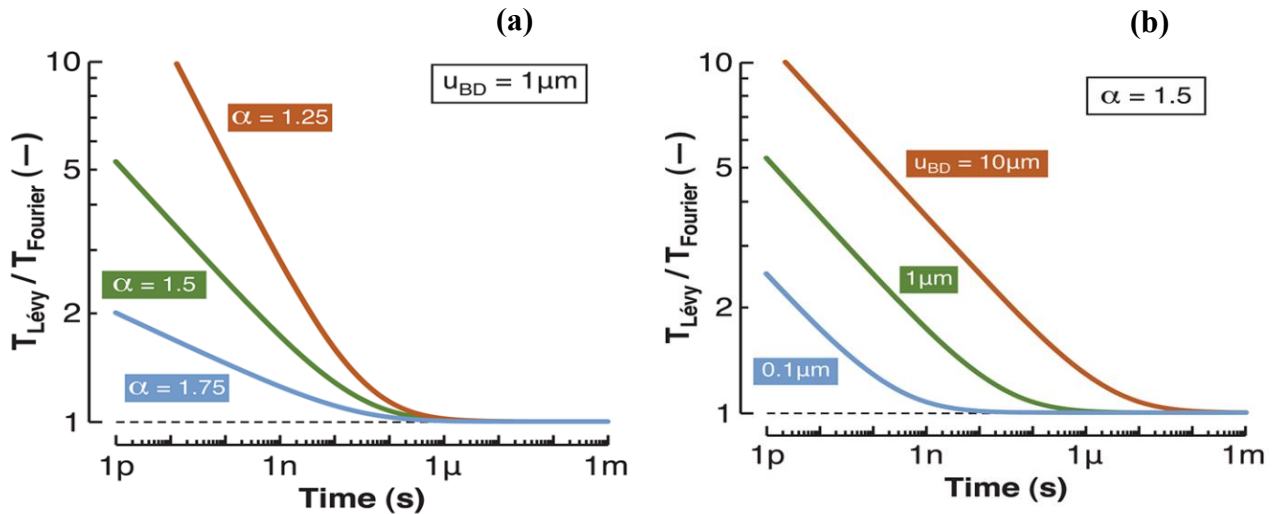


Figure 4-4: Temperature source response of truncated Levy model normalized by Fourier prediction. (a) Fractal dimension α controls the steepness of the initial transient. (b) Characteristic length u_{BD} regulates the transition in space and time from pure Lévy superdiffusion to regular Fourier diffusion [99].

Figure 4-4 [99] illustrates clearly the effect of the two Lévy parameters, which are α and u_{BD} , on the thermal response generated by a Dirac pulse of energy (space and time) in a semi-infinite

medium. The fractal dimension α induces initial temperature transients that significantly exceed Fourier predictions, but also drop more steeply. Meanwhile, u_{BD} controls the length and associated time scales t_{BD} after which the expected temperature response is identical for both Lévy and Fourier models.

It should be noted that as we have seen, the time of appearance of the superdiffusive regime depends on the studied material. In this chapter, we are interested in the thermal behavior of semiconductor alloys (**Figure 4-2**), in which the intermediate regime occurs in the first picoseconds following the excitation and gives way to the diffusive regime after tens of nanoseconds. Thus, the corresponding frequency range extends from GHz to about MHz, which is accessible by the FDTR/TDTR ultra wide band sensor.

4.2.3 Origin of the superdiffusive Lévy regime

The phonon scattering mechanism in solids is a key issue to understand the thermal conduction and the processes of energetic material. In this context, the literature study [92] showed that the quasi-ballistic dynamics existing in alloys originated in its dominant phonon scattering mechanism.

The phonon-scattering mechanism is generally described by the time approximation τ :

$$\tau(\omega) \propto \omega^{-n} \tag{4.58}$$

where ω is the phonon frequency and n is an integer qualifying the type of the scattering processes existing in the material. The exponent $n = 2$ describes the normal diffusion processes, for which the phonon wave vector is conserved ($\mathbf{k}_1 + \mathbf{k}_2 = \mathbf{k}_3$); $n = 3$ describes the Umklapp processes, which changes the phonon momentum ($\mathbf{k}_1 + \mathbf{k}_2 = \mathbf{k}_3 + \mathbf{G}$); and $n = 4$ corresponds to the relaxation process at high order, such as the Rayleigh scattering that happens in alloys (Mass-impurity diffusion).

The study of the phonon-scattering mechanism in silicon showed that the normal and Umklapp processes dominate its bulk thermal conductivity at ambient temperature [100-101]. This is illustrated in **Figure 4-5**, which presents the relaxation time of phonons as a function of their frequency obtained from *ab initio* dispersion calculations.

The results show that scattering rates of Si can be fitted with a scattering relation $\tau(\omega) \propto \omega^{-3}$, which is a characteristic of the Umklapp processes. The upper portions of the cumulative conductivity curve ($k_{\Sigma}(\tau)$) show a clear logarithmic dependence on the scattering time, as predicted by the ideal $n = 3$ case.

Similar study was performed for InGaAs and SiGe alloys, shows that the Rayleigh scattering dominant their thermal behavior. **Figure 4-6** presents the data result of phonon relaxation for InGaAs layer.

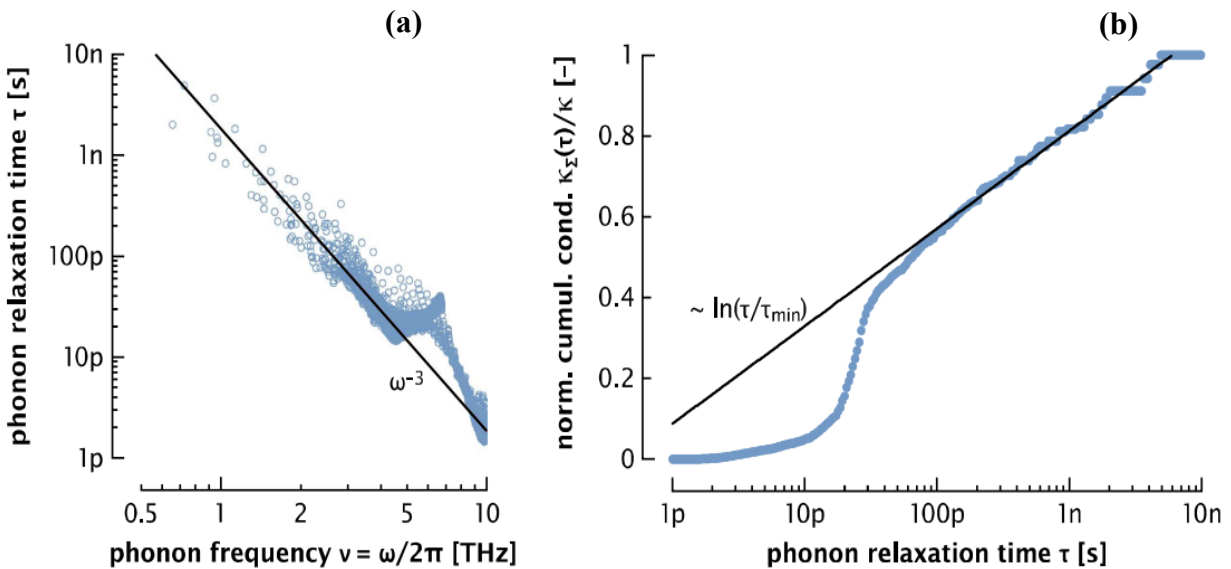


Figure 4-5: *ab initio* results of (a) relaxation times of phonons as a function of their frequency in Si, and (b) the accumulated thermal conductivity as a function of phonon relaxation time in Si [92].

The relaxation time of InGaAs in respect with about $\tau(\omega) \propto \omega^{-4}$, which has been attributed to the Rayleigh scattering by the authors. In addition, the relaxation time range over which $k_{\Sigma}(\tau)$ closely follows a power law corresponds to the superdiffusive time window in the mean square

displacement $\sigma^2 \sim t^\beta$ observed previously (see **Figure 4-2**). Consequently, the appearance of the superdiffusive regime is due to the presence of higher order relaxation mechanisms, such as the present Rayleigh scattering in alloys.

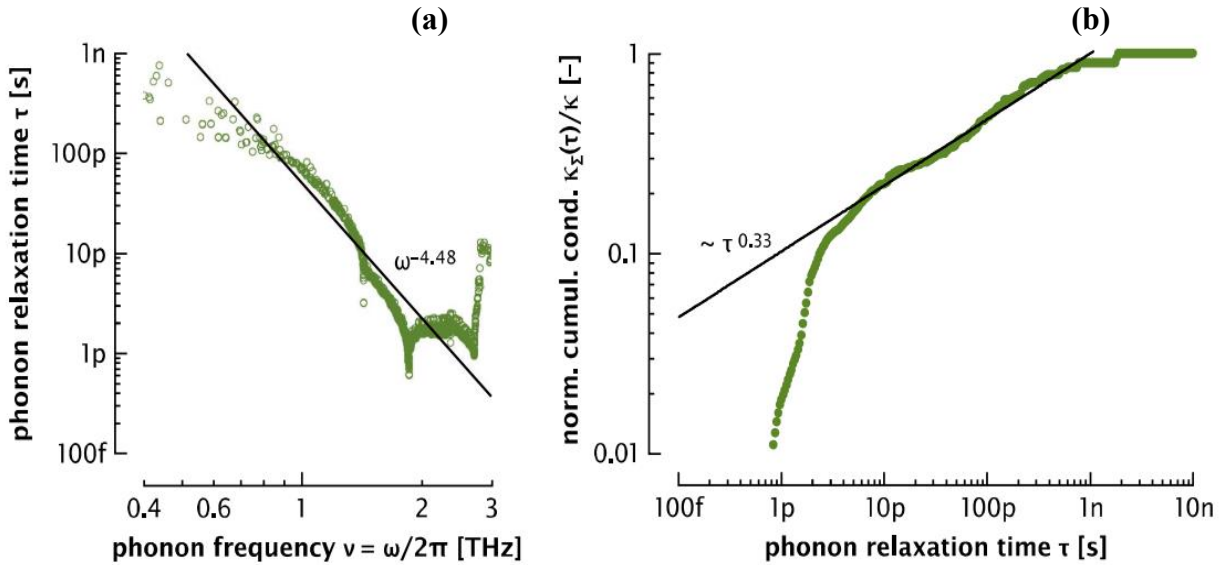


Figure 4-6: *ab initio* results of (a) Relaxation times of phonons as a function of their frequency in InGaAs alloy. (b) Accumulated thermal conductivity as a function of phonon relaxation time in InGaAs alloy [92].

The characterization of the thermal properties of alloys requires a thermal model considering the superdiffusive regime. By using a purely diffusive model, the interpretation leads to an identified thermal conductivity that depends on the excitation frequency. This dependence disappears by using a thermal model based on truncated Lévy dynamics, which proved itself as a better alternative to characterize alloys thermal properties [102]. In the following, we will show our thermal model based on Lévy dynamics used to study and characterize the thermal properties of semi-conductors alloys.

4.3 Modeling the truncated Lévy distribution

For modeling the quasiballistic heat flow, we adopted the three-dimensional Lévy approach described by Vermeersch [102]. In this section, we will present the implementation of this model and express the surface temperature of a sample subjected to a transient heat flux by an optical pulse. The key point of the method is based on the equivalence between the temperature response $T(x, t)$ to an energy impulse and the probability $\mathcal{P}(x, t)$ to find a random heat carrier in position x and at time t . This equivalence relation is:

$$T(x, t) = \frac{\mathcal{P}(x, t)}{\rho C} \quad 4.59$$

4.3.1 Implementation of the superdiffusion model

The motion of thermal energy in semiconductors can be described as a series of transition events. Each transition moves spatially the energy carriers by a distance u randomly chosen from the distribution probability $\psi_u(u)$, while the time between consecutive transitions is governed by a distribution $\psi_t(t)$. The latter is considered as a time Poissonian process $\psi_t(t) = \nu e^{-\nu t}$, where ν is the jump frequency. By supposing that $\psi_u(u)$ and $\psi_t(t)$ are stochastically independent, the mathematical description of the process can be simplified. In this case, the single pulse energy density for a given jump length, time distributions can be write in Fourier-time domain by [103]:

$$\ln \mathcal{P}_{Lévy}(\xi, t) = -\nu t \int_{-\infty}^{+\infty} (1 - e^{-j\xi u}) \psi_u(u) du \quad 4.60$$

With the truncated Lévy jump length distribution $\psi(u)$, described earlier in equation (4.57), the energy density can be evaluated analytically. We obtain, after integration, the following expression of the 1D energy density:

$$\ln \mathcal{P}_{1D-Lévy}(\xi, t) = (-2t) \frac{\xi_{BD}^2 D}{\alpha(1-\alpha)} \times \left[\left(\left(\frac{\xi}{\xi_{BD}} \right)^2 + 1 \right)^{\alpha/2} \cos \left(\alpha \arctan \left(\frac{\xi_{BD}}{|\xi|} \right) - \frac{\alpha\pi}{2} \right) - 1 \right] \quad 4.61$$

where $\xi_{BD} = \frac{1}{u_{BD}}$.

When $\alpha = 2$, this distribution becomes identical to that of the Fourier regime, for whatever value of ξ_{BD} , as shown in this equation:

$$\ln \mathcal{P}_{1D-Lévy}(\xi, t) = -D\xi^2 t \quad 4.62$$

By applying a numerical Fourier inversion of equation 4.61, we can obtain the 1D energy density in the real spatial domain $\mathcal{P}(x, t)_{Lévy-1D}$. Then, the temperature in 3 dimensions can be calculated based on isotropy and symmetry of revolution of the heat flow. The single pulse temperature response for a semi-infinite medium becomes:

$$T_{Lévy-3D}(r, t) = \frac{2}{\rho C} \mathcal{P}(x = r/\sqrt{3}, t)_{Lévy-1D}^3 \quad 4.63$$

with r the distance from the source.

Finally, we apply to this calculated temperature the formalism of the thermal quadrupoles (described in chapter 1) as shown the modeling in **Figure 4-7**. This allows to obtain the

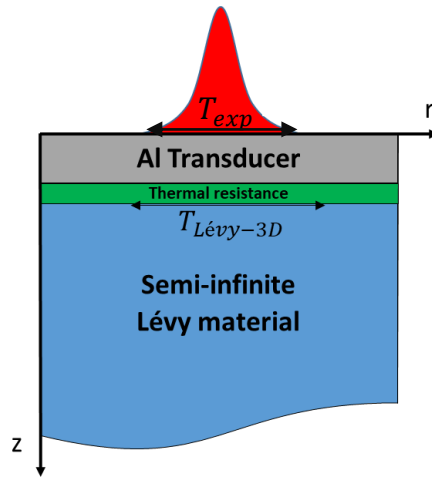


Figure 4-7: Modeling of applying the thermal quadrupole method on a semi-infinite Lévy material.

temperature at the transducer surface, which make the thermal model able to analyze the thermoreflectance experimental measurements and to extract the desired thermal properties.

4.3.2 Comparative study with the response of diffusive 1TM

After the implementation of the Lévy model, a comparative study of its thermal response with that of the 1TM (Fourier) can be carried out to show the difference between them. In this part, we assumed for simplicity that the transducer is instantaneously thermalized in both models in order to focus on the material of interest. **Figure 4-8** shows the amplitude and spectral phase of the thermal response calculated with the 1TM and truncated Lévy models of a semi-infinite substrate topped with a 70 nm aluminum transducer.

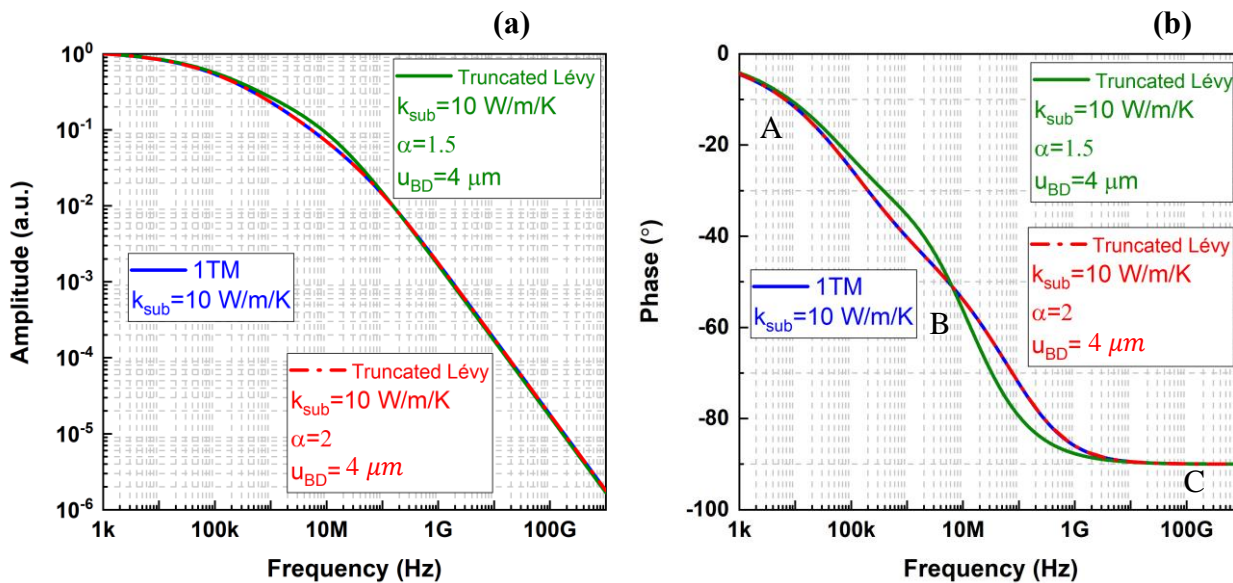


Figure 4-8: Spectral response in (a) amplitude and (b) phase calculated with the Fourier 1TM and truncated Lévy models of a semi-infinite substrate with a 70nm aluminum transducer.

We can see that the Lévy model with $\alpha = 2$ becomes a regular Fourier model providing the same spectral response to that calculated by the 1TM. However, when the exponent $\alpha = 1.5$, the Lévy model behaves differently than the 1TM considering quasi-ballistic effects. This difference can be

seen especially in the phase response, which exhibits more sensitivity to the non-Fourier transport, via the time of flight, than to the amplitude signal.

In the phase response (**Figure 4-8(b)**), the 1TM and truncated Lévy ($\alpha = 1.5$) models behave identically at high frequency, in which the thermal response is sensitive to the transducer. As the transducer is being considered as instantaneously thermalized, the phase of the spectral response tends towards -90° at high frequency (region C). On the other hand, at low frequencies, the phase of the two models response tends towards 0° due to the semi-infinite medium (region A). The differences in the rest of the frequency range is due to the superdiffusive regime (region B). Therefore, the range of this thermal regime is accessible by the thermoreflectance Spectral Sensor FDTR/TDTR and the characterization should be performed on the phase response.

The difference between the 1TM (Fourier) and Lévy models can be discriminated also from the spatial response. **Figure 4-9** presents the surface temperature response maps calculated by the two models, where two major differences can be seen from these calculations at short times. The first reveals that the superdiffusive model predicts that the energy propagates further away from the point source capturing the effect of phonons with long mean-free path. The second effect appears close to the source where the temperature of the hot spot is much higher than the one predicted by the diffusive theory.

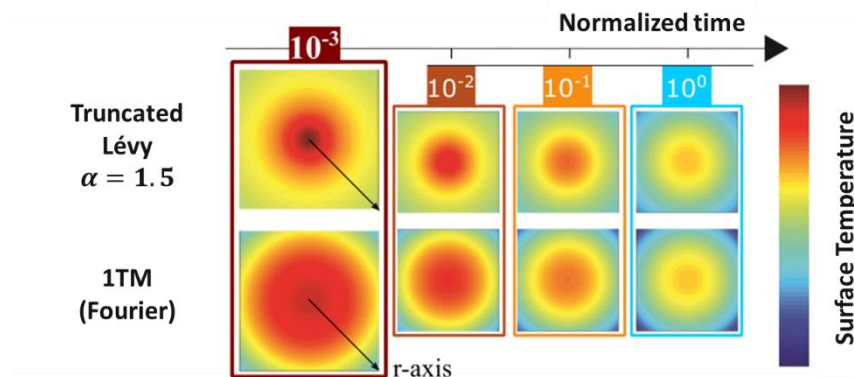


Figure 4-9 Maps of surface thermal response calculated for a Lévy model and 1TM at different times normalized to the characteristic Lévy time t_{BD} [102].

4.4 Experimental study and analysis out of plane diffusion

In this section, we studied the expected superdiffusive behavior in nanostructured materials; InGaAs alloy and GeMn crystal. The investigation of this quasi-ballistic thermal behavior was carried out by the several steps:

In the beginning, we measured the phase spectral response of the studied sample by the thermal sensor FDTR/TDTR. In a second step, we applied two optimizations on the experimental response to describe the thermal response. The first optimization is with the purely diffusive 1TM and the second one is with the truncated Lévy model. If the studied material is a Fourier sample and not exhibiting a superdiffusive behavior, the two temperature models, 1TM and truncated Lévy, must converge and identify identical thermal properties, which should agree with the literature. On the other hand, for non-Fourier samples, in which a superdiffusive regime is exist, the 1TM is not able to correctly describe the spectral phase response and thus can not identify consistent values.

4.4.1 InGaAs

The first studied sample is $\text{In}_{0.53}\text{Ga}_{0.47}\text{As}$ alloy, in which a frequency dependence of the thermal conductivity is present according to literature, evidence of the presence of a marked ballistic-diffusive transition. Here, we will show the capacity of the FDTR/TDTR sensor to detect this superdiffusive regime and the capability of the truncated Lévy model to describe it.

4.4.1.1 Sample description

The structure of the sample consists of a 2000 nm thick InGaAs layer, deposited on an InP substrate, and with a 70 nm aluminum transducer deposited on top of it. **Figure 4-10** shows the multilayer structure of this sample with thermal properties essential for its modeling, the known values taken from the literature [104]. The size of lasers (pump and probe) and the properties of the aluminum transducer are fixed at the same values as those used in chapter 2. The thermal

resistance $R_{\text{InGaAs/InP}}$ is fixed at $1 \text{ nK}\cdot\text{m}^2/\text{W}$. The value of this thermal resistance has no significant effect due to the low sensitivity of the response to it.

The 1TM optimization is performed with two free parameters, which are the thermal conductivity of InGaAs (k_{InGaAs}) and the thermal resistance between the Al transducer and InGaAs layer ($R_{\text{Al/InGaAs}}$).

For the truncated Lévy model, which describes the heat in a semi-infinite medium topped by a transducer, the InGaAs layer is considered as a substrate. In addition to the thermal conductivity of InGaAs (k_{InGaAs}) and the thermal resistance ($R_{\text{Al/InGaAs}}$), the optimization with this thermal model enables the identification of two other parameters, which are the superdiffusive exponent (α) and the characteristic transition length (u_{BD}).

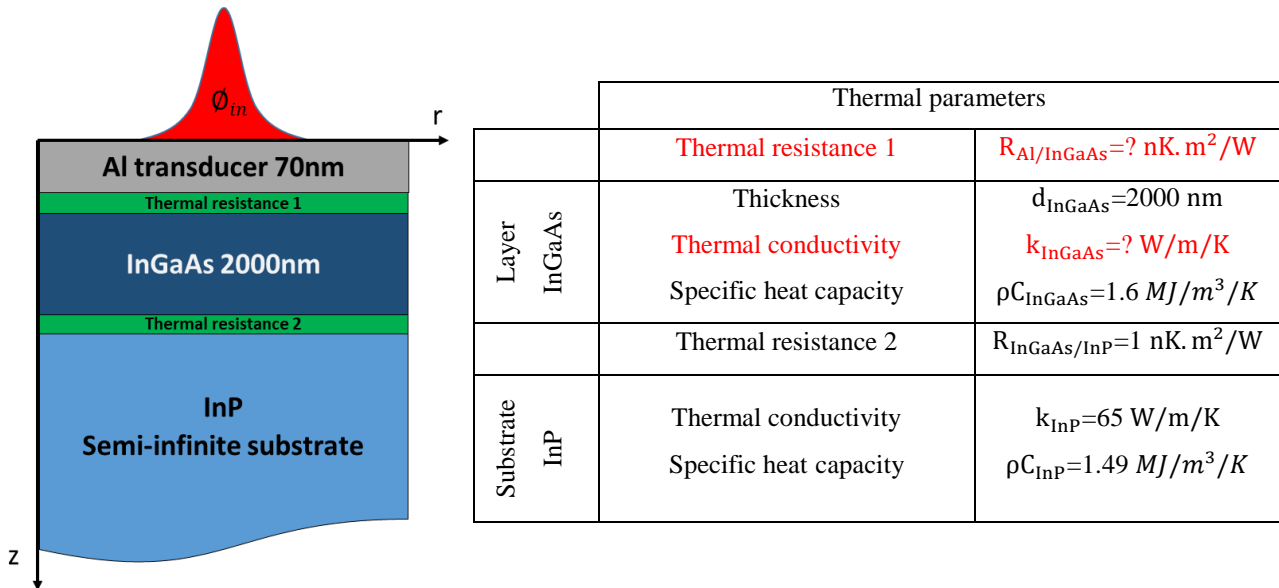


Figure 4-10: Schematic description of the Al/InGaAs/InP sample with thermal properties used for the modeling.

4.4.1.2 Results and discussion

Figure 4-11 shows the measured spectral phase response of Al/InGaAs/InP sample, on which two optimizations are performed, one with the classic 1TM and the other with the truncated Lévy model. We immediately observe the inability of the 1TM model to describe the entire frequency response of the sample. The purely diffusive model does not fit the experimental response, particularly in a frequency range extending from 200 kHz to 200 MHz. However, the model fitting is adequate at high frequencies (200 MHz to 10 GHz) where the thermal response is sensitive to the Al transducer effect. This is also the case at low frequencies (up to 200 kHz) where the response is sensitive to the InP substrate thermal effect. Therefore, the disagreement only exists in the range where the response is sensitive to the InGaAs layer. The identified parameters by this 1TM optimization are 3.4 W/m/K for the k_{InGaAs} and 11.8 nK.m²/K for the $R_{Al/InGaAs}$. The thermal

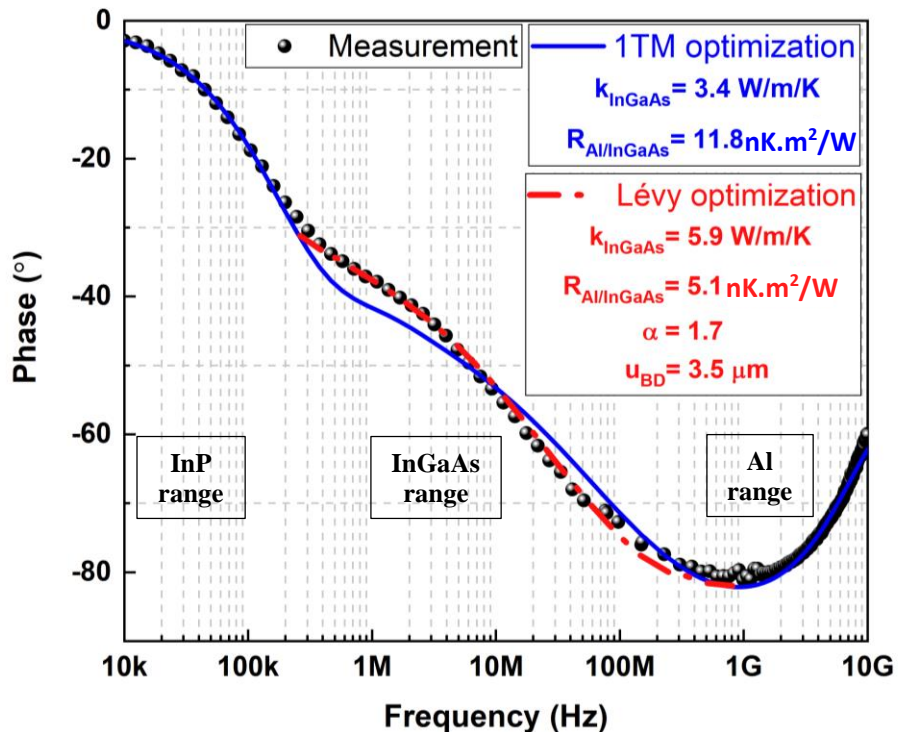


Figure 4-11: Spectral phase of the thermal response measured for Al/In_{0.53}Ga_{0.47}As/InP sample. In black the experimental response, in blue the theoretical one adjusted by the 1TM, and in red the theoretical one adjusted by the truncated Lévy model.

conductivity is 50% lower than the expected value while the thermal resistance is 50% higher than what is found in literature.

On the same figure (**Figure 4-11**), the optimization performed by the semi-infinite Lévy model is also presented. On the contrary of the 1TM, the truncated Lévy provides an accurate fit to the thermal response above the frequency 200 kHz. This means that the model was able to describe the thermal behavior of InGaAs. The best optimization is obtained with the values of 1.7 for α , 3.5 μm for u_{BD} , 5.9 W/m/K for k_{InGaAs} and 5.1 nK.m²/K for $R_{Al/InGaAs}$. These identified values are in perfect agreement with the theory and measurements found in [44, 92].

Consequently, the failure of the purely diffusive 1TM to describe the thermal response is an agreement with the theoretical simulation of Vermeersch, presented earlier in this chapter, predicting the existence of the superdiffusive regime in InGaAs alloy. Besides, the result confirms and validates the capacity of truncated Lévy model to characterize this ballistic-diffusive transition regime in the non-Fourier material.

4.4.2 GeMn

The second studied sample is an innovative nano-inclusions embedded semi-conductor GeMn, consisting of a crystalline germanium matrix with embedded crystalline spherical manganese nano-inclusions. We will show the effect of nano-inclusions on the thermal behavior of the sample, which is expected to exhibit a superdiffusive regime. Then, we will present the fabrication process of this state-of-the art material and the experimental results of the thermal investigation obtained by the TDTR/FDTR spectral sensor.

4.4.2.1 Expected effect of Mn nano-inclusions

Based on literature, bulk crystalline materials are not suitable for the occurrence of the ballistic-diffusive behavior and nano-structuration is mandatory. To do so, nano-inclusions will be incorporated to crystalline layers. By modifying the crystalline phases and the size distribution of

nano-inclusions, the phonon mean free path can be adjusted at different scales to enhance the expected superdiffusion.

Numerous studies report significant changes in transport properties by incorporating nano-inclusions into a semiconductor matrix. For superdiffusive heat transfer, measurements of the superdiffusive exponent in InGaAs material containing various concentrations of ErAs nano-inclusions have been reported by Mohammed and Koh in 2015 [99]. They observed a reduction of the superdiffusive exponent $\alpha_{\text{InGaAs:ErAs}} \sim 1.55$ regarding the host alloy without inclusions $\alpha_{\text{InGaAs}} \sim 1.7$ shown in the previous section. This reduction proves that the presence of nano-inclusions slightly enhances the superdiffusive process. They also observed a quasi-constant value of α regarding the different concentrations in ErAs nanoparticles. These results are explained by the narrow size distribution of inclusions that only scatters a limited range of phonons.

In 2008, Barthelemy et al [98] engineered a “Lévy glass for light” by incorporating TiO₂ microspheres into a glass matrix. By doing so, they modified the distribution of “jumps” between consecutive scattering events and reported a superdiffusive Lévy transfer. Even if subtle differences exist between the “Lévy Flights” for light addressed by Barthelemy and the “Lévy Walks” for thermal phonons that we study in this work, these results show the possibility to engineer phonon transport and enhance superdiffusive effects by nanostructuring.

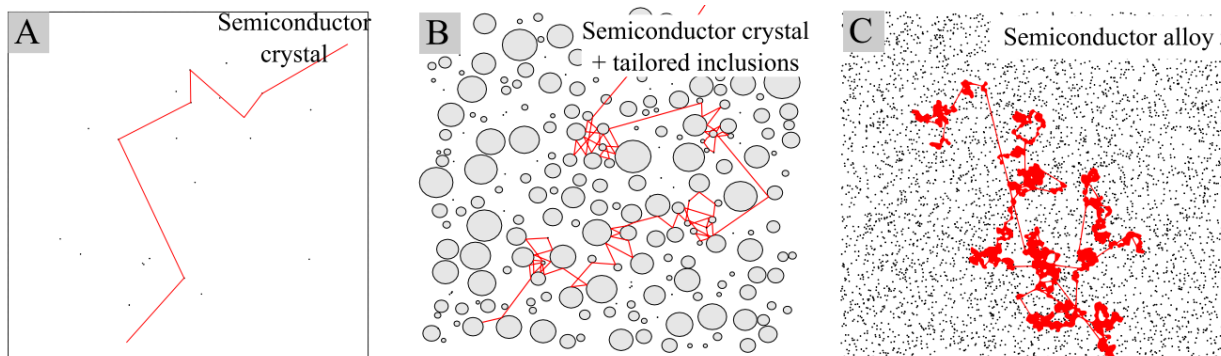


Figure 4-12: Schematic of heat transfer regimes at short times (10 ps-10 ns) in model materials. (A) Natural semiconductor crystal (few isotopic impurities) with no ballistic-diffusive transition. (B) Expected ballistic-diffusive transition in a pure crystal with a tailored distribution of nano-inclusions. (C) Natural semiconductor alloy exhibiting a ballistic-diffusive transition described by a superdiffusive Lévy model.

In this context, the produced crystalline semi-conductors Ge with embedded crystalline nano-inclusions Mn are model materials, since nano-inclusions are expected to increase phonon scattering depending on their sizes and distribution as shown in **Figure 4-12**. This key feature of Ge-based nanostructuration is expected to strongly alter heat transfer by inducing scattering of a wider population of phonons than those reported in the literature. In this work, we will verify experimentally the existence, or not, of the superdiffusive regime in the model material GeMn.

4.4.2.2 Fabrication process

The growth of the GeMn films have been performed in the research group at Néel institute in Grenoble, by the team of O. Bourgeois [105–107]. The epitaxial growth of GeMn films was performed using ultra-high vacuum Molecular beam epitaxy (MBE) deposition technique. The fabrication process of these films can be divided into several steps describe in the following.

First, the GeMn films were grown on commercially available Ge (001) wafers. This Ge substrate underwent a chemical and thermal treatment in order to remove the contamination and the oxidation layer present on its top surface. After this treatment, a 27 nm thick Ge buffer layer is deposited on the Ge substrate followed by a quick annealing, allowing the epitaxial growth of GeMn film on an atomically flat surface. The substrate is then transferred to the MBE chamber equipped with standard effusion cells that permit the growth of the film via the co-deposition of Ge and Mn. This is performed at a temperature region around 100 °C that is expected to enhance the Mn solubility in Ge and also minimize the phase separation. The film thickness is well controlled because of the slow growth rate of 1.3 nm/min. The co-deposition leads to the formation of auto-organized nano-columns embedded in the crystalline germanium matrix as a result of spinodal decomposition.

In order to transform the nano-columns into a more stable state GeMn spherical nano-inclusions in Ge matrix, the film is annealed after growth over a certain time period to reach high temperature (450-500 °C), leading to the formation of randomly distributed Ge_3Mn_5 nano-inclusions in a Mn doped crystalline germanium matrix. TEM micrographs showing the transition from columnar to nano-clusters in the film are presented in **Figure 4-13** [108].

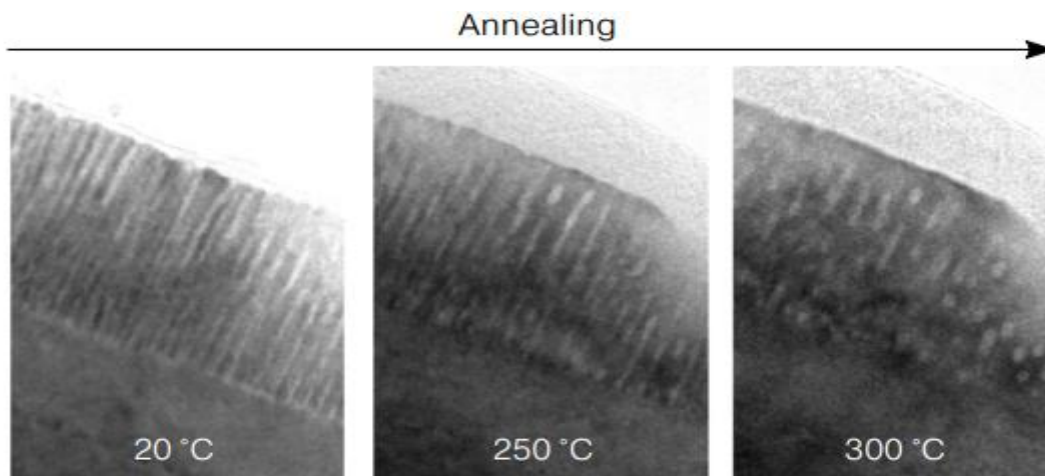


Figure 4-13: TEM images of the transformation process of nano-columns GeMn to spherical nano-inclusions in the germanium matrix by annealing [108].

Prior to the annealing step, the GeMn films are capped with an 80 nm germanium layer to avoid the surface roughness possibly occurring due to the migration of manganese upon annealing. Therefore, this extra thin germanium layer makes the surface smoother, which allows in final step the deposition of aluminum transducer on top of it for the thermoreflectance measurements. It should be noted that the quality of the crystalline nature of the films is periodically observed by in-situ reflection-high-energy-diffraction (RHEED) equipped within the MBE chamber.

In the growth process, the size distribution of the Ge_3Mn_5 nano-inclusions can be tuned by controlling the amount of manganese introduced during the growth and the annealing temperature. This is shown in **Figure 4-14**, where the size distribution of the nano-inclusions is tailored by the Mn concentration (from 8% to 14%) and the annealing temperature. The well-controlled nano-inclusions size distribution and concentration is important to tune phonon transport and efficiently scatter a broad portion of the entire phonon spectrum as we have seen earlier. In this work, this model materials will be used to study the influence of disorder on the appearance of superdiffusive regime at a 10 nm scale.

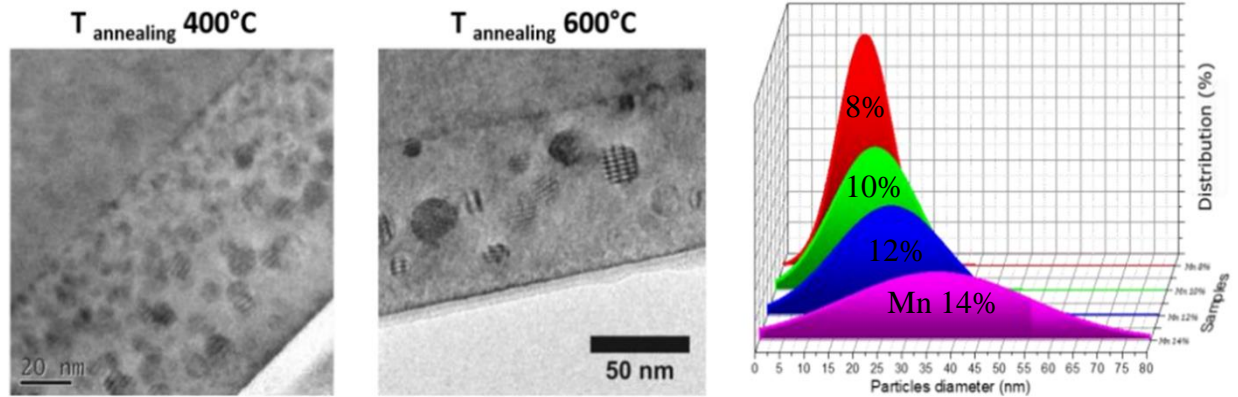


Figure 4-14: TEM side view of GeMn thin film annealed at a) 400°C and b) 600°C. c) Size distribution of nano-inclusions deduced from TEM observation in GeMn thin films annealed at 700°C and containing different concentration of Mn [106].

4.4.2.3 Sample modeling

We have studied two types of GeMn layers for several thicknesses, the first one containing 8% of manganese ($\text{Ge}_{0.92}\text{Mn}_{0.08}$) and the other one 10% ($\text{Ge}_{0.90}\text{Mn}_{0.10}$). The schematic structure of the multi-layers system that has been grown is shown in **Figure 4-15**.

We have considered the germanium capping layer to be part of the GeMn film in the thermal models (1TM, truncated Lévy) instead of an extra layer. The reason for this is due to the immigration of the manganese during the annealing, since the thickness of the capping layer is of the order of the inter-inclusion distance. For the modeling, the thermal properties of the substrate Ge and the transducer Al are supposed to be known. The thermal resistance $R_{\text{GeMn}/\text{Ge}}$ between the GeMn layer and the Ge substrate is fixed at $1 \text{ nK}\cdot\text{m}^2/\text{W}$.

In the 1TM optimization, two thermal parameters are left free: k_{GeMn} and $R_{\text{Al}/\text{GeMn}}$. On the other hand, the Lévy model optimization collectively identifies k_{GeMn} , $R_{\text{Al}/\text{GeMn}}$ and the two quasiballistic parameters α and u_{BD} . It should be noted that the GeMn layer is considered as a semi-infinite substrate in the truncated Lévy model.

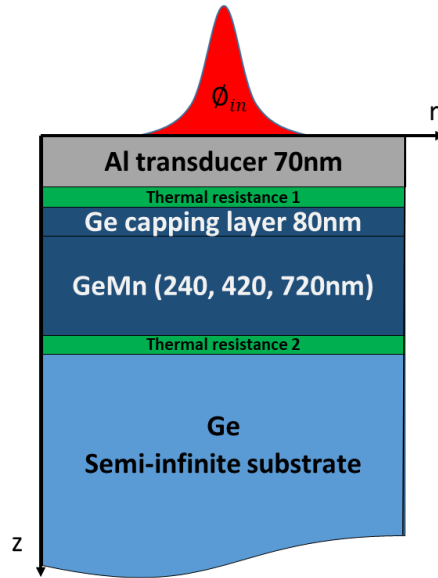


Figure 4-15: Schematic of the studied multilayer system of GeMn.

4.4.2.4 Results and discussion

Figure 4-16 shows the result of optimizations performed by the 1TM and the truncated Lévy model on the measured spectral response for the case of 420 nm thick $\text{Ge}_{0.92}\text{Mn}_{0.08}$ layer.

We can see that the 1TM has successfully described the thermal response over all the frequency measurements. The best optimization is obtained with $k_{\text{GeMn}} = 15.9 \text{ W/m/K}$ and $R_{\text{GeMn/Ge}} = 13 \text{ nK.m}^2/\text{W}$. Moreover, the truncated Lévy model fits the spectral response in the GeMn frequency range (above 10 MHz) and converges to $\alpha = 2$ for the exponent characterizing the superdiffusion dimension. In this case $\alpha = 2$, indicating purely diffusive dynamics, the transition length u_{BD} is no longer meaningful and its value is therefore not significant. For the identified thermal parameters, the optimization of truncated Lévy model is obtained with $k_{\text{GeMn}} = 15.9 \text{ W/m/K}$ and $R_{\text{GeMn/Ge}} = 13.1 \text{ nK.m}^2/\text{W}$, which are extremely close to those estimated with the 1TM. Indeed, the identified value of the thermal conductivity by the two thermal models is in agreement with literature [109], in which the measurement was performed by a SthM method.

For thermal studies, to observe the diffusion of carriers, it is necessary to be able to observe a sufficient number of them. For this, we performed another measurement with a larger laser to

validate the previous result. To do that, we have replaced the microscope objective 10X by a 5X. The sizes of the pump and the probe measured by the profiler beam now become $9 \mu\text{m}$ and $6 \mu\text{m}$, respectively.

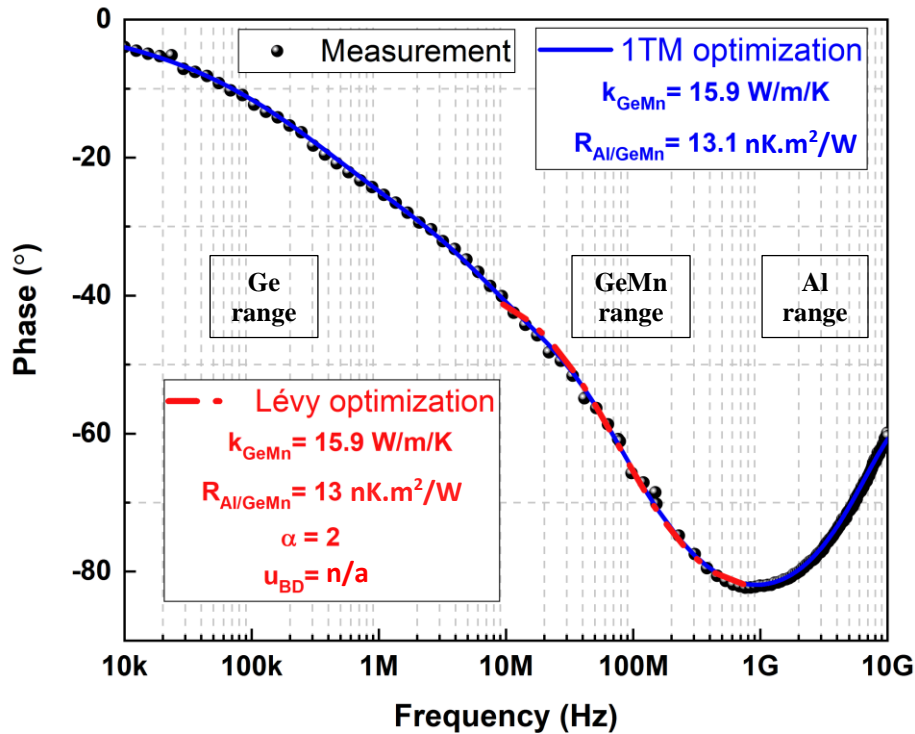


Figure 4-16: Optimizations on the thermal phase response (in black) measured with a 10X microscopic objective of Al/Ge_{0.92}Mn_{0.08}/InP sample. In blue the 1TM theoretical response, and in red the truncated Lévy model theoretical response.

We have carried out the measurement for the same sample of 420 nm thick Ge_{0.92}Mn_{0.08} layer. The experimental phase response with two optimizations applied by the 1TM and the truncated Lévy model are presented in **Figure 4-17**.

Same as the previous measurement, the result shows that the 1TM matches very well the experimental response. Besides, the Lévy model fits the response above 100 MHz and converges to the exponent $\alpha = 2$. This clearly indicates the absence of the ballistic-diffusive transition in the Ge_{0.92}Mn_{0.08} studied layer. Both thermal models identified the same values, namely 16.3 W/m/K for

thermal conductivity k_{GeMn} and $13.2 \text{ nK.m}^2/\text{W}$ for the thermal resistance $R_{\text{GeMn/Ge}}$. These values are very similar to those obtained with the microscope objective X10.

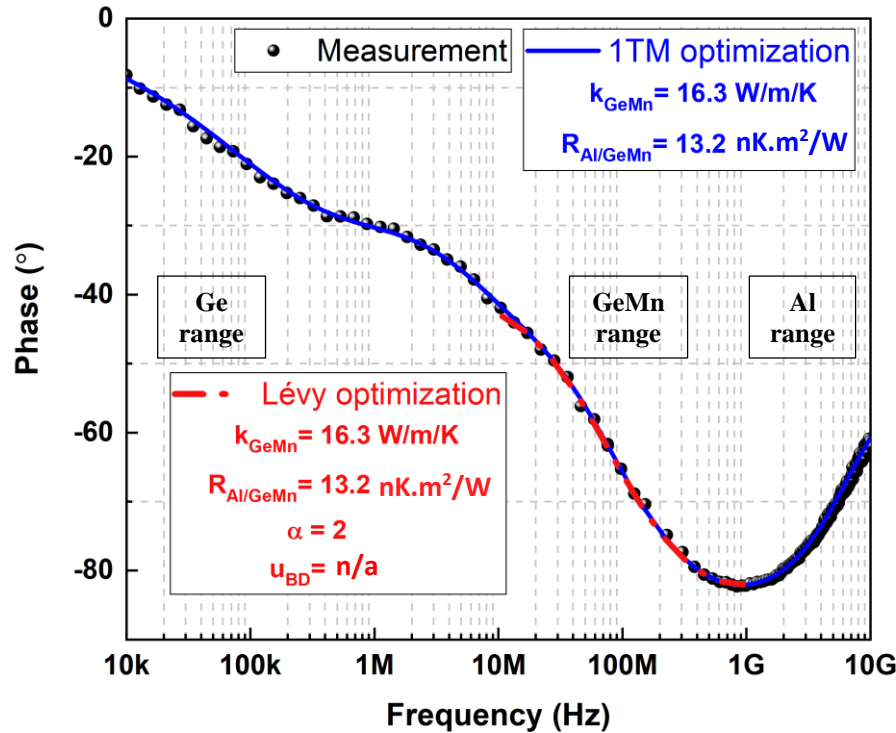


Figure 4-17: Optimizations on the thermal phase response measured with 5X microscopic objective of Al/Ge_{0.92}Mn_{0.08}/InP sample. In black the experimental response, in blue the 1TM theoretical one, and in red the truncated Lévy model theoretical response.

The identical convergence and identification of 1TM and truncated Lévy model clearly indicates the absence of the ballistic-diffusive transition in the Ge_{0.92}Mn_{0.08} layer. This is also the case for the Ge_{0.90}Mn_{0.10} layer, where the two thermal models converge to the same thermal values. The average of the identified thermal properties of Ge_{0.92}Mn_{0.08} and Ge_{0.90}Mn_{0.10} for several thicknesses are given by the **Table 4-1**.

Layer Thickness	Ge _{0.92} Mn _{0.08} (8% of Mn)	Ge _{0.90} Mn _{0.10} (10% of Mn)
240 nm	$k_{GeMn}=16.2$ W/m/K $R_{GeMn/Ge} = 13.3$ nK.m ² /W	$k_{GeMn}=13.7$ W/m/K $R_{GeMn/Ge} = 13$ nK.m ² /W
420 nm	$k_{GeMn}=15.9$ W/m/K $R_{GeMn/Ge} = 13$ nK.m ² /W	$k_{GeMn}=14$ W/m/K $R_{GeMn/Ge} = 12.8$ nK.m ² /W
720 nm	$k_{GeMn}=15.8$ W/m/K $R_{GeMn/Ge} = 13.6$ nK.m ² /W	$k_{GeMn}=13.8$ W/m/K $R_{GeMn/Ge} = 13$ nK.m ² /W

Table 4-1: Identified thermal properties for different thicknesses of Ge_{0.92}Mn_{0.08} and Ge_{0.90}Mn_{0.10}.

We can see the effect of the manganese concentration, where the identified thermal conductivity in the different studied thicknesses, changes from 16.2 W/m/K for Ge_{0.92}Mn_{0.08} to 14 W/m.K for Ge_{0.90}Mn_{0.10}. This variation can be explained by the fact that increasing the concentration of nano-inclusions, the phonon scattering increases and thus reducing the lattice thermal conductivity. However, the superdiffusive regime did not exist in the different studied samples. This thermal investigation also underlines the repeatability of the experiment since we obtained similar results with different thicknesses.

The thermal characterization of Mn-doped crystalline germanium matrix GeMn, shows the effect of inclusions concentration, and that is by inducing scattering of thermal phonons and thus decreasing the thermal conductivity. However, the introduced nano-inclusions were not able to enhance a ballistic-diffusive transition as expected. The thermal investigation by the two thermal models, 1TM and truncated Lévy, indicates the purely diffusive dynamic of the heat transport in the model material GeMn. This can be due to the small size distribution of Mn inclusions, which was not able to improve a sufficient superdiffusive regime that can be detected by the measurement.

4.4.3 Conclusion

In the first part of this chapter, we have studied the energy transfer in nanostructured semiconductors that exhibit a superdiffusive regime at specific space-times scales.

First, we have shown that the classic Fourier model considering only the diffusion, failed to describe the quasi-ballistic regime observed in the materials in the form of an apparent frequency dependence of the thermal conductivity. We have then introduced the truncated Levy formalism, which captures all essential physics of transition between quasiballistic and regular diffusive transport contained. The final equation obtained can be used to interpret the thermal response for a semi-infinite medium subjected to a transient surface heat flux. The study of this model shows that the quasi-ballistic effects typically appear at time scales accessible by the spectral thermal sensor FDTR/TDTR.

We have then presented the experimental study of InGaAs semi-conductor alloy. The obtained result verified the presence of quasi-ballistic effects in InGaAs, previously observed by other methods. This thermal investigation validated the capability of the truncated Lévy model to describe the ballistic-diffusive regime.

Finally, we have studied the thermal behavior of Mn-doped crystalline germanium matrix GeMn. The 1TM (Fourier) was able to describe correctly the full spectrum of studied GeMn samples, proving the diffusive nature of the transfer and thus the absence of a superdiffusive regime, in this model material. However, the thermal characterization has shown that the thermal conductivity of the layer was affected by the concentration and the distribution of nano-inclusions, which increase the phonon scattering in the material.

4.5 Heat transfer dynamics imaging for in-plane diffusion analysis

Advances in instrumentations of thermoreflectance methods allow direct spatio-temporal measurement of the surface response of materials following the laser excitation. After having shown the determination of through-plane thermal properties, we will now look at the in-plane properties. This provides a more complete study of thermal behaviors in materials. The preliminary

work presented in this second part of the chapter will be a preparation to a later investigation of the spatial distribution of the superdiffusive regime in alloys and find out how it propagates in-plane.

First, we will introduce a new optical system employed in the heterodyne TDTR allowing to probe the spatial heat distribution on the surface of materials. We will show the capacity of this system, which takes advantage of the femtosecond pump-probe technique and provides the thermal measuring of heat carriers with high spatio-temporal resolution. Second, we will propose a thermal method based on the spatial logarithmic processing of the temperature response for a semi-infinite layer. This model makes it possible to estimate the thermal properties in particular the diffusivity in the plane of heterogeneous and anisotropic mediums. Finally, we will show the experimental measurement and the characterization results of in-plane thermal diffusivities obtained for electrons and phonons in a gold film.

4.5.1 TDTR scanning system

In order to obtain the spatial information on the thermal heat transport, we use an optical imaging system implemented in the heterodyne TDTR bench. This latter allows to change the position of the probe beam arriving on the sample and scan the targeted surface. The detection of the reflected probe beam is synchronized with the scanner motion in order to obtain the signal for each position (pixel). In this way, we can obtain a map of the reflectivity variations and thus the temperature distribution in the sample plane.

In our case, the imaging system consists of a focal lens mounted on a dynamic two-axis motor. A motion controller (MM4006) is connected with the motor to produce the precise displacement (horizontally or vertically) and the characteristic speed of the components. The lens movements are generated by electrical signals sent by the controller. The variation along the chosen axis is directly proportional to the voltage of the signal.

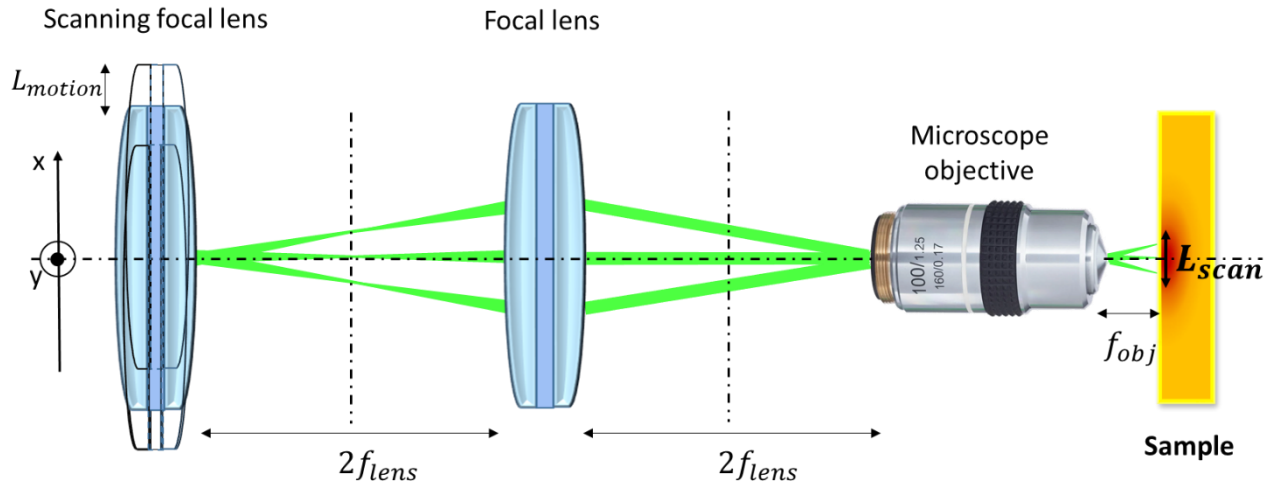


Figure 4-18: Schematic representation of the optical imaging system

The scanning optical lens is coupled with another focal lens and the microscope objective. The purpose of this combination of lenses is to combine the position of the scanner with the entrance pupil of the objective. The beam will therefore always be focused on the image focal plane of the objective whatever its angle of incidence. A schematic of the scanning system used is presented in **Figure 4-18**.

For each particular displacement L_{motion} , set for the motion lens, and a particular microscope objective, corresponds to a precise length L_{scan} scanned by the beam in the sample plane. The length L_{scan} along one of the axes (x or y) can be obtained by the following relation:

$$L_{scan} = L_{motion} \frac{f_{obj}}{f_{lens}} \quad 4.64$$

where f_{lens} is the focal length of the motion lens and f_{obj} is the focal length of the used objective. As an example, for a microscope objective 100X with $f_{obj}=1.8$ mm and a focal lens with $f_{lens}=200$ mm, setting a displacement of $L_{motion}=1000 \mu m$, the length of scan on the sample surface is $L_{scan} = 9 \mu m$.

4.5.2 Measurement and acquisition process

During the measurement, the pump is held fixed at a specific position on the sample while the probe is scanned over the field of view to provide a spatial map of the reflectivity. For each scanned position (pixel), we are able to perform the point measurement and record the time response of the reflectivity variation. This measurement in both time and space leads to produce a thermoreflectance movie describing the entire process of hot electron excitation and their consequent relaxation to phonons. With the movie, we are able to study the surface thermal distribution at any particular time following the excitation. **Figure 4-19** shows an example of a thermal map obtained 2 ps after of the pump excitation on a gold film surface.

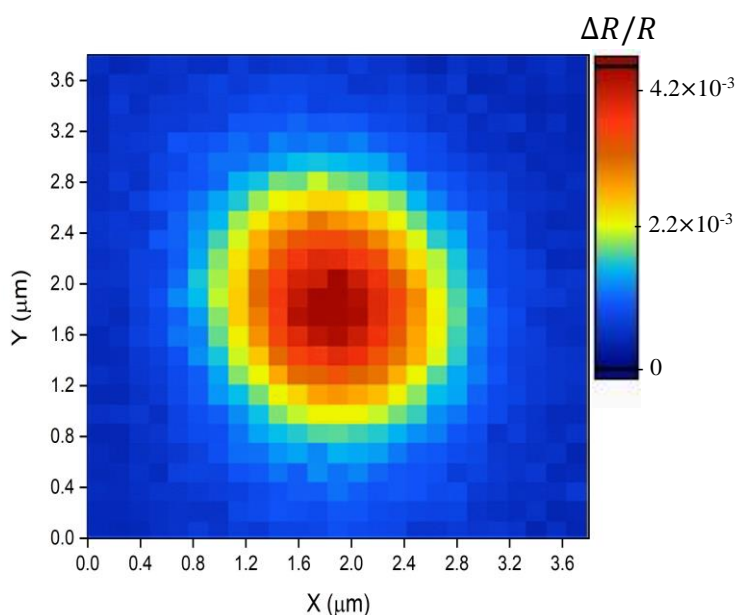


Figure 4-19: A thermal map acquired at 2 ps after the excitation for Au film with 808 nm and 532 nm for the pump and the probe respectively.

The measurement performed with the 100X microscope objective enabled to scan the surface with $3.7 \mu\text{m}$ length in both x and y directions. In addition, the mapping response is measured with a high spatial resolution of up to 130 nm and sub-picosecond time resolution. For this, the TDTR

heat imaging is characterized by high spatiotemporal resolution allowing to examine and investigate the in-plane thermal properties of ultrafast heat carriers, electrons and phonons.

4.6 In-plane thermal properties identification

4.6.1 Parabolic method

In order to characterize the in-plane thermal properties, we use a spatial logarithmic approach, which called the thermal parabolic method. This approach allows to estimate the thermal diffusivity, the location and size of the heating spot on the surface. For the modeling, we consider that the studied sample is a homogeneous and anisotropic semi-infinite medium, subjected to a thermal excitation by an impulse with Gaussian distribution in space and Dirac in time. Under these conditions, the front face analytical expression of the temperature response field is written as follows [50, 109-110]:

$$T^*(x, y, z = 0, t) = \frac{E}{\rho C} \frac{\exp\left(-\frac{(x - x_0)^2}{\frac{r_p^2}{2} + 4D_x t}\right) \exp\left(-\frac{(y - y_0)^2}{\frac{r_p^2}{2} + 4D_y t}\right)}{\sqrt{\frac{r_p^2}{2} + \pi D_x t} \sqrt{\frac{r_p^2}{2} + \pi D_y t} \sqrt{\pi D_z t}} \quad 4.65$$

where x_0 and y_0 are the spatial coordinates (m) of the laser spot on the surface; D_x , D_y and D_z represent the thermal diffusivities (m^2/s) according to the x, y, and z direction axis; E is the energy of the pulse laser source (J); r_p is the pump spot radius (m) and ρC corresponds to the specific heat capacity of the medium ($\text{J}/\text{m}^3/\text{K}$).

To reduce this three-dimensional equation to a two-dimensional scattering one, the expression is divided by its average calculated in the plane (along the x and y directions). This division allows to obtain the following transient thermal response:

$$\begin{aligned}
 T(x, y, z = 0, t) &= \frac{T^*(x, y, z = 0, t)}{\langle T^*(x, y, z = 0, t) \rangle_{x,y}} \\
 \frac{T^*(x, y, z = 0, t)}{\langle T^*(x, y, z = 0, t) \rangle_{x,y}} &= \frac{\exp\left(-\frac{(x-x_0)^2}{\frac{r_p^2}{2} + 4D_x t}\right) \exp\left(-\frac{(y-y_0)^2}{\frac{r_p^2}{2} + 4D_y t}\right)}{\sqrt{\frac{r_p^2}{2} + \pi D_x t} \sqrt{\frac{r_p^2}{2} + \pi D_y t}}
 \end{aligned} \quad 4.66$$

where,

$$\langle T^*(x, y, z = 0, t) \rangle_{x,y} = \frac{E}{\rho C} \frac{1}{\sqrt{\pi D_z t}} \quad 4.67$$

Due to the separability properties of the method, it is possible to study the different one-dimensional transient temperature fields. To do this, a marginal average is calculated according to each of the x ($\langle T(x, y, z = 0, t) \rangle_x$) and y ($\langle T(x, y, z = 0, t) \rangle_y$) directions, which yields to a 1D transient temperature distribution. By taking the spatial logarithm these averages, the following expressions are obtained:

$$\begin{aligned}
 \ln(\langle T(x, y, z = 0, t) \rangle_x) &\approx \ln(k_1) - \ln(t) - \frac{(y-y_0)^2}{\frac{r_p^2}{2} + 4D_y t} \\
 \ln(\langle T(x, y, z = 0, t) \rangle_y) &\approx \ln(k_2) - \ln(t) - \frac{(x-x_0)^2}{\frac{r_p^2}{2} + 4D_x t}
 \end{aligned} \quad 4.68$$

where k_1 and k_2 are constants. These expressions can be assimilated to a polynomial relation of order 2:

$$\begin{aligned}
 \ln(\langle T(x, y, z = 0, t) \rangle_x) &\approx \beta_{0_y}(t) + \beta_{1_y}(t)y + \beta_{2_y}(t)y^2 \\
 \ln(\langle T(x, y, z = 0, t) \rangle_y) &\approx \beta_{0_x}(t) + \beta_{1_x}(t)x + \beta_{2_x}(t)x^2
 \end{aligned} \quad 4.69$$

Hence, the different coefficients are given by:

$$\begin{aligned}
 \beta_{2x,y}(t) &= -\frac{1}{\frac{r_p^2}{2} + 4D_{x,y}t} \\
 \beta_{1x,y}(t) &= \frac{x_0, y_0}{\frac{r_p^2}{4} + 2D_{x,y}t} \\
 \beta_{0x,y}(t) &= -\frac{x_0^2, y_0^2}{\frac{r_p^2}{2} + 4D_{x,y}t} + C_{1,2}
 \end{aligned} \tag{4.70}$$

From these coefficients, the following thermal properties can be estimated:

- The radius of the pump r_p is obtained at the y-intercept of the coefficient $\beta_{2x,y}^{-1}$ plotted as a function of time.
- The diffusivities $D_{x,y}$ can then be estimated independently according to x and y directions by the slope of the coefficient $\beta_{2x,y}^{-1}$ as a function of time.
- The pump spot position x_0 and y_0 could be conducted with the direct relation between $\beta_1(t)$ and $\beta_2(t)$:

$$\beta_{1x}(t) = -2\beta_{2x}(t)x_0 \text{ or } \beta_{1y}(t) = -2\beta_{2y}(t)y_0 \tag{4.71}$$

4.6.2 Hotspot imaging in homogenous gold film

To validate the parabolic method proposed in this work, we will show the characterization results of in-plane thermal properties obtained from the measurement of TDTR thermal imaging for a gold film.

4.6.2.1 Hotspot mapping measurement

An experimental thermal mapping study is carried out on a homogeneous gold film. The sample structure consists of a 140 nm thick Au film deposited on a semi-infinite silica substrate. The measurement is performed with pump and probe wavelengths of 800 nm and 532 nm respectively. By using the imaging system of focal lenses, the probe beam scans the sample surface with an area of $3.8 \mu\text{m} \times 3.8 \mu\text{m}$ and records the response of the reflectivity variation in each position (30x30 pixels). The result obtained of the hotspot imaging as well as the spatial Gaussian fitting at different times of pump-probe delay is shown in **Figure 4-20**.

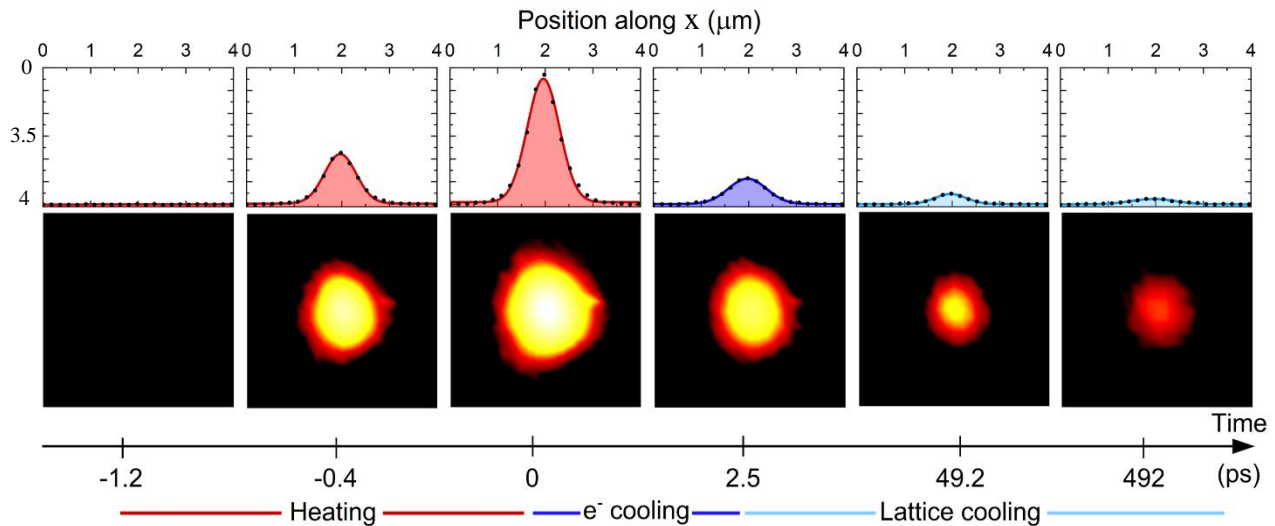


Figure 4-20: TDTR measurements of thermal heat mapping for a gold film at different pump-probe time delays as well as the spatial fitting performed in the x direction.

We can observe the evolution of the thermal spot following the pump excitation. The thermal images at different times describe the entire process of electrons and phonons dynamics. Moreover, by taking into account the isotropic properties of the sample, we also notice that the surface thermal distribution takes the form of a Gaussian profile at all times, characteristic of a homogeneous diffusion in all the directions of space.

Due to the semi-infinite characteristic of the model, the parabolic method has to be performed at short time scales where the heat propagation occurs in the Au film and does not reach the substrate,

which will affect the thermal properties on the surface. For this, we will study in the following the in-plane properties of electrons in a time range (0.5 ps to 2.5 ps) and for phonons (20 ps to 100 s). At these time scales, the heat carriers are always in the gold film.

4.6.2.2 Estimation of in-plane thermal diffusivity

In order to obtain the in-plane thermal properties, the marginal averages are carried out relative to the x and y directions on the thermal mapping measurement. This allows to optimize the area where the parabolic fit of equation 4.69 can be performed and estimate the coefficients of the second order polynomial for each time step for both directions.

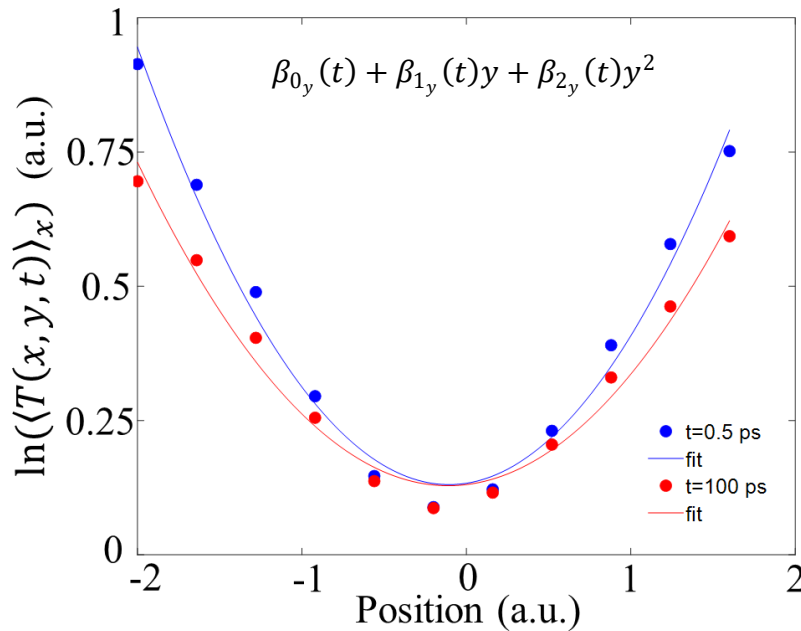


Figure 4-21: Logarithm of the marginal average of the temperature field along the x direction and the resulting fit for $t = 0.5$ ps and $t = 100$ ps.

By doing the marginal average along the x axis, we can obtain the transient temperature distribution in the y axis $\langle T(x, y, z = 0, t) \rangle_x$. Then, the parabolic fit was applied for each time step. **Figure 4-21** shows the fitting at two different times following the excitation, 0.5 ps and 100 ps.

From this, the parabola coefficient $\beta_{2y}(t)$ can be obtained for each time step. Calculating this coefficient as a function of time allow us to extract the desired in-plane thermal parameters according to expressions in equation 4.70 For that, we performed the calculation of $\beta_{2y}(t)$ in the time range extending from 0.5 ps up to 100 ps. For the short time range [0.5, 2.5] ps, we can estimate the thermal diffusivity of electrons (see **Figure 4-20**). For the longer time range [20, 100] ps, we can estimate the thermal diffusivity of phonons. **Figure 4-22** shows the inverse of the parabolic coefficient $\beta_{2y}(t)$ plotted as a function of time as well as the two fittings performed at short and long time ranges to estimate the thermal properties. Here, the fitting slopes correspond to the thermal diffusivities (see equation 4.70).

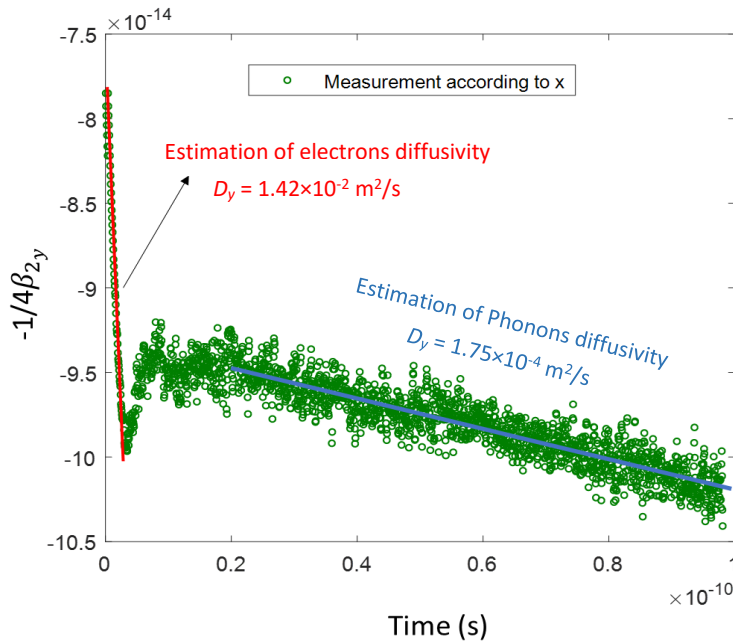


Figure 4-22: Inverse of the parabolic coefficient β_{2y} estimated along the direction x . Linear fit was applied at short time range [0.5, 2.5] ps to estimate in-plane thermal diffusivities of electrons, and at longer time range [20, 100] ps to estimate those of phonons.

Similarly, we performed the same analysis along the y axis to obtain the thermal properties in the x direction. **Table 4-2** presents the identified thermal diffusivities of electrons and phonons as well

as the estimated radius of the heat source, both along the x and y directions. It should be noted that the radius is estimated in both directions from the y-intercept of the fit at long time scales.

	x direction	y direction
Electrons diffusivity (m ² /s)	1.42×10^{-2}	1.45×10^{-2}
Phonons diffusivity (m ² /s)	1.75×10^{-4}	1.70×10^{-4}
Laser pump radius (μm)	0.96	0.90

Table 4-2: Estimated values of in-plane thermal diffusivities of electrons and phonons as well as the laser pump radius by the parabolic method along the x and y directions for the gold film.

The diffusivity values in two directions are very similar, confirming the isotropy of the material, and are in agreement with the literature [112]. In addition, the estimated size of the laser is very close to the expected value with the used objective 100X.

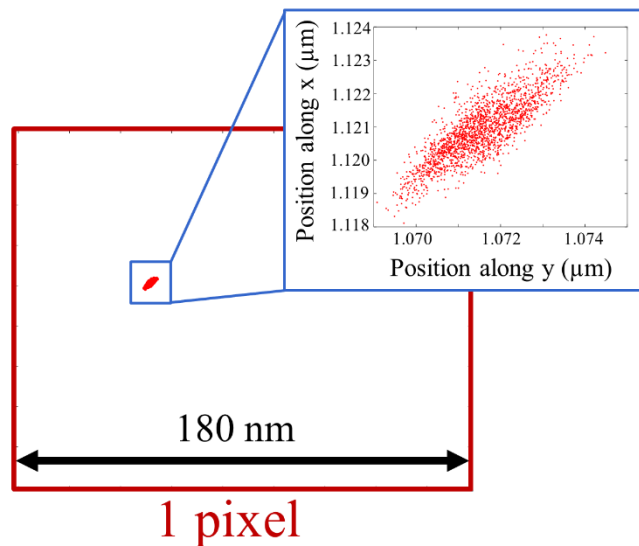


Figure 4-23: Estimated laser spot position obtained over the acquisition time on the surface of the film gold.

Finally, the spatial position of the thermal source is estimated according to the direct relation between the parabola coefficients; $\beta_{2,x,y}(t)$ and $\beta_{1,x,y}(t)$ (see equation 4.71). **Figure 4-23** presents the source position extracted over the acquisition time. We can see the accuracy of the estimated position compared to the pixel size, indicating the stability of the laser spot on the surface during the measurement thanks to the TDTR heterodyne sampling.

This study of in-plane measurement on an isotropic material such as the gold film makes it possible to validate the parabolic method since the diffusivities estimated for electrons and phonons along x and y are almost identical and are in agreement with the literature.

4.7 Conclusion and perspective

The second part of this chapter was devoted to the study of the spatial thermal characterization at the materials surface.

For that, we have shown an imaging system employed in the TDTR method, which enables to do the thermal mapping measurement with high spatio-temporal resolution. To estimate the thermal properties, we have introduced the parabolic method, which is based on a transient 3D analytical model of the impulse response. This analytical solution has the advantage of being separable, which makes it possible to study the heat transfers independently of the direction considered. By using the spatial logarithmic method, it becomes possible to estimate both the in-plane thermal diffusivities, the location and the size of the heating spot. The efficiency of the TDTR imaging method and the capability of the parabolic model were validated by the thermal characterization of an isotropic gold film. We were able to estimate the in-plane thermal diffusivities of both electrons and phonons in two directions of the heat propagation.

The study presented in this chapter concerns the preliminary step for spatial analysis of the heat transfer in alloys, in which the superdiffusive regime exists. The perspectives considered for this work can be classified into two aspects developed in parallel: the experimental TDTR method and the analytical model.

For the experimental aspect, we will develop a modulated heterodyne TDTR method for thermal mapping. The superdiffusive regime appears in alloys, as we have seen in chapter 4, at frequency range from hundreds of kHz up to hundreds of MHz. In order to reach the frequencies in this range and study the spatial propagation of non-diffusive transport, a modulation of the pump beam is necessary. Using dedicated modulation of femtosecond laser excitations; we will provide a complete description to the spatial distribution of the superdiffusive regime as a function of frequency. For that, the installation of the instruments required to perform the mapping measurement at different modulation frequencies is almost finished. However, a development of a Labview program for the setup is in progress. This program allows to automate the measurement as much as possible and to control all devices parts of the thermal imaging system.

For the theoretical aspect, we will extend the thermal parabolic method, which is valid for a semi-infinite layer, to thin films. This extension of the model will allow to take into account the non-diffusive thermal effect of the alloys layer deposited below the transducer. Therefore, the parabolic method becomes capable to estimate the thermal diffusivities in depth for a multilayer structure.

Conclusion

Conclusion

The work of this thesis focused on the study of the ultrafast heat transport in materials, especially the superdiffusive regime existing in semiconductor alloys. This was a part of the SPiDER-man ANR project, which aims to fill evident lacks in experimental solutions and knowledge of ballistic-diffusive heat transfer. The project brought together three complementary areas of expertise : the experimental measurements by the team of Stefan DILHAIRE at LOMA; the growth of materials by the team of Olivier BOURGEOIS at Néel institute; and the theoretical modeling with Gilles PERNOT at LEMTA.

Our part of the work consisted in designing a new instrumentation called spectral thermal sensor to probe the superdiffusive phonon transport. This sensor combined the measurements of two thermoreflectance methods, the TDTR heterodyne and the FDTR.

Thus, the first chapter was devoted to the thermal characterization of nanomaterials from the measurement of pump-probe thermoreflectance methods. The optical sampling of these techniques can be performed in different ways. In our work, we used a method called asynchronous, where the delay was performed using two femtosecond laser cavities with different repetition rate of frequencies. This technique allowed transient temperature measurements from hundreds of femtoseconds up to tens of nanoseconds. In addition to the superior speed acquisition of this sampling method compared to the synchronous one, the absence of a mechanical delay stage was also a considerable advantage as it eliminated many artifacts related to mechanical vibrations. Another thermoreflectance method resolved in frequency was also used in our work. In this configuration, the pump and the probe were generated by two continuous wave lasers. The response sampling of this method depended on the frequency modulation of the pump laser. After the description of the experimental techniques, we have introduced the 2TM, which made it possible to understand the impulse response of a metal. This model was used in the chapter 2 to study and describe the evolution of both phonon and electron temperatures in the studied medium during a femtosecond thermoreflectance experiment. We have also presented the classical 1TM, which is an asymptotic limit at long time scale of the 2TM when the heat carriers are in thermal equilibrium. We have solved this Fourier model in cylindrical coordinate for multilayer system by

applying a thermal quadrupole method. Solving the heat diffusion equation in Laplace-Hankel space allowed to describe the temperature response on the system surface. At the end of the chapter, we presented an example of 1TM thermal identification performed on the FDTR spectral response for a SiO₂ and Ge samples.

In the second chapter, we studied the effect of transducer on the spectral response of the heterodyne TDTR method. The ultimate bandwidth of the corresponding spectral material response that expands from 76 MHz up to 10 THz was limited by the presence of the metal transducer deposited on top of the material of interest. In order to determine the optimal transducer, we investigated the thermal transparency of several metal thin films. For that, we implemented and solved numerically the 2TM to describe the dynamics of both phonon and electron temperatures. This was performed for a set of Al, Au, Ag, Cu, Cr, and Pt thin layers. The numerical study showed that the Al thin film was better suited for spectroscopic lattice temperature measurements exhibiting a frequency bandwidth extending from 76 MHz up to 10 GHz. On the other hand, the Au gold film was the best for hot carrier electrons dynamics allowing the measurement from 1 GHz up to 5 THz. The experimental result showed a very good agreement between the thermal behavior of the Au spectral response predicted by the 2TM simulation study and the TDTR thermoreflectance curve.

The third chapter was devoted to the investigation and characterization of thermal properties of different types of materials through an ultra-broadband spectroscopy. We presented a spectral sensor combining the measurement of the FDTR and TDTR methods. The overlap allowed to probe a wide spectral response over 8 decades extending from 10 kHz up to 1 THz. We showed the ability of this sensor by identifying the thermal properties of different types of materials with the 1TM in a wide range of thermal conductivities (alloys, semiconductors and insulators). This sensor method measurement brought an additional key factor, which was the improvement of the sensitivity to parameters and reduction of their correlation. This allowed the identification of several parameters simultaneously, such as the thermal conductivity and the thermal heat capacity of the studied medium.

The fourth chapter was devoted to seek for the non-Fourier transport in some materials. The first part is to study the superdiffusive regime out of plane in alloys and model materials. The second to show that the heterodyne TDTR method allows to carry out mapping measurements and thus to study in-plane thermal properties.

First, we presented the characteristic of the intermediate superdiffusive regime, which appeared between the ballistic and diffusive regimes in some materials, notably alloys. Then, we introduced a model based on Lévy dynamics that allowed to describe the quasi-ballistic transport in a semi-infinite sample. The broadband spectral response and its modeling by a Lévy model allowed to identify the thermal properties of the studied samples, and to highlight the presence of non-diffusive transport in InGaAs alloy. Then, we investigated a model material of Mn-doped crystalline germanium matrix GeMn. The study was performed on different thicknesses of GeMn layer with different manganese concentration. Results of the thermal identification verified the absence of the superdiffusive regime in these material models; however, the thermal conductivity was affected by the concentration of nano-inclusions. New material samples based on Germanium and Silicon, which expected to exhibit a superdiffusive regime, are being manufactured.

In the second part of this chapter, we introduced a TDTR imaging technique to study the heat transport in plane. This technique provided the thermal measuring of heat carriers with high spatio-temporal resolution. In order to obtain the in-plane thermal properties, we introduced a model called the parabolic method that describes the spatial distribution of the heat. Finally, we presented the preliminary results obtained for the surface thermal characterization of a gold layer. The next step after this thesis would be to study the propagation of the superdiffusive regime in the plane.

Finally, the synthesis of the elements brought in this thesis was as follow:

- Development of a thermal sensor combining the measurements of heterodyne TDTR and FDTR methods. The wide bandwidth measured by this sensor allowed us to measure the different thermal behaviors in nanomaterials;
- Development of a thermal model using Matlab to determine the thermal properties of multi-layered nanomaterials;
- Development of a Labview program for the in-plane thermal mapping measurements. The program enabled to automate the measurement as much as possible and to speed up and facilitate data acquisition.

List of achievements

Peer-reviewed articles

A. Zenji, J.-M. Rampnoux, S. Grauby, and S. Dilhaire, " Ultimate-resolution thermal spectroscopy in time domain thermoreflectance (TDTR) ", Journal of Applied Physics 128, (2020).

S. Grauby, B. Vidal Montes, A. Zenji, J.-M. Rampnoux, and S. Dilhaire "How to Measure Hot Electron and Phonon Temperatures with Time Domain Thermoreflectance Spectroscopy?", ACS Photonics, (2022)

R. Burcea, J. F. Barbot, P. Renault, D. Eyidi, T. Girardeau, M. Marteau, F. Giovannelli, A. Zenji, J. M. Rampnoux, S. Dilhaire, P. Eklund, and A. le Febvrier, "Influence of Generated Defects by Ar Implantation on the Thermoelectric Properties of ScN", ACS Applied Energy Materials, (2022).

Conferences

Eurotherm / 2022 : Ultra-Broad Band Spectroscopy of Heat Transport at Nanoscale in Non-Fourier Materials , Oral Communication

E.MRS / 2021 : Metal Transducer Effect on Time Resolution in Thermoreflectance Spectroscopy, Oral Communication

References

- [1] O. M. Corbino, “Thermal oscillations in lamps of thin fibers with alternating current flowing through them and the resulting effect on the rectifier as a result of the presence of even-numbered harmonics,” *Phys. Z.*, vol. 11, 1910.
- [2] O. M. Corbino, “Periodic resistance changes of fine metal threads which are brought together by alternating streams as well as deduction of their thermo characteristics at high temperatures,” *Phys. Z.*, vol. 12, 1911.
- [3] D. Cahill and R. Pohl, “Thermal-conductivity of amorphous solids above the plateau,” *Physical Review B*, vol. 35, no. 8. American physical soc, one physics ellipse, college PK, MD 20740-3844 USA, pp. 4067–4073, 1987. doi: 10.1103/PhysRevB.35.4067.
- [4] D. G. Cahill, “Thermal conductivity measurement from 30 to 750 K: the 3ω method,” *Rev. Sci. Instrum.*, vol. 61, no. 2, pp. 802–808, Feb. 1990, doi: 10.1063/1.1141498.
- [5] O. Bourgeois, T. Fournier, and J. Chaussy, “Measurement of the thermal conductance of silicon nanowires at low temperature,” *J. Appl. Phys.*, vol. 101, no. 1, p. 016104, Jan. 2007, doi: 10.1063/1.2400093.
- [6] H. Ftouni *et al.*, “Specific heat measurement of thin suspended SiN membrane from 8 K to 300 K using the 3ω -Völklein method,” *Rev. Sci. Instrum.*, vol. 84, no. 9, p. 094902, Sep. 2013, doi: 10.1063/1.4821501.
- [7] D. Singhal *et al.*, “Measurement of anisotropic thermal conductivity of a dense forest of nanowires using the 3ω method,” *Rev. Sci. Instrum.*, vol. 89, no. 8, p. 084902, Aug. 2018, doi: 10.1063/1.5025319.
- [8] D. Cahill, A. Bullen, and S.-M. Lee, “Interface thermal conductance and the thermal conductivity of multilayer thin films,” *High Temp.-High Press.*, vol. 32, no. 2, pp. 135–142, 2000, doi: 10.1068/htwi9.
- [9] S. Gomès, A. Assy, and P.-O. Chapuis, “Scanning thermal microscopy: A review: Scanning thermal microscopy,” *Phys. Status Solidi A*, vol. 212, no. 3, pp. 477–494, Mar. 2015, doi: 10.1002/pssa.201400360.
- [10] S. Grauby *et al.*, “Joule expansion imaging techniques on microelectronic devices,” *Microelectron. J.*, vol. 40, no. 9, pp. 1367–1372, Sep. 2009, doi: 10.1016/j.mejo.2008.04.016.
- [11] S. Grauby *et al.*, “Qualitative Temperature Variation Imaging by Thermoreflectance and SThM Techniques,” p. 7, 2005.
- [12] S. Grauby, A. Salhi, L.-D. Patino Lopez, W. Claeys, B. Charlot, and S. Dilhaire, “Comparison of thermoreflectance and scanning thermal microscopy for microelectronic device temperature variation imaging: Calibration and resolution issues,” *Microelectron. Reliab.*, vol. 48, no. 2, pp. 204–211, Feb. 2008, doi: 10.1016/j.microrel.2007.04.008.
- [13] G. Wielgoszewski and T. Gotszalk, “Scanning Thermal Microscopy (SThM),” in *Advances in Imaging and Electron Physics*, vol. 190, Elsevier, 2015, pp. 177–221. doi: 10.1016/bs.aiep.2015.03.011.
- [14] S. Lefèvre, S. Volz, and P.-O. Chapuis, “Nanoscale heat transfer at contact between a hot tip and a substrate,” *Int. J. Heat Mass Transf.*, vol. 49, no. 1–2, pp. 251–258, Jan. 2006, doi: 10.1016/j.ijheatmasstransfer.2005.07.010.

- [15] E. Puyoo, S. Grauby, J.-M. Rampnoux, E. Rouvière, and S. Dilhaire, “Scanning thermal microscopy of individual silicon nanowires,” *J. Appl. Phys.*, vol. 109, no. 2, p. 024302, Jan. 2011, doi: 10.1063/1.3524223.
- [16] S. Lefèvre, J.-B. Saulnier, C. Fuentes, and S. Volz, “Probe calibration of the scanning thermal microscope in the AC mode,” *Superlattices Microstruct.*, vol. 35, no. 3–6, pp. 283–288, Mar. 2004, doi: 10.1016/j.spmi.2003.11.004.
- [17] W. J. Parker, R. J. Jenkins, C. P. Butler, and G. L. Abbott, “Flash Method of Determining Thermal Diffusivity, Heat Capacity, and Thermal Conductivity,” *J. Appl. Phys.*, vol. 32, no. 9, pp. 1679–1684, Sep. 1961, doi: 10.1063/1.1728417.
- [18] P. G. Bison, S. Marinetti, A. Mazzoldi, E. Grinzato, and C. Bressan, “Cross-comparison of thermal diffusivity measurements by thermal methods,” *Infrared Phys. Technol.*, vol. 43, no. 3–5, pp. 127–132, Jun. 2002, doi: 10.1016/S1350-4495(02)00130-5.
- [19] P. K. Bachmann *et al.*, “Thermal properties of C/H-, C/H/O-, C/H/N- and C/H/X-grown polycrystalline CVD diamond,” *Diam. Relat. Mater.*, vol. 4, no. 5–6, pp. 820–826, May 1995, doi: 10.1016/0925-9635(94)05229-8.
- [20] X. Liu, X. Wu, and T. Ren, “*In situ* and noncontact measurement of silicon membrane thermal conductivity,” *Appl. Phys. Lett.*, vol. 98, no. 17, p. 174104, Apr. 2011, doi: 10.1063/1.3583603.
- [21] S. Périchon, V. Lysenko, B. Remaki, D. Barbier, and B. Champagnon, “Measurement of porous silicon thermal conductivity by micro-Raman scattering,” *J. Appl. Phys.*, vol. 86, no. 8, pp. 4700–4702, Oct. 1999, doi: 10.1063/1.371424.
- [22] H. Malekpour and A. A. Balandin, “Raman-based technique for measuring thermal conductivity of graphene and related materials: Thermal conductivity of graphene and related materials,” *J. Raman Spectrosc.*, vol. 49, no. 1, pp. 106–120, Jan. 2018, doi: 10.1002/jrs.5230.
- [23] S. Sandell, E. Chávez-Ángel, A. El Sachat, J. He, C. M. Sotomayor Torres, and J. Maire, “Thermoreflectance techniques and Raman thermometry for thermal property characterization of nanostructures,” *J. Appl. Phys.*, vol. 128, no. 13, p. 131101, Oct. 2020, doi: 10.1063/5.0020239.
- [24] M. Lax, “Temperature rise induced by a laser beam,” *J Appl Phys*, vol. 48, p. 7, 1977.
- [25] I. H. Campbell and P. M. Fauchet, “The effects of microcrystal size and shape on the one phonon Raman spectra of crystalline semiconductors,” *Solid State Commun.*, vol. 58, no. 10, pp. 739–741, Jun. 1986, doi: 10.1016/0038-1098(86)90513-2.
- [26] P. Mishra and K. P. Jain, “Temperature-dependent Raman scattering studies in nanocrystalline silicon and finite-size effects,” *Phys. Rev. B*, vol. 62, no. 22, pp. 14790–14795, Dec. 2000, doi: 10.1103/PhysRevB.62.14790.
- [27] J. Opsal, A. Rosencwaig, and D. L. Willenborg, “Thermal-wave detection and thin-film thickness measurements with laser beam deflection,” *Appl. Opt.*, vol. 22, no. 20, p. 3169, Oct. 1983, doi: 10.1364/AO.22.003169.
- [28] S. L. Shapiro, Ed., *Ultrashort Light Pulses*, vol. 18. Berlin, Heidelberg: Springer Berlin Heidelberg, 1977. doi: 10.1007/978-3-662-22574-5.
- [29] A. Rosencwaig, J. Opsal, and D. L. Willenborg, “Thin-film thickness measurements with thermal waves,” p. 4, 1983.
- [30] J.-L. Battaglia, A. Kusiak, C. Rossignol, and N. Chigarev, “Thermal diffusivity of a metallic thin layer using the time-domain thermo reflectance technique,” *J. Phys. Conf. Ser.*, vol. 92, p. 012083, Dec. 2007, doi: 10.1088/1742-6596/92/1/012083.

- [31] V. Juvé *et al.*, “Cooling dynamics and thermal interface resistance of glass-embedded metal nanoparticles,” *Phys. Rev. B*, vol. 80, no. 19, p. 195406, Nov. 2009, doi: 10.1103/PhysRevB.80.195406.
- [32] C.-K. Sun, F. Vallée, L. Acioli, E. P. Ippen, and J. G. Fujimoto, “Femtosecond investigation of electron thermalization in gold,” *Phys. Rev. B*, vol. 48, no. 16, pp. 12365–12368, Oct. 1993, doi: 10.1103/PhysRevB.48.12365.
- [33] F. Decremps, L. Belliard, B. Perrin, and M. Gauthier, “Sound Velocity and Absorption Measurements under High Pressure Using Picosecond Ultrasonics in a Diamond Anvil Cell: Application to the Stability Study of AlPdMn,” *Phys. Rev. Lett.*, vol. 100, no. 3, p. 035502, Jan. 2008, doi: 10.1103/PhysRevLett.100.035502.
- [34] P. M. Norris, A. P. Caffrey, R. J. Stevens, J. M. Klopff, J. T. McLeskey, and A. N. Smith, “Femtosecond pump–probe nondestructive examination of materials (invited),” *Rev. Sci. Instrum.*, vol. 74, no. 1, pp. 400–406, Jan. 2003, doi: 10.1063/1.1517187.
- [35] D. M. Profunser, J. Vollmann, and J. Dual, “Determination of the material properties of microstructures by laser based ultrasound,” *Ultrasonics*, vol. 42, no. 1–9, pp. 641–646, Apr. 2004, doi: 10.1016/j.ultras.2004.01.049.
- [36] A. Crut, P. Maioli, N. Del Fatti, and F. Vallée, “Acoustic vibrations of metal nano-objects: Time-domain investigations,” *Phys. Rep.*, vol. 549, pp. 1–43, Jan. 2015, doi: 10.1016/j.physrep.2014.09.004.
- [37] S. Dilhaire and T. Phan, “Sondes laser et méthodes pour l’analyse thermique à l’échelle micrométrique. Application à la microélectronique,” p. 11.
- [38] T. Favaloro, J.-H. Bahk, and A. Shakouri, “Characterization of the temperature dependence of the thermoreflectance coefficient for conductive thin films,” *Rev. Sci. Instrum.*, vol. 86, no. 2, p. 024903, Feb. 2015, doi: 10.1063/1.4907354.
- [39] C. Paddock and G. Eesley, “Transient thermoreflectance from thin metal-films,” *Journal of applied physics*, vol. 60, no. 1. Amer inst physics, Circulation fulfillment div, 500 Sunnyside blvd, Woodbury, NY 11797-2999, pp. 285–290, Jul. 01, 1986. doi: 10.1063/1.337642.
- [40] G. Pernot, “Identification de propriétés thermiques et spectroscopie térahertz de nanostructures par thermoréfectance pompe-sonde asynchrone : application à l’étude du transport des phonons dans les super réseaux,” University of Bordeaux, 2010.
- [41] S. Dilhaire, G. Pernot, G. Calbris, J. M. Rampnoux, and S. Grauby, “Heterodyne picosecond thermoreflectance applied to nanoscale thermal metrology,” *Journal of applied physics*, vol. 110, no. 11. Amer inst physics, 1305 Walt whitman RD, STE 300, Melville, NY 11747-4501 USA, Dec. 01, 2011. doi: 10.1063/1.3665129.
- [42] A. Bartels, F. Hudert, C. Janke, T. Dekorsy, and K. Köhler, “Femtosecond time-resolved optical pump-probe spectroscopy at kilohertz-scan-rates over nanosecond-time-delays without mechanical delay line,” *Appl. Phys. Lett.*, vol. 88, no. 4, p. 041117, Jan. 2006, doi: 10.1063/1.2167812.
- [43] A. Casanova, Q. D’Acremont, G. Santarelli, S. Dilhaire, and A. Courjaud, “Ultrafast amplifier additive timing jitter characterization and control,” *Opt. Lett.*, vol. 41, no. 5, p. 898, Mar. 2016, doi: 10.1364/OL.41.000898.
- [44] Q. D’Acremont, “Étude des propriétés thermiques de bibliothèques d’alliages ternaires en couches minces et mise en évidence du transport non-diffusif par spectroscopie thermique pompe-sonde femtoseconde,” p. 88.

- [45] A. J. Schmidt, R. Cheaito, and M. Chiesa, “Characterization of thin metal films via frequency-domain thermoreflectance,” *J. Appl. Phys.*, vol. 107, no. 2, p. 024908, Jan. 2010, doi: 10.1063/1.3289907.
- [46] L. Wang, R. Cheaito, J. L. Braun, A. Giri, and P. E. Hopkins, “Thermal conductivity measurements of non-metals via combined time- and frequency-domain thermoreflectance without a metal film transducer,” *Rev. Sci. Instrum.*, vol. 87, no. 9, p. 094902, Sep. 2016, doi: 10.1063/1.4962711.
- [47] J. Hohlfeld, S.-S. Wellershoff, J. Gdde, U. Conrad, V. Jhnke, and E. Matthias, “Electron and lattice dynamics following optical excitation of metals,” *Chem. Phys.*, vol. 251, no. 1–3, pp. 237–258, Jan. 2000, doi: 10.1016/S0301-0104(99)00330-4.
- [48] S. I. Anisimov, “Electron emission from metal surfaces exposed to ultrashort laser pulses,” p. 3.
- [49] J. FOURIER, *Theorie analytique de la chaleur*. 1822.
- [50] H. C. Carslaw and J. C. Jaeger, *Conduction of Heat in Solids*. Oxford University Press, 1959.
- [51] D. Maillt, S. Andr, J. C. Batsale, A. Degiovanni, and C. Moyne, *Thermal Quadrupoles: Solving the Heat Equation through Integral Transforms*. 2000.
- [52] H. Garnier and L. Wang, Eds., *Identification of Continuous-time Models from Sampled Data*. London: Springer London, 2008. doi: 10.1007/978-1-84800-161-9.
- [53] A. Aouali, “Tomographie thermo-spectroscopique par imagerie 3D pour l’tude des torches `a plasma,” University of Bordeaux, 2022.
- [54] A. Tarantola, *Inverse Problem Theory and Methods for Model Parameter Estimation*. 2005.
- [55] J. Hadamard, *Lectures on Cauchy’s Problem in Linear Partial Differential Equations*. Yale University Press, 1923.
- [56] K. Madsen, H. B. Nielsen, and O. Tingleff, *Methods for non-linear least squares problems*. Technical University of Denmark, 2004.
- [57] “Matlab Optimization Toolbox Guide.” 2008.
- [58] D. G. Cahill and T. H. Allen, “Thermal conductivity of sputtered and evaporated SiO₂ and TiO₂ optical coatings,” *Appl. Phys. Lett.*, vol. 65, no. 3, pp. 309–311, Jul. 1994, doi: 10.1063/1.112355.
- [59] T. Yamane, N. Nagai, S. Katayama, and M. Todoki, “Measurement of thermal conductivity of silicon dioxide thin films using a 3ω method,” *J. Appl. Phys.*, vol. 91, no. 12, p. 9772, 2002, doi: 10.1063/1.1481958.
- [60] J. Alvarez-Quintana, J. Rodrguez-Viejo, F. X. Alvarez, and D. Jou, “Thermal conductivity of thin single-crystalline germanium-on-insulator structures,” *Int. J. Heat Mass Transf.*, vol. 54, no. 9–10, pp. 1959–1962, Apr. 2011, doi: 10.1016/j.ijheatmasstransfer.2011.01.006.
- [61] G. Pernot *et al.*, “Precise control of thermal conductivity at the nanoscale through individual phonon-scattering barriers,” *NATURE materials*, vol. 9, no. 6. Nature publishing group, Macmillan building, 4 Crinan ST, London N1 9XW, England, pp. 491–495, Jun. 2010. doi: 10.1038/NMAT2752.
- [62] J. Hohlfeld, S. Wellershoff, J. Gudde, U. Conrad, V. Jahnke, and E. Matthias, “Electron and lattice dynamics following optical excitation of metals,” *Chemical Physics*, vol. 251, no. 1–3. ELSEVIER science BV, PO BOX 211, 1000 AE Amsterdam, Netherlands, pp. 237–258, Jan. 01, 2000. doi: 10.1016/S0301-0104(99)00330-4.

- [63] R. B. Wilson, J. P. Feser, G. T. Hohensee, and D. G. Cahill, “Two-channel model for nonequilibrium thermal transport in pump-probe experiments,” *Phys. Rev. B*, vol. 88, no. 14, p. 144305, Oct. 2013, doi: 10.1103/PhysRevB.88.144305.
- [64] A. Majumdar and P. Reddy, “Role of electron–phonon coupling in thermal conductance of metal–nonmetal interfaces,” *Appl. Phys. Lett.*, vol. 84, no. 23, pp. 4768–4770, Jun. 2004, doi: 10.1063/1.1758301.
- [65] J. Hostetler, A. Smith, D. Czajkowsky, and P. Norris, “Measurement of the electron-phonon coupling factor dependence on film thickness and grain size in Au, Cr, and Al,” *Applied optics*, vol. 38, no. 16. Optical soc amer, 2010 Massachusetts AVE NW, Washington, DC 20036 USA, pp. 3614–3620, Jun. 01, 1999. doi: 10.1364/AO.38.003614.
- [66] P. E. Hopkins and P. M. Norris, “Substrate influence in electron–phonon coupling measurements in thin Au films,” *Appl. Surf. Sci.*, vol. 253, no. 15, pp. 6289–6294, May 2007, doi: 10.1016/j.apsusc.2007.01.065.
- [67] Y. Wang, J. Y. Park, Y. K. Koh, and D. G. Cahill, “Thermoreflectance of metal transducers for time-domain thermoreflectance,” *J. Appl. Phys.*, vol. 108, no. 4, p. 043507, Aug. 2010, doi: 10.1063/1.3457151.
- [68] P. L. Komarov, M. G. Burzo, and P. E. Raad, “A thermoreflectance thermography system for measuring the transient surface temperature field of activated electronic devices,” in *Twenty-Second Annual IEEE Semiconductor Thermal Measurement And Management Symposium*, Dallas, TX USA, 2006, pp. 199–203. doi: 10.1109/STHERM.2006.1625228.
- [69] A. M. Chen, Y. F. Jiang, L. Z. Sui, H. Liu, M. X. Jin, and D. J. Ding, “Thermal analysis of double-layer metal films during femtosecond laser heating,” *J. Opt.*, vol. 13, no. 5, p. 055503, May 2011, doi: 10.1088/2040-8978/13/5/055503.
- [70] A. Caffrey, P. Hopkins, J. Klopff, and P. Norris, “Thin film non-noble transition metal thermophysical properties,” *Microscale thermophysical engineering*, vol. 9, no. 4. Taylor & Francis inc, 530 Walnut street, STE 850, Philadelphia, PA 19106 USA, pp. 365–377, Dec. 2005. doi: 10.1080/10893950500357970.
- [71] Z. Lin, L. V. Zhigilei, and V. Celli, “Electron-phonon coupling and electron heat capacity of metals under conditions of strong electron-phonon nonequilibrium,” *Physical Review B*, vol. 77, no. 7. Amer physical soc, One physics ellipse, College PK, MD 20740-3844 USA, Feb. 2008. doi: 10.1103/PhysRevB.77.075133.
- [72] D. G. Cahill, “Analysis of heat flow in layered structures for time-domain thermoreflectance,” *Rev. Sci. Instrum.*, vol. 75, no. 12, pp. 5119–5122, Dec. 2004, doi: 10.1063/1.1819431.
- [73] A. J. Schmidt, R. Cheaito, and M. Chiesa, “A frequency-domain thermoreflectance method for the characterization of thermal properties,” *Rev. Sci. Instrum.*, vol. 80, no. 9, p. 094901, Sep. 2009, doi: 10.1063/1.3212673.
- [74] W.-L. Ong, S. M. Rupich, D. V. Talapin, A. J. H. McGaughey, and J. A. Malen, “Surface chemistry mediates thermal transport in three-dimensional nanocrystal arrays,” *Nat. Mater.*, vol. 12, no. 5, pp. 410–415, May 2013, doi: 10.1038/nmat3596.
- [75] H. R. Shanks, P. D. Maycock, P. H. Sidles, and G. C. Danielson, “Thermal Conductivity of Silicon from 300 to 1400°K,” *Phys. Rev.*, vol. 130, no. 5, pp. 1743–1748, Jun. 1963, doi: 10.1103/PhysRev.130.1743.
- [76] C. J. Glassbrenner and G. A. Slack, “Thermal Conductivity of Silicon and Germanium from 3°K to the Melting Point,” *Phys. Rev.*, vol. 134, no. 4A, pp. A1058–A1069, May 1964, doi: 10.1103/PhysRev.134.A1058.

- [77] P. V. Burmistrova *et al.*, “Thermoelectric properties of epitaxial ScN films deposited by reactive magnetron sputtering onto MgO(001) substrates,” *J. Appl. Phys.*, vol. 113, no. 15, p. 153704, Apr. 2013, doi: 10.1063/1.4801886.
- [78] N. Tureson *et al.*, “Reduction of the thermal conductivity of the thermoelectric material ScN by Nb alloying,” *J. Appl. Phys.*, vol. 122, no. 2, p. 025116, Jul. 2017, doi: 10.1063/1.4993913.
- [79] R. Burcea, J.-M. Rampnoux, S. Dilhaire, and P. Eklund, “Influence of implantation induced defects on the thermoelectric properties of ScN,” p. 20.
- [80] D.-W. Oh, C. Ko, S. Ramanathan, and D. G. Cahill, “Thermal conductivity and dynamic heat capacity across the metal-insulator transition in thin film VO₂,” *Appl Phys Lett*, p. 4, 2014.
- [81] I. Stark, M. Stordeur, and F. Syrowatka, “Thermal conductivity of thin amorphous alumina films,” *Thin Solid Films*, vol. 226, no. 1, pp. 185–190, Apr. 1993, doi: 10.1016/0040-6090(93)90227-G.
- [82] Y. A. Volkov, S. Palatnik, and A. T. Pugachev, “Investigation of the thermal properties of thin aluminum films,” vol. 43, p. 4, 1976.
- [83] T. L. Bergman, A. S. Lavine, F. P. Incropera, and D. P. Dewitt, *Fundamentals of Heat and Mass Transfer*. 2011.
- [84] Y. K. Koh and D. G. Cahill, “Frequency dependence of the thermal conductivity of semiconductor alloys,” *Phys. Rev. B*, vol. 76, no. 7, p. 075207, Aug. 2007, doi: 10.1103/PhysRevB.76.075207.
- [85] C. Bera, N. Mingo, and S. Volz, “Marked Effects of Alloying on the Thermal Conductivity of Nanoporous Materials,” *Phys. Rev. Lett.*, vol. 104, no. 11, p. 115502, Mar. 2010, doi: 10.1103/PhysRevLett.104.115502.
- [86] A. J. Minnich *et al.*, “Thermal Conductivity Spectroscopy Technique to Measure Phonon Mean Free Paths,” *Phys. Rev. Lett.*, vol. 107, no. 9, p. 095901, Aug. 2011, doi: 10.1103/PhysRevLett.107.095901.
- [87] K. T. Regner, D. P. Sellan, Z. Su, C. H. Amon, A. J. H. McGaughey, and J. A. Malen, “Broadband phonon mean free path contributions to thermal conductivity measured using frequency domain thermoreflectance,” *Nat. Commun.*, vol. 4, no. 1, p. 1640, Jun. 2013, doi: 10.1038/ncomms2630.
- [88] M. E. Siemens *et al.*, “Quasi-ballistic thermal transport from nanoscale interfaces observed using ultrafast coherent soft X-ray beams,” *Nat. Mater.*, vol. 9, no. 1, pp. 26–30, Jan. 2010, doi: 10.1038/nmat2568.
- [89] L. Zeng *et al.*, “Measuring Phonon Mean Free Path Distributions by Probing Quasiballistic Phonon Transport in Grating Nanostructures,” *Sci. Rep.*, vol. 5, no. 1, p. 17131, Dec. 2015, doi: 10.1038/srep17131.
- [90] O. W. Kiiding, H. Shurk, A. A. Maznev, and E. Matthias, “Transient thermal gratings at surfaces for thermal characterization of bulk materials and thin films,” p. 9.
- [91] J. A. Johnson *et al.*, “Direct Measurement of Room-Temperature Nondiffusive Thermal Transport Over Micron Distances in a Silicon Membrane,” *Phys. Rev. Lett.*, vol. 110, no. 2, p. 025901, Jan. 2013, doi: 10.1103/PhysRevLett.110.025901.
- [92] B. Vermeersch, J. Carrete, N. Mingo, and A. Shakouri, “Superdiffusive heat conduction in semiconductor alloys. I. Theoretical foundations,” *Phys. Rev. B*, vol. 91, no. 8, p. 085202, Feb. 2015, doi: 10.1103/PhysRevB.91.085202.

- [93] M. F. Shlesinger, J. Klafter, and G. Zumofen, “Above, below and beyond Brownian motion,” *Am. J. Phys.*, vol. 67, no. 12, pp. 1253–1259, Dec. 1999, doi: 10.1119/1.19112.
- [94] B. Vermeersch, G. Pernot, Y.-R. Koh, P. Abumov, and A. Shakouri, “Ballistic heat transport and associated frequency dependence of thermal conductivity in semiconductor alloys,” in *13th InterSociety Conference on Thermal and Thermomechanical Phenomena in Electronic Systems*, San Diego, CA, USA, May 2012, pp. 428–434. doi: 10.1109/ITHERM.2012.6231462.
- [95] B. Vermeersch and N. Mingo, “Quasiballistic heat removal from small sources studied from first principles,” *Phys. Rev. B*, vol. 97, no. 4, p. 045205, Jan. 2018, doi: 10.1103/PhysRevB.97.045205.
- [96] B. Vermeersch, “Compact stochastic models for multidimensional quasiballistic thermal transport,” *J. Appl. Phys.*, vol. 120, no. 17, p. 175102, Nov. 2016, doi: 10.1063/1.4965866.
- [97] J. Klafter and I. M. Sokolov, “Anomalous diffusion spreads its wings,” *Phys. World*, vol. 18, no. 8, pp. 29–32, Aug. 2005, doi: 10.1088/2058-7058/18/8/33.
- [98] P. Barthelemy, J. Bertolotti, and D. S. Wiersma, “A Lévy flight for light,” *Nature*, vol. 453, no. 7194, pp. 495–498, May 2008, doi: 10.1038/nature06948.
- [99] A. M. S. Mohammed *et al.*, “Fractal Lévy Heat Transport in Nanoparticle Embedded Semiconductor Alloys,” *Nano Lett.*, vol. 15, no. 7, pp. 4269–4273, Jul. 2015, doi: 10.1021/nl5044665.
- [100] K. Esfarjani, G. Chen, and H. T. Stokes, “Heat transport in silicon from first-principles calculations,” *Phys. Rev. B*, vol. 84, no. 8, p. 085204, Aug. 2011, doi: 10.1103/PhysRevB.84.085204.
- [101] A. Ward and D. A. Broido, “Intrinsic phonon relaxation times from first-principles studies of the thermal conductivities of Si and Ge,” *Phys. Rev. B*, vol. 81, no. 8, p. 085205, Feb. 2010, doi: 10.1103/PhysRevB.81.085205.
- [102] B. Vermeersch, A. M. S. Mohammed, G. Pernot, Y. R. Koh, and A. Shakouri, “Superdiffusive heat conduction in semiconductor alloys. II. Truncated Lévy formalism for experimental analysis,” *Phys. Rev. B*, vol. 91, no. 8, p. 085203, Feb. 2015, doi: 10.1103/PhysRevB.91.085203.
- [103] J. Klafter, A. Blumen, and M. F. Shlesinger, “Stochastic pathway to anomalous diffusion,” *Phys. Rev. A*, vol. 35, no. 7, pp. 3081–3085, Apr. 1987, doi: 10.1103/PhysRevA.35.3081.
- [104] P. D. Maycock, “Thermal conductivity of silicon, germanium, iii-v compounds and iii-v alloys,” p. 8.
- [105] O. Bourgeois *et al.*, “Reduction of phonon mean free path: From low-temperature physics to room temperature applications in thermoelectricity,” *Comptes Rendus Phys.*, vol. 17, no. 10, pp. 1154–1160, Dec. 2016, doi: 10.1016/j.crhy.2016.08.008.
- [106] D. Tainoff *et al.*, “Thermoelectric properties of high quality nanostructured Ge:Mn thin films,” p. 13.
- [107] Y. Q. Liu *et al.*, “Sensitive 3-omega measurements on epitaxial thermoelectric thin films,” *IOP Conf. Ser. Mater. Sci. Eng.*, vol. 68, p. 012005, Nov. 2014, doi: 10.1088/1757-899X/68/1/012005.
- [108] T. Devillers, “Etude des propriétés physiques des phases de Ge(1-x)Mn(x) ferromagnétiques pour l’électronique de spin,” p. 175.
- [109] J. Paterson, “Experimental investigation of heat transport in nanomaterials using electro-thermal methods.”

- [110] F. Cernuschi, A. Russo, L. Lorenzoni, and A. Figari, “In-plane thermal diffusivity evaluation by infrared thermography,” *Rev. Sci. Instrum.*, vol. 72, no. 10, pp. 3988–3995, Oct. 2001, doi: 10.1063/1.1400151.
- [111] L. Gaverina *et al.*, “Constant Velocity Flying Spot for the estimation of in-plane thermal diffusivity on anisotropic materials,” *Int. J. Therm. Sci.*, vol. 145, p. 106000, Nov. 2019, doi: 10.1016/j.ijthermalsci.2019.106000.
- [112] B. Huttner, “Femtosecond Laser Pulse Interactions with Metals,” p. 23.